



UNIVERSITÀ  
DEGLI STUDI  
FIRENZE

DOTTORATO DI RICERCA IN  
ATOMIC AND MOLECULAR PHOTONICS

CICLO XXXIII

COORDINATORE Prof. FRANCESCO CATALIOTTI

ENHANCING THE PERFORMANCE OF POTENTIAL  
MOLECULAR QUBITS: INSIGHT INTO THE PHONONS  
INVOLVED IN THE SPIN-LATTICE RELAXATION

Settore Scientifico Disciplinare CHIM/02

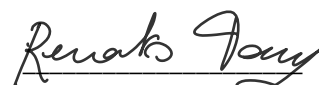
**Dottorando**

Dott. Stefano Benci

  
(firma)


**Tutore**

Prof. Renato Torre

  
(firma)


**Co-tutore**

Prof.ssa Roberta Sessoli

  
(firma)

**Coordinatore**

Prof. Francesco Cataliotti

  
(firma)

Anni 2017/2020



# Contents

<b>Preface</b>	<b>vii</b>
<b>I Introduction</b>	<b>1</b>
<b>1 What is a Quantum Bit?</b>	<b>3</b>
1.1 Molecular electronic spin Qubits . . . . .	7
<b>II Theoretical background</b>	<b>11</b>
<b>2 Spin-orbit coupling</b>	<b>13</b>
<b>3 Spin Hamiltonian</b>	<b>17</b>
<b>4 Theory of spin relaxation</b>	<b>21</b>
4.1 The spin-lattice relaxation . . . . .	22
4.1.1 The Harmonic lattice . . . . .	23
4.1.2 The one-phonon process: Direct mechanism . . . . .	24
4.1.3 The two-phonons process: Raman mechanism . . . . .	27
4.1.4 Resonant Raman process: Orbach mechanism . . . . .	28
4.1.5 The spin-phonon Bottleneck effect . . . . .	29
4.2 The spin-spin relaxation . . . . .	31
<b>5 Spin-phonon dynamics theory</b>	<b>33</b>
5.1 Some useful numbers . . . . .	37
<b>III Experimental section</b>	<b>39</b>
<b>6 Time Domain THz Spectroscopy</b>	<b>43</b>
6.1 Set-up based on photoconductive antennas . . . . .	43
6.2 Set-up based on plasma and ABC detection . . . . .	45

## CONTENTS

6.3	Extraction of optical parameters from the measurements . . . . .	47
6.4	The THz spectrum . . . . .	51
6.5	Investigation of water absorption coefficient in FIR . . . . .	53
<b>7</b>	<b>Time-resolved THz-EPR spectroscopy</b>	<b>55</b>
7.1	NovoFEL . . . . .	55
7.2	EPR spectrometer . . . . .	58
7.3	THz waveguide and optical setup . . . . .	59
<b>8</b>	<b>Sample preparation</b>	<b>61</b>
8.1	THz-TDS measurements . . . . .	61
8.2	TR-THz-EPR measurements . . . . .	61
<b>IV</b>	<b>Results and discussion</b>	<b>65</b>
<b>9</b>	<b>THz spectroscopy as innovative probe of the molecular Qubits performance</b>	<b>69</b>
9.1	The Vanadyl prototype: VO(acac) <sub>2</sub> . . . . .	70
9.1.1	Molecular and crystal structure . . . . .	70
9.1.2	Magnetic properties . . . . .	70
9.1.3	Investigation of low energy vibrations . . . . .	72
9.1.4	Simulation results . . . . .	77
9.1.5	Conclusion . . . . .	78
9.2	The role of the rigidity of the coordination shell . . . . .	79
9.2.1	Molecular and crystal structures . . . . .	80
9.2.2	Magnetic properties . . . . .	82
9.2.3	Spectroscopic investigation . . . . .	85
9.2.4	Conclusions . . . . .	88
9.3	Investigation of the spin-phonon coupling by first-principles approach	89
9.3.1	Molecular and crystal structure . . . . .	89
9.3.2	Spectroscopic investigation . . . . .	91
9.3.3	Spin-phonon coupling analysis . . . . .	94
9.3.4	Conclusions . . . . .	96
9.4	Arranging the Qubit units into a Metal Organic Framework . . . . .	98
9.4.1	Molecular and crystal structure . . . . .	98
9.4.2	Magnetic properties . . . . .	100
9.4.3	Spectroscopic investigation . . . . .	103
9.4.4	Conclusions . . . . .	105
9.5	Summary . . . . .	107

<b>10 Spin dynamics under THz irradiation</b>	<b>109</b>
10.1 Pulse EPR investigation	110
10.1.1 $T_1$ measurements at 7 and 70 K in a wide magnetic field range	110
10.1.2 Temperature dependence of $T_1$	116
10.1.3 $T_2$ measurements at 7 and 70 K	117
10.2 CW-EPR measurements	120
10.2.1 Saturation curves of VOTPP 2%	120
10.2.2 Estimation of the sample T-jump	123
10.3 2D-THz-EPR experiments	125
10.4 MW power dependence of TR-THz-EPR signal	131
10.5 Temperature dependence of TR-THz-EPR signal	134
10.6 THz radiation frequency dependence of the TR-THz-EPR signal	140
10.7 THz power dependence of the TR-THz-EPR signal	143
10.8 Simulations	145
10.8.1 Description of the model	146
10.8.2 Simulation of MW power dependence at 20 K	148
10.8.3 Simulation of MW power dependence at 55 K	153
10.8.4 Simulation of THz power dependence	156
10.9 Conclusions	158
<b>V Conclusions</b>	<b>163</b>
<b>Appendices</b>	<b>167</b>
<b>A Error analysis</b>	<b>169</b>
<b>B Origin of Bloch equations</b>	<b>173</b>
B.1 Bloch equations with relaxation process	174
B.2 Including perturbation in the system: RF field	175
B.3 Rotating frame	175

*CONTENTS*

# Preface

The aim of this PhD work is the optimization of the molecular Qubits performances through the research of the key “elements” to enhance the spin-lattice relaxation time,  $T_1$ . The study has been focused on Vanadium(IV) coordination compounds whose magnetic properties are due to the single unpaired electron, resulting in a  $S = 1/2$  spin value. This element shows a weak spin-orbit coupling and, consequently, a small spin-phonon coupling, that makes it particularly suitable for the purpose. Two classes of complexes have been taken into account: vanadyl-based molecules, which show the  $VO^{2+}$  metal centre in a square pyramidal coordination geometry, and  $V^{4+}$ -based ones in which the metal centre is octahedrally coordinated. Several ligands have been used in order to test different structural effects on the spin relaxation. In this study we utilized different experimental techniques to investigate different aspects of the issue. We jointed standard magnetic techniques, as alternate-current (AC) susceptometry, continuous-wave (CW) and pulse electron paramagnetic resonance (EPR) spectroscopy, and TeraHertz time-domain spectroscopy (THz-TDS) for the characterization of the phonons of the complexes in the crystal phase.

Moreover, a deeper investigation of the spin-lattice relaxation mechanisms required a more exotic technique, that is time-resolved THz-pump EPR-probe (TR-THz-EPR) measurements, which exploits the free electron laser radiation as THz source at the Novosibirsk Free Electron Laser (NovoFEL) facility.

The whole work has been supported by theoretical calculations that has been fundamental in the rationalization of several experimental results.

The employment of such a large number of different techniques results in a wide interdisciplinary collaboration with many chemists and physicists, thanks to whom it has been possible reaching the results here described.

The following pages are organized in several parts and each of them includes different chapters. *Part I* provides a general introduction about Qubits and, in particular, those based on molecular electronic spins. In *part II*, many theoretical concepts that I consider to be essential in the comprehension of this work are discussed, such as the theory of the spin relaxation and the spin-phonon interaction,

*CHAPTER 0. Preface*

with a short mention to the spin-orbit coupling. In *part III*, the techniques based on custom setups, as THz-TDS setups and the NovoFEL equipment, as well as the samples preparation, are examined. *Part IV*, which represents the heftiest one, is devoted to the results obtained during these years. It is divided in two chapters, according to the two main topics: the former contains the outcomes obtained by the combination of magnetic techniques and THz-TD spectroscopy, arranged according to the publications; while the latter includes the investigation of THz-induced effects on the spin dynamics, performed at NovoFEL. In *part V*, that is the last one, a summary of this work helps in picking up the pieces.



## Part I

# Introduction



# Chapter 1

## What is a Quantum Bit?

During the last century, the quantum physics drastically changed our lifestyle and our point of view on what the matter is. The *quantization of the energy* supposed by Max Plank, through the well-known law  $E = h\nu$  at the beginning of the twentieth century, represents the first breakthrough in the comprehension of the quantum nature of the matter. Few years later, Wernel Karl Heisenberg stated his *uncertainty principle*, which asserting the limit to the accuracy with which the values for certain pairs of physical quantities of a particle, such as position and momentum, can be predicted from initial conditions. These were the basis from which the modern physics started on. Erwin Schrödinger, in 1926, published the quantum mechanics counterpart of the Newton's Law, universally known as Schrödinger equation[1]. Through the latter it was possible to describe the microscopic universe of atoms and molecules in terms of wave functions, i.e. the most complete description that can be given of a physical system, according to the Copenhagen interpretation. Thanks to quantum mechanics, a huge number of inventions came up with, such as lasers, quantum cryptography and many other devices that are essential in our everyday life.

The birth of modern computer science dates back to 1936 with a breakthrough paper of Alan Turing[2]. In that work, Turing provided the first formalization of the concepts of algorithm and computation, nowadays known as *Turing machine*. Few years later, John von Neumann developed a simple theoretical model concerning how to put together all the components required for implementing the Turing machine in a practical fashion[3]. The hardware development became finally a reality in 1947, when John Bardeen, Walter Brattain, and William Shockley built up the first transistor, for which they were awarded the Nobel Prize. Since then, computer hardware has grown in power at an impressive rate. In spite of that, the progressive miniaturization of the computer hardware led to deal with the quantum effects, that become not negligible under a certain size.

## CHAPTER 1. What is a Quantum Bit?

This suddenly put a striking limitation in the computer progression.

A further breakthrough came from David Deutsch[4] and Richard Feynman[5], who suggested to exploit the quantum physics properties to perform calculations, instead of classical physics ones, leading to the foundation of *quantum computation*. Obviously, the exploitation of quantum phenomena requires a completely different hardware compared to that of standard computer, which have to be based on quantum objects.

Nowadays, all the computers are based on the *Binary Digit*, or *Bit*, which represents the basic unit in computing and digital communications. The Bit represents a logical state with one of two possible values 0 and 1, and can be stored in any physical system that exists in either of two possible distinct states. In practice, a Bit is usually represented by an electrical or current signal, or by the electrical state of a flip-flop circuit. The quantum equivalent of the Bit is the *Quantum Bit*, or *Qubit*. According to quantum mechanics, the general quantum state of a Qubit can be represented by a linear superposition of its two orthonormal basis states, usually denoted as  $|0\rangle$  and  $|1\rangle$ , where the symbol “ $| \ )$ ” is the standard notation for states in quantum mechanics by using the Dirac notation. These two orthonormal basis states,  $\{|0\rangle, |1\rangle\}$ , together called the *computational basis*, span the two-dimensional linear vector Hilbert space of the Qubit. In analogy with the Bit, the Qubit can be addressed in the excited state  $|1\rangle$ , in the fundamental state  $|0\rangle$ , but also in a coherent superposition of the basis states. This means that a single Qubit can be described by a linear combination of  $|1\rangle$  and  $|0\rangle$  according to equation 1.1

$$|\psi\rangle = \alpha |0\rangle + \beta |1\rangle \quad (1.1)$$

where  $\alpha$  and  $\beta$  are the probability amplitudes and can, in general, be complex numbers. When the qubit is “measured” in the standard basis, according to the Born rule, the probability of outcome 0 is  $|\alpha|^2$  and the probability of outcome 1 is  $|\beta|^2$ . Because the absolute squares of the amplitudes equate to probabilities, it follows that  $|\alpha|^2 + |\beta|^2 = 1$ . Note that a Qubit in this superposition state does not have a value in between 0 and 1; rather, when measured, it has a probability  $|\alpha|^2$  of the value 0 and a probability  $|\beta|^2$  of the value 1. In other words, superposition means that there is no way, even in principle, to know which of the two possible states is forming the superposition state actually pertains. A useful way to visualize a single Qubit is using the *Bloch sphere* (Figure 1.1).

In this picture, the state of the Qubit can be rewritten as in equation 1.2.

$$|\psi\rangle = \cos \frac{\theta}{2} |0\rangle + e^{i\phi} \sin \frac{\theta}{2} |1\rangle \quad (1.2)$$

Where  $\theta$  and  $\phi$  are real numbers and define a point on the surface of the

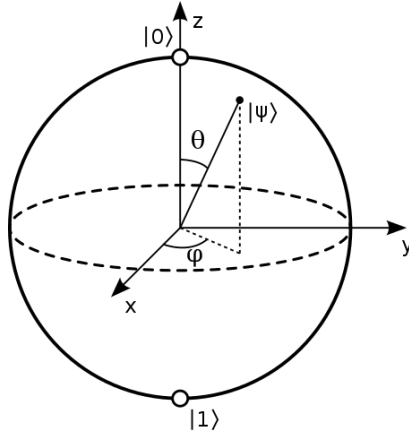


**Figure 1.1:** Bloch sphere representation of the Qubit.

sphere. Represented on such a sphere, a classical bit could only be at the “North Pole” or the “South Pole”, in the locations where  $|0\rangle$  and  $|1\rangle$  are respectively. A pure state is fully specified by a single ket  $|\psi\rangle$ , as  $|\psi\rangle = \alpha |0\rangle + \beta |1\rangle$ , a coherent superposition as described above. Coherence is essential for a Qubit to be in a superposition state. With interactions and *decoherence*, it is possible to put the Qubit in a mixed state, a statistical combination or incoherent mixture of different pure states. Mixed states can be represented by points inside the Bloch sphere and they have three degrees of freedom: the two angles  $\theta$  and  $\phi$ , as well as the length  $r$  of the vector that represents the mixed state.

The time-evolution of the state  $|\psi\rangle$  is described by a unitary transformation that can be always defined through the operator  $U(t)$ , for which

$$|\psi'\rangle = U(t) |\psi\rangle \quad (1.3)$$

Each unitary operator represents the operation performed by a so-called *quantum logic gate*, of which there are a rich variety. Some examples of quantum gates are the following:

- *Hadamard gate* ( $H$ ) is a one-Qubit rotation, mapping the Qubit-basis states  $|0\rangle$  and  $|1\rangle$  to two superposition states with equal weight

$$\begin{aligned} H |0\rangle &= \frac{|0\rangle + |1\rangle}{\sqrt{2}} \\ H |1\rangle &= \frac{|0\rangle - |1\rangle}{\sqrt{2}} \end{aligned} \quad (1.4)$$

- *NOT-gate* is a quantum gate which takes either  $|0\rangle$  to  $|1\rangle$  or  $|1\rangle$  to  $|0\rangle$ ;

- *CNOT-gate* is a two-Qubits gate with no classical analogue. It acts as a NOT-gate flipping the second Qubit (target Qubit) if and only if the first one (control Qubit) is in the state  $|1\rangle$ , and does nothing otherwise.

Before		After	
Control	Target	Control	Target
$ 0\rangle$	$ 0\rangle$	$ 0\rangle$	$ 0\rangle$
$ 0\rangle$	$ 1\rangle$	$ 0\rangle$	$ 1\rangle$
$ 1\rangle$	$ 0\rangle$	$ 1\rangle$	$ 1\rangle$
$ 1\rangle$	$ 1\rangle$	$ 1\rangle$	$ 0\rangle$

**Table 1.1:** CNOT-gate applied to a two-Qubits system.

An important distinguishing feature between Qubits and classical Bits is that multiple Qubits can exhibit *quantum entanglement*. Quantum entanglement is a nonlocal property of two or more Qubits whereby it is no longer possible to describe the state of the two or more Qubits independently. Such a property has no classical equivalent and it establishes the main difference between classical and quantum physics. The entanglement is a natural occurrence of quantum systems when they are correlated by some weak interaction, and it is a necessary property to realize two-Qubits gates.

Despite the potentiality of using Qubits, several problems must be solved before reaching the capability to fulfill a real quantum computer. The five criteria proposed by DiVincenzo[6] for realizing a quantum computer are listed below:

1. scalable physical systems having each Qubit sufficiently isolated in order to exhibit a proper two-level basis;
2. the ability to initialize the state of the Qubits;
3. long coherence times compared to the gate operation time;
4. a universal set of quantum gates;
5. the capability to readout the Qubit.

Many efforts have been done during last years to find proper physical systems working as Qubits. Some examples are: cold trapped ions[7], bulk nuclear magnetic resonance[8], cavity quantum electrodynamics[9], quantum dots[10][11], donor atoms[12][13], linear optics[14], colour centres in diamond[15][16], carbon nanotubes[17] and molecular spins[18][19][20][21][22][23].

The realization of quantum computers is a challenging task since it is basically a fragile equilibrium between the requirement of a well-isolated quantum

system to retain the quantum properties, but at the same time, the Qubits must be accessible for their manipulation. In this framework, the concept of *decoherence*, already mentioned by DiVincenzo[6], becomes a key parameter in the evaluation of the Qubit's performances. It depends on the quantum system chosen for the Qubit implementation as well as on the method (instrument) used for its manipulation. Two parameters are essential to set the time-scale of the longest quantum computation: the time during which the system maintains the coherence,  $\tau_m$ , and the time required for the basic computation action, i.e. the elementary unitary transformation,  $\tau_{op}$ .

## 1.1 Molecular electronic spin Qubits

Molecular electronic spins are particularly interesting from the point of view of this dissertation, since they represent the core of this work. Accordingly, for such a system the ratio  $\tau_m/\tau_{op}$  should be  $10^4$ [24], therefore the required coherence time is approximately tens of microseconds if a manipulation time equal to few tens of nanoseconds is considered, when pulse EPR is used.

Two simultaneously relaxation processes act on an ensemble of spin Qubits:

- *spin-lattice* or *longitudinal relaxation*, which describes the random transitions from the excited state  $|1\rangle$  to the ground state  $|0\rangle$ . The process is described by the spin-lattice relaxation time,  $T_1$ ;
- *spin-spin* or *transverse relaxation*, that describes the loses of coherence among the spins caused by their different surrounding. The spin-spin relaxation time,  $T_2$ , represents the time needed to pass from a pure quantum state to a mixed quantum state.

The two relaxation times are related to each other, and in particular  $T_1$  represents the upper limit of  $T_2$ [25].

Molecular Qubits result particularly appealing thanks to their versatility from the engineering point of view, since, for instance, they can be easily addressed on surfaces[26]. Furthermore, a fine tuning of the interaction between the paramagnetic centres is achievable through an *ad-hoc* synthetic strategy.

Several electronic spin systems are under development, such as Single Molecule Magnets (SMMs), lanthanide ions and light transition metals. Among them, SMMs have been the first proposed systems and it is worth mentioning  $\text{Fe}_8$ [27][28],  $\text{Cr}_7\text{Ni}$ [29] and  $\text{Fe}_4$ [30]. Lanthanide ions allow a great control over the energy level structure and electron-nuclear hyperfine interaction making them appeal for solid-state Qubits[31][32]. Recently, mononuclear light transition metal complexes, in which the metal bears a single unpaired electron, have been proposed

as spin Qubits and the first example was Cu(II)-phthalocyanine which showed coherence times around a few microseconds at 80 K[33]. They show a relatively long coherence time, especially at high temperature, due to the limited number of relaxation pathways. Indeed, the main source of decoherence is the interaction between the electronic spin with the nuclear one, because of the lack of the electronic spin-spin interaction, namely the *Zero-field splitting*, which is typical for  $S > 1/2$  spin systems. In particular, 3d-metals show long coherence time due to the weak spin-orbit coupling. This reflects in a weak spin-phonon coupling and a resulting longer  $T_1$ [26].

In this framework, the enhancement of the spin-lattice relaxation time as well as the comprehension of the spin-lattice interactions is crucial in the improvement of electronic molecular Qubits, with the aim to propose them as real devices. These purposes represent the core of this three-years work that has been focused on vanadyl molecules.

## References

- [1] Erwin Schrödinger. “An undulatory theory of the mechanics of atoms and molecules”. In: *Physical review* 28.6 (1926), p. 1049.
- [2] A.M. Turing. “On computable numbers, with an application to the Entscheidungs problem.” In: *Proceedings of the London Mathematical Society* 42.2 (1936), pp. 230–265.
- [3] John von Neumann. “First draft of a report on the EDVAC. contract no. w-670-ord-4926”. In: *The Origins of Digital Computers: Selected Papers, 3rd edn (Berlin/Heidelberg/New York: Springer-Verlag) (1945)*.
- [4] David Deutsch. “Quantum theory, the Church–Turing principle and the universal quantum computer”. In: *Proceedings of the Royal Society of London. A. Mathematical and Physical Sciences* 400.1818 (1985), pp. 97–117.
- [5] Richard P Feynman. “Quantum mechanical computers”. In: *Foundations of physics* 16.6 (1986), pp. 507–531.
- [6] David P DiVincenzo. “The physical implementation of quantum computation”. In: *Fortschritte der Physik: Progress of Physics* 48.9-11 (2000), pp. 771–783.
- [7] Juan I Cirac and Peter Zoller. “Quantum computations with cold trapped ions”. In: *Physical review letters* 74.20 (1995), p. 4091.
- [8] N Gershenfeld and I Chuang. “The usefulness of NMR quantum computing-response”. In: *Science* 277.5332 (1997), pp. 1689–1690.



## REFERENCES

- [9] Quentin A Turchette et al. “Measurement of conditional phase shifts for quantum logic”. In: *Physical Review Letters* 75.25 (1995), p. 4710.
- [10] A Imamog et al. “Quantum information processing using quantum dot spins and cavity QED”. In: *Physical review letters* 83.20 (1999), p. 4204.
- [11] Daniel Loss and David P DiVincenzo. “Quantum computation with quantum dots”. In: *Physical Review A* 57.1 (1998), p. 120.
- [12] Bruce E Kane. “A silicon-based nuclear spin quantum computer”. In: *nature* 393.6681 (1998), pp. 133–137.
- [13] Rutger Vrijen et al. “Electron-spin-resonance transistors for quantum computing in silicon-germanium heterostructures”. In: *Physical Review A* 62.1 (2000), p. 012306.
- [14] Emanuel Knill, Raymond Laflamme, and Gerald J Milburn. “A scheme for efficient quantum computation with linear optics”. In: *nature* 409.6816 (2001), pp. 46–52.
- [15] Ronald Hanson and David D Awschalom. “Coherent manipulation of single spins in semiconductors”. In: *Nature* 453.7198 (2008), pp. 1043–1049.
- [16] Patrick Maletinsky et al. “A robust scanning diamond sensor for nanoscale imaging with single nitrogen-vacancy centres”. In: *Nature nanotechnology* 7.5 (2012), pp. 320–324.
- [17] Denis V Bulaev, Björn Trauzettel, and Daniel Loss. “Spin-orbit interaction and anomalous spin relaxation in carbon nanotube quantum dots”. In: *Physical Review B* 77.23 (2008), p. 235301.
- [18] J Lehmann. “A. Gaita-Arin o, E. Coronado and D. Loss”. In: *Nat. Nanotechnol* 2 (2007), pp. 312–317.
- [19] Michael N Leuenberger and Daniel Loss. “Quantum computing in molecular magnets”. In: *Nature* 410.6830 (2001), pp. 789–793.
- [20] Florian Meier, Jeremy Levy, and Daniel Loss. “Quantum computing with spin cluster qubits”. In: *Physical review letters* 90.4 (2003), p. 047901.
- [21] J Tejada et al. “Magnetic qubits as hardware for quantum computers”. In: *Nanotechnology* 12.2 (2001), p. 181.
- [22] Filippo Troiani et al. “Molecular engineering of antiferromagnetic rings for quantum computation”. In: *Physical review letters* 94.20 (2005), p. 207208.
- [23] Mircea Trif et al. “Spin-electric coupling in molecular magnets”. In: *Physical review letters* 101.21 (2008), p. 217201.
- [24] Guillem Aromí et al. “Design of magnetic coordination complexes for quantum computing”. In: *Chemical Society Reviews* 41.2 (2012), pp. 537–546.

CHAPTER 1. What is a Quantum Bit?

- [25] Matteo Atzori et al. “Quantum coherence times enhancement in vanadium (IV)-based potential molecular qubits: the key role of the vanadyl moiety”. In: *Journal of the American Chemical Society* 138.35 (2016), pp. 11234–11244.
- [26] Lorenzo Tesi et al. “Quantum coherence in a processable vanadyl complex: new tools for the search of molecular spin qubits”. In: *Chemical science* 7.3 (2016), pp. 2074–2083.
- [27] M Bal et al. “Photon-induced magnetization reversal in the Fe 8 single-molecule magnet”. In: *Physical Review B* 70.10 (2004), p. 100408.
- [28] K Petukhov et al. “Magnetization dynamics in the single-molecule magnet Fe 8 under pulsed microwave irradiation”. In: *Physical Review B* 75.6 (2007), p. 064408.
- [29] Arzhang Ardavan et al. “Will spin-relaxation times in molecular magnets permit quantum information processing?” In: *Physical review letters* 98.5 (2007), p. 057201.
- [30] C Schlegel et al. “Direct observation of quantum coherence in single-molecule magnets”. In: *Physical review letters* 101.14 (2008), p. 147203.
- [31] S Bertaina et al. “Rare-earth solid-state qubits”. In: *Nature nanotechnology* 2.39-42 (2007), pp. 1–1.
- [32] RM Rakhmatullin et al. “Coherent spin manipulations in Yb 3+: CaWO 4 at X-and W-band EPR frequencies”. In: *Physical Review B* 79.17 (2009), p. 172408.
- [33] Marc Warner et al. “Potential for spin-based information processing in a thin-film molecular semiconductor”. In: *Nature* 503.7477 (2013), pp. 504–508.

## Part II

# Theoretical background



## Chapter 2

# Spin-orbit coupling

The description of a molecule from the quantum mechanics point of view, i.e. in terms of wave functions, requires the introduction of the Schrödinger equation which describes all the possible state functions of the system[1]. Since there is a large difference between the electron's and nucleus' mass, their motions develop on very different timescale. In other terms, giving the same amount of kinetic energy on nuclei and electrons, the former move much more slowly than the latter. This allows to operate the Born-Oppenheimer approximation expressing the total system eigenfunction as a product of the nuclear eigenstate and the electronic one[1].

$$\psi = \psi_N(\mathbf{R})\psi_e(\mathbf{r}; \mathbf{R}) \quad (2.1)$$

The electronic eigenfunction parametrically depends on the nuclei position, since the electrons still feel the nuclear Coulomb potential corresponding at a certain nuclei position.

The Hamiltonian operator represents the energy corresponding to each wave function and, by applying the Born-Oppenheimer approximation, it can be split in two terms[1]

$$\mathcal{H}^{(0)} = \mathcal{H}_e + \mathcal{H}_N \quad (2.2)$$

$$\mathcal{H}_e = - \sum_{i=1}^n \frac{\hbar^2}{2m_e} \nabla_{\mathbf{r}_i}^2 + \sum_{i=1}^n \sum_{j=1}^N \frac{Z_j e^2}{4\pi\epsilon_0 |\mathbf{r}_i - \mathbf{R}_j|} + \sum_{i=1}^n \sum_{j>i}^n \frac{e^2}{4\pi\epsilon_0 |\mathbf{r}_i - \mathbf{r}_j|} \quad (2.3)$$

$$\mathcal{H}_N = - \sum_{i=1}^N \frac{\hbar^2}{2m_N} \nabla_{\mathbf{R}_i}^2 + \sum_{i=1}^N \sum_{j>i}^N \frac{Z_i Z_j e^2}{4\pi\epsilon_0 |\mathbf{R}_i - \mathbf{R}_j|} \quad (2.4)$$

CHAPTER 2. Spin-orbit coupling

$\mathcal{H}_e$  describes the properties of the electrons under the nuclei's electrostatic potential, it contains the kinetic energy of the electrons, the potential energy arising from the Coulomb electron-electron repulsion and the potential energy coming from the electron-nucleus attraction, whereas  $\mathcal{H}_N$  takes into account the kinetic energy of nuclei and the Coulomb nucleus-nucleus repulsion.

The Schrödinger equation for the sole electrons reads, then, as[1]

$$\mathcal{H}_e \psi_e(\mathbf{r}; \mathbf{R}) = E(\mathbf{R}) \psi_e(\mathbf{r}; \mathbf{R}) \quad (2.5)$$

where also the eigenvalue, i.e. the energy corresponding to the wave function, parametrically depends on the nuclei position.

In the above electron Hamiltonian an additional term has been neglected: the *spin-orbit coupling*. This one accounts for the magnetic interaction between the electron spin magnetic dipole and the magnetic field generated by the orbital motion of the electron[2]

$$\mathcal{H}_{SO} = \sum_{i=1}^n \xi(r_i) L_i \cdot S_i \quad (2.6)$$

In (2.6),  $L_i$  and  $S_i$  are the orbital angular momentum and the spin angular momentum of the  $i$ -th electron, respectively, and  $\xi(r_i)$  contains the dependence on the orbital radial function and the nuclear charge. Under the hypothesis of pure Coulombic central potential, as in the case of a single atom with nuclear charge  $Z$ , the  $\xi(r)$  term can be written as[2]

$$\xi(r) = \frac{1}{2m^2 c^2} \left( \frac{Ze^2}{r^3} \right) \quad (2.7)$$

where  $m$  and  $c$  are the mass of electron and the speed of light, respectively. Under the Russel-Saunders scheme[2], the spin-orbit coupling is small with respect to the other terms of the Hamiltonian, so  $\mathcal{H}_{SO}$  can be considered as a perturbation of the uncoupled Hamiltonian. If  $\psi_{n,\ell,m_\ell,m_s}$  is the eigenfunction defined by the principal quantum number,  $n$ , the azimuthal quantum number,  $\ell$ , the magnetic quantum number,  $m_\ell$ , and the spin quantum number,  $m_s$ , of the unperturbed Hamiltonian  $\mathcal{H}^{(0)}$  and  $E_0$  is its eigenvalue. By using a first-order perturbative approach, the energy levels of  $\mathcal{H} = \mathcal{H}^{(0)} + \mathcal{H}_{SO}$  can be approximated as

$$E = E_0 + \langle \psi_{n,\ell,m_\ell,m_s} | \mathcal{H}_{SO} | \psi_{n,\ell,m_\ell,m_s} \rangle \quad (2.8)$$

Expressing the wave function as product of the radial and the angular part,  $\psi_{n,\ell,m_\ell,m_s} = R_{n,\ell} \Theta_{\ell,m_\ell,m_s}$ , and writing down  $\mathcal{H}_{SO}$  in terms of creation and annihilation operators as follows

$$\mathcal{H}_{SO} = \xi(r) \left( \frac{1}{2}(L_+S_- + L_-S_+) + L_zS_z \right) \quad (2.9)$$

if we consider that  $\xi(r)$  acts only on the radial part of the wave function, whereas the second term of  $\mathcal{H}_{SO}$  acts on the angular one, it results in

$$\langle \psi_{n,\ell,m_\ell,m_s} | \mathcal{H}_{SO} | \psi_{n,\ell,m_\ell,m_s} \rangle = m_\ell m_s \zeta_{n,\ell} \quad (2.10)$$

where

$$\zeta_{n,\ell} = \hbar^2 \int dr r^2 R_{n,\ell}^* \xi(r) R_{n,\ell} \quad (2.11)$$

is the spin-orbit coupling constant.

For hydrogen-like orbitals, the spin-orbit coupling constant can be written as

$$\zeta_{n,\ell} = \frac{1}{8\pi\epsilon_0 m_e^2 c^2 a_0^2} \frac{Z^4 e^2}{n\ell(\ell+1/2)(\ell+1)} \quad (2.12)$$

where  $a_0$  is the Bohr radius. It is worth noting that the spin-orbit coupling constant depends on  $Z^4$ , so it is relatively small for light atoms, but dramatically increases with the atomic number, making the spin-orbit coupling even no more treatable as perturbative effect in case of heavy atoms, such as lanthanides. However, in polyelectronic atoms the single-electron angular momentum operators are often replaced by the corresponding total ones, i.e.  $\mathbf{L}^2$ ,  $\mathbf{S}^2$ ,  $\mathbf{L}_z$ ,  $\mathbf{S}_z$ . In this new picture, the spin-orbit coupling Hamiltonian is rewritten in the following equivalent form[2]

$$\mathcal{H}_{SO} = \lambda \mathbf{L} \cdot \mathbf{S} \quad (2.13)$$

and  $\lambda$  is the average coupling constant for a given  $^{2S+1}L$  spectroscopic term.

*CHAPTER 2. Spin-orbit coupling*



## Chapter 3

# Spin Hamiltonian

The theoretical approach to the study of a spin system requires the introduction of few concepts of second-order perturbation theory[3]. By it the main magnetic interactions can be represented using effective Hamiltonians which include only spin operators, both electronic and nuclear, as well as magnetic field vectors. This is the spin Hamiltonian approach, which is widely used in the interpretation of the EPR spectra. In the following section, we present the most important features of the spin Hamiltonian concerning the transition metal ions coordination compounds and some relationships between the spin Hamiltonian parameters and the electronic structure of the molecules will be outlined.

The quantum mechanical description of Electron Paramagnetic Resonance spectroscopy is considerably simplified by the introduction of the spin Hamiltonian  $\mathcal{H}_s$ , obtained by averaging of the full Hamiltonian over the lattice coordinates and over the spin coordinates of the paired electrons. In the most general case, the spin Hamiltonian has the following form [4]:

$$\mathcal{H}_s = \mathcal{H}_{ze} + \mathcal{H}_{zn} + \mathcal{H}_{zfs} + \mathcal{H}_{SI} + \mathcal{H}_{NQ} \quad (3.1)$$

The interaction of the electronic system with the external magnetic field,  $\mathbf{B}$ , is represented by the Zeeman term

$$\mathcal{H}_{ze} = \mu_B \mathbf{B} \cdot \hat{\mathbf{g}} \cdot \mathbf{S} \quad (3.2)$$

where  $\mu_B$  is the Bohr magneton,  $\mathbf{S}$  is the spin angular momentum operator and  $\hat{\mathbf{g}}$  is the Landé factor tensor.

The nuclear Zeeman term has a form similar to that of (3.2)

$$\mathcal{H}_{zn} = \mu_N \mathbf{B} \cdot \hat{\mathbf{g}}_N \cdot \mathbf{I} \quad (3.3)$$

CHAPTER 3. Spin Hamiltonian

where  $\mu_N$  is the nuclear magneton,  $\mathbf{I}$  is the nuclear spin angular momentum operator. Since  $\mu_B$  is much larger than  $\mu_N$ , the term 3.3 is, generally, neglected.

When there is more than one unpaired electron, their mutual interaction must be taken into account through the zero field splitting Hamiltonian

$$\mathcal{H}_{zfs} = \mathbf{S} \cdot \hat{\mathbf{D}} \cdot \mathbf{S} \quad (3.4)$$

where  $\hat{\mathbf{D}}$  is a symmetric traceless second rank tensor, which is called zero field splitting tensor. This term is different from zero only when  $S > 1/2$  and in symmetry lower than cubic one [4]. The term describing the electron-nucleus interaction is called hyperfine coupling and reads

$$\mathcal{H}_{SI} = \mathbf{S} \cdot \hat{\mathbf{A}} \cdot \mathbf{I} \quad (3.5)$$

in which  $\hat{\mathbf{A}}$  is the hyperfine tensor which is a symmetric matrix. The term describing the nucleus-nucleus interaction is:

$$\mathcal{H}_{NQ} = \mathbf{I} \cdot \hat{\mathbf{Q}} \cdot \mathbf{I} \quad (3.6)$$

but it is generally neglected as the term 3.3.

Interaction of spins with an external magnetic field is defined by  $\mathcal{H}_{ze}$  term, determined by the Landé tensor,  $\hat{\mathbf{g}}$ . By using an appropriate basis, it can be made diagonal, providing the values of the principal directions  $g_x$ ,  $g_y$  and  $g_z$ . In the most general case, they are different from each other, whereas if the system has axial symmetry  $g_x = g_y = g_{\perp}$  and  $g_z = g_{\parallel}$ , while in the cubic symmetry  $g_x = g_y = g_z = g_{iso}$ . The principal values of  $\hat{\mathbf{g}}$  depend on the electronic structure of the paramagnet. In most cases, the ground state of the system has no orbital degeneracy and it is well separated from the first excited states. In this case, second-order perturbation theory provides[5] [6] the following expression for the  $\hat{\mathbf{g}}$  tensor:

$$g_{ij} = g_e \delta_{ij} - 2\lambda \sum_n \frac{\langle g | L_i | n \rangle \langle n | L_j | g \rangle}{E_n - E_g} \quad (3.7)$$

In equation (3.7),  $|g\rangle$  is the spin ground state, whose energy is  $E_g$ ,  $|n\rangle$  is an excited state, whose energy is  $E_n$ ,  $g_e$  is the free-electron  $g$  value equal to 2.0023 and  $\lambda$  is the spin-orbit coupling constant.  $\lambda$  is positive for ions with less than five  $d$  electrons in the valence shell, whereas it is negative for ions with more than five  $d$  electrons, leading to  $g$  values smaller than  $g_e$  for  $d^1$ - $d^4$  ions and larger than  $g_e$  for  $d^6$ - $d^9$  ions. The physical meaning of equation (3.7) is that spin-orbit coupling reintroduces some orbital contribution into the ground state producing deviations of  $g$  from the free-electron value. It is also evident from equation (3.7)

that the deviation from  $g_e$  is larger for ions with larger spin-orbit coupling and small energy separation between the excited and the ground state.

*CHAPTER 3. Spin Hamiltonian*

## Chapter 4

# Theory of spin relaxation

The theory of spin relaxation includes a great number of topics. For this reason, this chapter is devoted to provide just the useful background to understand the main processes which drive the spin relaxation of the compounds investigated in this work. The chapter is mainly based on two reviews: “Electron Spin Relaxation Phenomena in Solids”, *K.J. Stanley and R.A. Vaughan*[7], and “Spin-lattice relaxation in rare-earth salts”, *R. Orbach*[8].

Let us consider a free ion without any interactions, its electronic states are degenerate because the total angular momentum  $\mathbf{J}$  is not zero. As just mentioned in Chapter 2, the total orbital momentum,  $\mathbf{L}$ , and the total spin momentum,  $\mathbf{S}$ , are coupled through the spin-orbit coupling  $\lambda\mathbf{L} \cdot \mathbf{S}$ , defining the total angular momentum as  $\mathbf{J} = \mathbf{L} + \mathbf{S}$  in the Russell-Saunders scheme. When the ion is put in an environment which generates a crystal-field, the degeneracy is partially or totally removed as consequence of the electrostatic interactions between the ion and its neighbour atoms. Interestingly, ions having half-integer spin value and without any interactions able to break the time-reversal symmetry are at least doubly-degenerate, as a consequence of the *Kramers degeneracy theorem*[9]. This means that even the low symmetry of the crystal field is not able to remove the degeneracy of the two levels, named *Kramers doublets* of a  $S = 1/2$  spin system. To split them, it is necessary to apply an external perturbation able to break the time-reversal symmetry, for instance a magnetic field. The spin can be perturbed in a large variety of ways and the application of an external magnetic field represents the most common one. After this perturbation, the spin returns to its equilibrium: this phenomenon is called *relaxation* and can occurs in different ways, either involving the exchange of energy or not. The former case represents the *spin-lattice relaxation*, whether the latter the *spin-spin relaxation*. The spin-lattice relaxation involves an energy transfer between the spin system and the

crystal lattice that hosts it, mediated by the spin-orbit coupling. Whenever the spin is out of the equilibrium, the crystal phonons restore such equilibrium dissipating the energy to the thermal bath. The entire process occurs with a characteristic time  $T_1$  named *spin-lattice relaxation time*. Generally, such time is related to the spin-lattice energy transfer since it represents the rate-determining step of the process, whereas the *lattice-lattice* and *lattice-bath* processes are faster. An exception is represented by the *spin-phonon bottleneck effect*, in which the lattice vibrations are not able to effectively dissipate the energy to the bath, leading to several consequences on the spin dynamics[10]. Concerning the spin-spin relaxation, the process takes place “inside” the spin system, in other words the total spin energy is retained. This effect corresponds to the coherence loss of the transverse magnetization and it is characterized by the *phase memory time*,  $T_m$ .

## 4.1 The spin-lattice relaxation

The lattice vibrations of a crystal can interact with the spin system promoting the spin-lattice relaxation. There are three most important types of mechanisms, schematically represented in Figure 4.1 and listed below:

1. Direct process;
2. Raman process;
3. Orbach process.

By considering transition metals, the direct relaxation process arises from terms in the so-called *effective Hamiltonian* that are linear with the strain i.e. the deformation of the lattice. Such a Hamiltonian is the product of the mixing between the spin-orbit and the orbit-lattice terms, and it couples the spin magnetic dipole to the lattice vibrational modes. Only phonons with energy  $\hbar\omega = \Delta E$ , with  $\Delta E = E_1 - E_0$ , are able to take part in the process. The direct mechanism consists in a spin transition between the excited,  $|1\rangle$ , and the ground,  $|0\rangle$ , states induced by one phonon, whose frequency is resonant with the energy gap,  $\omega_{10} = (E_1 - E_0)/\hbar$ , as the radiative transitions involving single photons. This process is predominant at low temperatures, usually below 20-30 K. At higher temperatures, two-phonons processes start to be relevant in the spin dynamics producing a more pronounced relaxation, since the phonon states start to be populated. In such processes, spin transitions are induced by the absorption of one phonon together with the emission of another one whose frequencies differ exactly by  $\omega_{10}$ . For the two-phonons Raman mechanism the

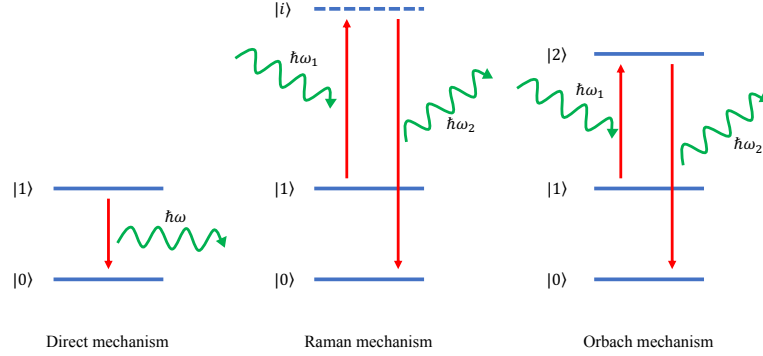


**Figure 4.1:** The three main spin-lattice relaxation processes that occur involving respectively one or two phonons, with frequency  $\omega$  and  $\omega_1, \omega_2$ : Direct, Raman and Orbach mechanism. Such processes will be discussed in detail in this chapter.

effective Hamiltonian is built up using higher order terms, being the orbit-lattice terms taken twice. Thus, the strain appears in the second order, allowing all phonons to take part to the relaxation process. The Raman mechanism involves transitions to and from a virtual excited state, accordingly to its spectroscopic equivalent. The Orbach process is a particular case of Raman one that involves transition to and from real, almost unoccupied, excited states.

#### 4.1.1 The Harmonic lattice

In the classical physics point of view, the atomic displacement produced by an elastic wave propagating through the crystal is

$$u(\mathbf{r}) = u_0 \cos(\mathbf{q} \cdot \mathbf{r} - \omega t) \quad (4.1)$$

where  $u_0$  is the amplitude,  $\mathbf{q}$  is the propagation vector,  $\mathbf{r}$  is the atomic position and  $\omega$  is the frequency of the vibration. According to quantum mechanics, the energy of the phonon is quantized, being

$$E = \left( n + \frac{1}{2} \right) \hbar\omega \quad (4.2)$$

A generally adopted simplification of the theory concerning crystal vibrations accounts for independent modes i.e. one longitudinal and two transverse, that can be described by the following Hamiltonian

$$\mathcal{H}_{ph} = \frac{\hbar}{2} \sum_{i=1}^n [\omega_{i1}(\alpha_i^* \alpha_i + \alpha_i \alpha_i^*) + \omega_{i2}(\beta_i^* \beta_i + \beta_i \beta_i^*) + \omega_{i3}(\gamma_i^* \gamma_i + \gamma_i \gamma_i^*)] \quad (4.3)$$

in which  $\alpha_i$ ,  $\beta_i$  and  $\gamma_i$  are Bose annihilation operators and  $\alpha_i^*$ ,  $\beta_i^*$  and  $\gamma_i^*$  are creation operators. Equation (4.3) takes into account that for the  $i$ -th phonon there are three distinct modes: one longitudinally polarized mode and two orthogonally polarized transverse modes. The Harmonic Hamiltonian can be rewritten as

$$\mathcal{H}_{ph} = \sum_{i=1}^n [\hbar\omega_i \alpha_i^* \alpha_i + \hbar\Omega_i(\beta_i^* \beta_i + \gamma_i^* \gamma_i)] \quad (4.4)$$

where  $\omega_i$  is the frequency of the  $i$ -th longitudinal mode and  $\Omega_i$  is that one related to the  $i$ -th transverse mode. According to the Debye model,  $\omega_i = \Omega_i$ , even if in real materials  $\omega_i > \Omega_i$ , and the dispersion relation of the acoustic modes is proportional to the wave-vector  $\omega = vq$ , where  $v$  is the velocity of sound in the media. By these two assumptions, the Debye model provides the density of states  $\rho(\omega) = 3V\omega^2/2\pi^2\hbar v^3$ . Furthermore, the heat capacity is given by an increasing number of acoustic modes with cut-off frequency  $\omega_D$ , known as Debye frequency.

Lattice vibrations modify the inter-atomic distances time-dependently, thus modulating the crystal-field around the paramagnetic ion. Once the perturbation term of the Hamiltonian is written, the Fermi's Golden rule can be used to calculate the transition probability[7]

$$P_{10} = \frac{2\pi}{\hbar} |\langle 0 | \mathcal{H}_{sl} | 1 \rangle|^2 \rho(E_0) \quad (4.5)$$

in which  $\mathcal{H}_{sl}$  is the spin-lattice Hamiltonian and  $\rho$  the density of the vibrational states. In next sections, the essential features of such relaxation mechanism will be described assuming the crystal as a continuous, isotropic and non-dispersive medium, and adopting the Debye model.

### 4.1.2 The one-phonon process: Direct mechanism

As already mentioned before, the direct mechanism is predominant at low temperatures and it takes place as a result of a spin flip from state  $|1\rangle$  to  $|0\rangle$  with the simultaneous creation of a phonon with frequency  $\hbar\omega = E_1 - E_0 = \delta_{10}$ , ensuring the conservation of energy. The process is schematically shown in Figure 4.2.

Let assume  $N_1$  and  $N_0$  be the population of the spin state  $|1\rangle$  and  $|0\rangle$ , respectively. The spin temperature,  $T_s$  is defined through



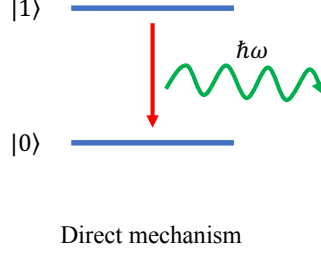


**Figure 4.2:** The direct mechanism. When the spin relaxes back to the ground state, a phonon with frequency  $\hbar\omega = E_1 - E_0 = \delta_{10}$  is emitted.

$$\frac{N_1}{N_0} = e^{-\delta_{10}/k_B T_s} \quad (4.6)$$

In thermal equilibrium  $T_s = T$ , which is the lattice temperature. The lattice is assumed to be in close thermal contact with a bath of infinite thermal capacity at temperature  $T_b$ . When such assumption do not hold, different consideration shall be done as reported in chapter 4.1.5. If the spin system is perturbed so that  $T_s$  becomes greater than  $T$ , the orbit-lattice interaction will induce transitions between the states  $|1\rangle$  and  $|0\rangle$  characterized by a certain rate. From first-order time-dependent perturbation theory, the probability of having a transition between the two spin states is given by[7]

$$P_{10} = \frac{2\pi}{\hbar} |\langle Q_m | \varepsilon | Q_m + 1 \rangle|^2 |\langle 0 | \sum_m V_m | 1 \rangle|^2 \rho(\delta_{10}) \quad (4.7)$$

where  $Q_m$  is the number of phonons in the mode  $m$ ,  $\varepsilon$  is the strain due to the  $m$ -th vibrational mode and  $V_m$  the phonon's operator responsible of the spin flipping. Since the mechanism under consideration is a one-phonon process, the energy conservation is achieved creating one phonon,  $Q_m + 1$ . In other words, the transition takes place between the two spin-phonon states  $|1, Q_m\rangle$  and  $|0, Q_m + 1\rangle$ . The occupation number of the phonon mode is assumed to have its thermal equilibrium value

$$Q_m = \left[ e^{\delta_{10}/k_B T} - 1 \right]^{-1} \quad (4.8)$$

while the density of phonon states  $\rho(\delta_{10})$  is given by the classical expression from the Debye model

$$\rho(\delta_{10}) = \frac{3V\delta_{10}^2}{2\pi^2\hbar^3 v^3} \quad (4.9)$$

where the crystal has volume  $V$  and velocity of sound  $v$ . For simplicity,  $v$  is

assumed to be the same in all the directions. Thus the transition probability can be rewritten as

$$\begin{aligned} P_{10} &= \frac{2\pi}{\hbar} \left[ \frac{(Q_m + 1)\delta_{10}}{2Mv^2} \frac{3V\delta_{10}^2}{2\pi\hbar^3v^3} \right] |\langle 0 | \sum_m V_m | 1 \rangle|^2 \\ &= \frac{3}{2\hbar} \left( \frac{\delta_{10}}{\hbar} \right)^3 \frac{Q_m + 1}{\rho\hbar v^5} W_D^2 \end{aligned} \quad (4.10)$$

where  $\rho$  is the density of the crystal and  $W_D^2$  stands for  $|\langle 0 | \sum_m V_m | 1 \rangle|^2$ . Similarly

$$P_{01} = \frac{3}{2\hbar} \left( \frac{\delta_{10}}{\hbar} \right)^3 \frac{Q_m}{\rho\hbar v^5} W_D^2 \quad (4.11)$$

By calculating the rate equation of the population and defining

$$T_1 = \frac{1}{P_{10} + P_{01}} \quad (4.12)$$

the spin-lattice relaxation time for the direct mechanism takes the following form

$$\frac{1}{T_1^D} = \frac{3}{2\pi} \left( \frac{\delta_{10}}{\hbar} \right)^3 \frac{\coth(\delta_{10}/2k_B T)}{\rho\hbar v^5} W_D^2 \quad (4.13)$$

and when  $\delta_{10} \ll 2k_B T$ ,  $\coth(\delta_{10}/2k_B T) \rightarrow k_B T/\delta_{10}$ , equation (4.13) reads

$$\frac{1}{T_1^D} = \frac{3\delta_{10}^2 k_B T}{\pi\hbar^4 v^5 \rho} W_D^2 \quad (4.14)$$

From equation (4.14) it follows that the spin-lattice relaxation time for the direct process becomes roughly proportional to  $T^{-1}$ . In the opposite condition, when  $\delta_{10} \gg 2k_B T$ ,  $T_1^D$  tends to be temperature independent, though this case hardly occurs. The Equation (4.14) cannot be applied directly in case of Kramers doublets, since they are not coupled to the crystal field, unless some other interaction lifts their degeneracy. Accordingly, the matrix elements of  $W_D$  are identically zero and no direct relaxation occurs between the levels of a Kramers doublet in zero magnetic field. The application of an external magnetic field,  $B$ , splits the doublet making the two spin states susceptible to the lattice strains through the modulation of the Landé splitting tensor,  $g$ . The resulting  $W_D$  is now proportional to  $B$ , and when  $k_B T > \delta_{10} \propto B$ , the spin-lattice relaxation time in equation (4.14) becomes proportional to  $H^{-4}T^{-1}$ .

### 4.1.3 The two-phonons process: Raman mechanism

The Raman mechanism belongs to the group of spin-lattice relaxation processes which involves two phonon, as shown in Figure 4.3. It results in the simultaneous creation and destruction of a pair of phonons having a difference in energy equal to those of the spin system,  $\delta_{10}$ . In other words, two phonons  $m$  and  $n$  whose frequency is  $\omega_m$  and  $\omega_n$ , combine non-linearly causing the spin transition, since the energy balance of the entire process is

$$\hbar\omega_m - \hbar\omega_n = \delta_{10} \quad (4.15)$$

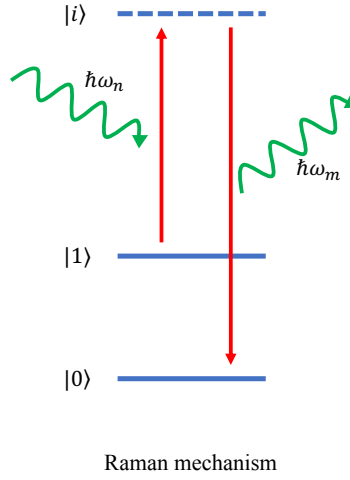


**Figure 4.3:** The Raman mechanism. It involves the simultaneous absorption and emission of two phonons, whose difference in energy is resonant with the spin transition.

The phonon  $n$  is absorbed by the spin system in its excited state  $|1\rangle$ , promoting the transition to the virtual state  $|i\rangle$ , followed by the emission of the phonon  $m$  and the simultaneous transition to the spin ground state  $|0\rangle$ . In case of non-Kramers systems, it can be demonstrated that the relaxation time can be approximated to[7]

$$\frac{1}{T_1^R} \propto \frac{1}{\rho^2 v^{10} \Delta_i^2} \left( \frac{k_B T}{\hbar} \right)^7 \left| \sum_{m,n} \langle 0 | V_m | i \rangle \langle i | V_n | 1 \rangle \right|^2 \quad (4.16)$$

in which  $\rho$  is the crystal density,  $v$  the velocity of sound and  $\Delta_i$  is the energy difference between the virtual state  $|i\rangle$  and the spin ground state  $|0\rangle$ . Such result holds for  $k_B \theta_D \ll \Delta_i$ , where  $\theta_D$  is the Debye temperature.

In the case of Kramers system, there are two time-conjugated doublets  $|0\rangle$ ,  $|1\rangle$  and  $|0'\rangle$ ,  $|1'\rangle$  separated by an energy gap  $\Delta_i$ . This excited doublet can act as

the state  $|i\rangle$  and the resulting  $T_1^R$  is

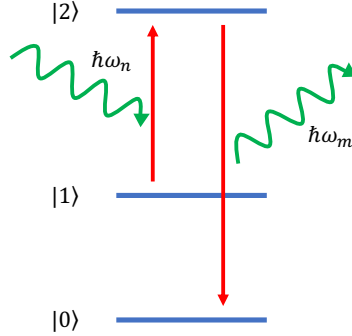
$$\frac{1}{T_1^R} \propto \frac{1}{\rho^2 v^{10} \Delta_i^4} \left( \frac{k_B T}{\hbar} \right)^9 \left| \sum_{m,n} \langle 0 | V_m | i \rangle \langle i | V_n | 1 \rangle \right|^2 \quad (4.17)$$

Kramers systems are particularly relevant for this work, since the investigated materials belong to them. However, they show a weaker temperature dependence of  $T_1$ , as discussed in chapter 9.

#### 4.1.4 Resonant Raman process: Orbach mechanism

The description of this process as a resonant version of the Raman one was given for the first time by R. Orbach in 1961[8]. In such a case, the state  $|i\rangle = |2\rangle$  is a real state and the phonons  $m$  and  $n$  are resonant with it, see figure 4.4. Considering the third state,  $|2\rangle$ , being relatively close in energy to the excited state  $|1\rangle$ , therefore  $k_B \theta_D > \Delta_2$ , and the spin-lattice relaxation time results

$$\frac{1}{T_1^O} \propto \frac{1}{\rho v^5} \left( \frac{\Delta_2}{\hbar} \right)^3 \left( e^{\Delta_2/k_B T} - 1 \right)^{-1} \frac{\left| \sum_{n,m} \langle 0 | V_m | 2 \rangle \langle 2 | V_n | 1 \rangle \right|^2}{\left| \sum_m \langle 0 | V_m | 2 \rangle \right|^2 + \left| \sum_n \langle 2 | V_n | 1 \rangle \right|^2} \quad (4.18)$$



Orbach mechanism

**Figure 4.4:** The Orbach mechanism. This process is similar to the Raman one, but in this case the state  $|2\rangle$  is a real excited state of the spin system, and the two phonons  $m$  and  $n$  are resonant with it.

Generally it is possible to assume that  $\Delta_2 > k_B T$ , therefore the spin-lattice relaxation rate for the Orbach mechanism follows an exponential decay as a function of temperature

$$\frac{1}{T_1^O} \propto e^{-\Delta_2/k_B T} \quad (4.19)$$

Such results hold for both Kramers and non-Kramers systems.

#### 4.1.5 The spin-phonon Bottleneck effect

In chapter 4.1.2, it was assumed that the orbit-lattice interaction was the rate-determining step in the spin-lattice relaxation. However, if the lattice is not able to dissipate the energy released by the spin transition from the excited state toward the ground one, a significant change in the lattice temperature may occur. At low temperature, the heat capacity of spins is commonly greater than that of the lattice modes involved in the relaxation, but this assumption is valid only if the energy can be transferred rapidly from the lattice vibrations to either the bath or the remaining crystal modes. Van Vleck pointed out that such transfers can be so slow as to limit the whole energy flow from the spin to the bath, when the relaxation is induced by direct mechanism[10][11]. This occurs because the energy can be only transferred from the spins to few phonons whose frequency is resonant with the spin levels energy gap. Such a hindrance becomes more important in high density spin systems, or when the size of crystal is quite large, being increasingly probable that a spin resonant phonon will be absorbed by another spin before it is dissipated to the bath. This restriction of spin-lattice relaxation by a “phonon bottleneck” has been observed in many systems, including those relaxing through the Orbach process. The simplest model of spin-phonon bottleneck treats the spin system as affecting equally all lattice modes within a narrow band of frequency  $\Delta\omega$ , centred at the frequency of a spin resonance line and corresponding roughly to its width. If this spin resonance band results from transitions between a spin state  $|0\rangle$  and a higher state  $|1\rangle$  with populations respectively  $N_0$  and  $N_1$ , the net rate at which phonons are created through single-phonon transitions, i.e. direct mechanism, is

$$R_{sl} = -N_0 P_{01} + N_1 P_{10} \quad (4.20)$$

If the average number of phonons per mode is  $n$ , the spin-lattice relaxation rate can be rewritten as

$$R_{sl} = \frac{P_{01}^0}{n_0} [(n+1)N_1 - nN_0] \quad (4.21)$$

where  $P_{01}^0$  and  $n_0$  are the values that would occur in absence of the bottleneck effect, i.e. when the system is at the thermal equilibrium.

The net rate at which phonons at frequencies  $\Delta\omega$  relax into the bath or into

other modes is

$$R_{lb} = (n - n_0) \rho(\omega_{01}) \Delta\omega \tau_p^{-1} \quad (4.22)$$

where  $\rho(\omega_{01})\Delta\omega$  represents the number of available vibrational modes resonant with the spin transition and  $\tau_p$  is the excited phonon lifetime within the band  $\Delta\omega$ . The energy stored by those modes may almost always be neglected and  $R_{sl}$  be set equal to  $R_{lb}$  for the entire relaxation. By arranging equations (4.21) and (4.22), a further relaxation term due to the bottleneck effect appears evident and it can be written as

$$R_{sl} = R_{sl}^0 \left[ 1 + A \left( \frac{N_0 - N_1}{N} \right) \right]^{-1} \quad (4.23)$$

in which  $R_{sl}^0$  stands for the net transition rate without bottleneck effect,  $N$  is the total number of spins inside the crystal and

$$A = \frac{N \tau_p P_{01}^0}{\rho(\omega_{01}) \Delta\omega n_0} = \frac{\pi W_D^2 \delta_{01} N \tau_p}{\hbar^2 \Delta\omega \rho v^2} \quad (4.24)$$

where  $\rho$  and  $v$  are the density of the crystal and the velocity of sound, respectively. The effect of phonon bottleneck is thus equivalent to the reduction of the transition probabilities  $P_{01}$  and  $P_{10}$  by a factor  $[1 + A(N_0 - N_1)/N]^{-1}$ .

It is worth noting that different types of bottleneck effects can occur. These can be divided either in “spatial bottleneck”, where the rate-determining process is the transfer of energy in space, or in “spectral bottleneck”, where the transfer of energy in frequency is the rate-determining step. In the former case, when the crystal volume is large compared with the phonon mean free path,  $v \cdot \tau_p$ , the bottleneck is particularly severe. Thus, it is clearly evident that there is a strong dependence of the spin-phonon bottleneck effect upon the crystal size. This is particularly relevant in chapter 9.1.

In this section it has discussed the case in which spin-phonon bottleneck effects influence the direct relaxation process. It should be stressed that these are not expected to influence the Raman process, since it involves a wide spectrum of lattice frequencies. However, the Orbach process, which in a simplified view corresponds to a double-step direct process, uses two narrow bands of lattice modes, for which bottleneck effects may be present. This case is, however, not discussed in the dissertation since Orbach mechanisms are not expected to be active in the relaxation of the investigated molecules.

## 4.2 The spin-spin relaxation

Belong to this category all phenomena that adiabatically decrease the transverse magnetization, i.e. which affect the spin-spin relaxation time  $T_2$ . These processes originate from *dipolar interactions* between electronic spins and/or electronic and nuclear spins surrounding the reference electronic spin. In discussing this type of relaxation, it is useful to employ the Electron Paramagnetic Resonance terminology[12].

In general, every electronic spin flip affects the coherence of other electronic spins through the dipolar interaction. This decoherence phenomenon can be reduced by increasing the distance among spins, i.e. by diluting the magnetic system, for example in a lattice of isostructural diamagnetic molecules. However, even in this case, when magnetically diluted electron spins are surrounded by magnetically concentrated nuclear spins, spin dephasing is dominated by *nuclear spin diffusion*. Such a process consists in nuclear spin flips that modulate the electron-nuclear dipolar interaction, with the consequent loss of spin coherence in the  $xy$ -plane. Even if the nuclear spin flips are relatively slow compared to the electronic spin ones, the large number of nuclei that are dipole-coupled with the electron spin makes this effect the major contribution to the coherence time[13]. This has been demonstrated by replacing ligand and/or solvent hydrogen atoms with deuterium atoms or with spin nuclear free elements, which have smaller or no magnetic moments. Indeed, this has led to an enhancement of the relaxation time  $T_2$ . The nuclear spin diffusion process exhibits weak or no temperature dependence and it is independent from the magnetic field.

Spin coherence in the  $xy$ -plane cannot be longer than the relaxation along the  $z$ -axis, and thus  $T_1$  represents an upper limit of  $T_2$ . This introduces a temperature dependence on spin-spin relaxation time, which becomes then temperature dependent according to the thermal behaviour of  $T_1$ . However, this is not the only phenomenon that can provide a temperature dependence for  $T_2$ . Indeed, the spin-spin relaxation depends on temperature when dominated by motional processes. These can be either tumbling of the molecule that averages  $\mathbf{g}$  and  $\mathbf{A}$  anisotropy, or internal motions such as rotation of methyl groups or ring inversions that interchange axial and equatorial substituents. Such effects are reduced when working in solid-state phase rather than in solution.

It should be noted that usually, instead of the spin-spin relaxation time,  $T_2$ , the spin-echo dephasing time i.e. the phase memory time,  $T_m$ , is measured, since it is easier to obtain. This encompasses all processes that disturb electron spin phase coherence and can be considered a lower limit of  $T_2$ [14][15].

*CHAPTER 4. Theory of spin relaxation*



## Chapter 5

# Spin-phonon dynamics theory

The dynamics of a spins ensemble is critically entangled with the degrees of freedom of the lattice which hosts it. More explicitly, it follows the total Hamiltonian [16]

$$\mathcal{H} = \mathcal{H}_s + \mathcal{H}_{ph} + \mathcal{H}_{s-ph} \quad (5.1)$$

In the case of a  $S = 1/2$  spin molecular system, the spin Hamiltonian will contain only the Zeeman and the hyperfine coupling term as well as the dipolar coupling between the spin of different molecules

$$\mathcal{H}_s = \mu_B \mathbf{B} \cdot \hat{\mathbf{g}} \cdot \mathbf{S} + \mathbf{S} \cdot \hat{\mathbf{A}} \cdot \mathbf{I} + \mathbf{S} \cdot \hat{\mathbf{D}}_{dip} \cdot \mathbf{S} \quad (5.2)$$

where  $\hat{\mathbf{D}}_{dip}$  is the dipole interaction tensor and  $\mathbf{S}$  and  $\mathbf{I}$  are the electron and the nuclear spin respectively. The spin dynamics can be described in term of the spin density matrix,  $\rho^s$ , and the Liouville equation

$$\frac{d\rho^s}{dt} = -\frac{i}{\hbar} [\mathcal{H}_s, \rho^s] \quad (5.3)$$

If we consider the crystal lattice defined by a set of reciprocal lattice vectors,  $\mathbf{q}$ , and  $N$  atoms in the unit cell, its dynamics results in periodic displacement waves, i.e. phonons,  $Q_{\alpha\mathbf{q}}$ , with frequency  $\omega_{\alpha\mathbf{q}}$ , described by the following harmonic Hamiltonian

$$\mathcal{H}_{ph} = \sum_{\alpha\mathbf{q}} \hbar\omega_{\alpha\mathbf{q}} \left( n_{\alpha\mathbf{q}} + \frac{1}{2} \right) \quad (5.4)$$

in which  $n_{\alpha\mathbf{q}}$  is the phonons occupation number. The spin-phonon coupling Hamiltonian is responsible for the energy exchange between spins and lattice through the spin-orbit coupling, except for the dipolar contribution, and reads

$$\mathcal{H}_{s-ph} = \sum_{\alpha\mathbf{q}} \left( \frac{\partial \mathcal{H}_s}{\partial Q_{\alpha\mathbf{q}}} \right) Q_{\alpha\mathbf{q}} \quad (5.5)$$

Generally, we can assume that the phonons and the spin dynamics occur at extremely different time scales. The unique limitation to such approximation is due to the phonon-bottleneck effect[17], which has been treated in chapter 4.1.5. However, if this effect is not present, the phonons can be considered to be always at the thermal equilibrium, being in the so called Born-Markov approximation. According to these hypotheses, the time evolution of the spin density matrix is ruled by the Redfield equation[18]

$$\frac{d\rho_{ab}^s(t)}{dt} = \sum_{cd} e^{i(\omega_{ac} + \omega_{bd})t} R_{cd}^{ab} \rho_{cd}^s(t) \quad (5.6)$$

where  $R_{cd}^{ab}$  represents the transition rate between the elements of the spin density matrix and reads

$$R_{cd}^{ab} \propto \frac{\pi}{2\hbar^2} \sum_{\alpha\mathbf{q}} V_{ac}^{\alpha\mathbf{q}} V_{bd}^{\alpha-\mathbf{q}} [G(\omega_{bd}, \omega_{\alpha\mathbf{q}}) + G(\omega_{ac}, \omega_{\alpha\mathbf{q}})] \quad (5.7)$$

in which  $V_{ac}^{\alpha\mathbf{q}}$  represents the matrix element of the spin-phonon Hamiltonian in the spin Hamiltonian eigenfunctions basis

$$V_{ac}^{\alpha\mathbf{q}} = \langle a | \frac{\partial \mathcal{H}_s}{\partial Q_{\alpha\mathbf{q}}} | b \rangle \quad (5.8)$$

and  $G(\omega_{ij}, \omega_{\alpha\mathbf{q}})$  is the Fourier transform of the single phonon correlation function at finite temperature. In the harmonic lattice approximation, it is defined as

$$G(\omega_{ij}, \omega_{\alpha\mathbf{q}}) = \bar{n}_{\alpha\mathbf{q}} \delta(\omega_{\alpha\mathbf{q}} - \omega_{ij}) + (\bar{n}_{\alpha\mathbf{q}} + 1) \delta(\omega_{\alpha\mathbf{q}} + \omega_{ij}) \quad (5.9)$$

where  $\bar{n}_{\alpha\mathbf{q}}$  is the Bose-Einstein population at a temperature T.

In the case that lattice anharmonic interactions cannot be neglected, the finite phonon's lifetime  $2\pi\Delta_{\alpha\mathbf{q}}^{-1}$  must be included in the model, giving  $G(\omega_{ij}, \omega_{\alpha\mathbf{q}})$  the usual Lorentzian line shape

$$G(\omega_{ij}, \omega_{\alpha\mathbf{q}}) = \frac{1}{\pi} \left[ \frac{\Delta_{\alpha\mathbf{q}}}{\Delta_{\alpha\mathbf{q}}^2 + (\omega_{ij} - \omega_{\alpha\mathbf{q}})^2} \bar{n}_{\alpha\mathbf{q}} + \frac{\Delta_{\alpha\mathbf{q}}}{\Delta_{\alpha\mathbf{q}}^2 + (\omega_{ij} + \omega_{\alpha\mathbf{q}})^2} (\bar{n}_{\alpha\mathbf{q}} + 1) \right] \quad (5.10)$$

By solving (5.6), the magnetization dynamics for the i-th spin can be calculated by using the expression  $\mathbf{M}(i) = Tr\{\rho^s(t)\mathbf{S}(i)\}$ .

Let us focus on the spin-phonon coupling term contained in (5.8). It can be

developed as follow

$$\frac{\partial \mathcal{H}_s(i)}{\partial Q_{\alpha\mathbf{q}}} = \mu_B \mathbf{B} \cdot \frac{\partial \hat{\mathbf{g}}(i)}{\partial Q_{\alpha\mathbf{q}}} \cdot \mathbf{S}(i) + \mathbf{S}(i) \cdot \frac{\partial \hat{\mathbf{A}}(ii)}{\partial Q_{\alpha\mathbf{q}}} \cdot \mathbf{I}(i) + \sum_{j=1}^{N_s} \mathbf{S}(i) \cdot \frac{\partial \hat{\mathbf{D}}_{dip}(ij)}{\partial Q_{\alpha\mathbf{q}}} \cdot \mathbf{S}(j) \quad (5.11)$$

The  $\hat{\mathbf{g}}$  and the  $\hat{\mathbf{A}}$  tensors are strongly dependent on the spin-orbit coupling[3][19] having, therefore, a “local” character, which means that the first two terms of equation (5.11) are only influenced by localized intramolecular vibrations[20]. On the contrary, since dipolar interaction take into account how the  $i$ -th spin experiences the other ones, the  $\hat{\mathbf{D}}_{dip}$  tensor is also dependent on molecular translation[20] i.e. phonons.

In the absence of spin-spin interaction for highly magnetically diluted systems, spin relaxation can only occurs through the modulation of the spin Hamiltonian by local rotations and intramolecular distortions. However, for a 1/2 spin molecular system in a reasonable external magnetic field, the Zeeman splitting is much smaller than the energy of the first optical modes, suggesting that only acoustic modes can be responsible for the spin relaxation through spin-phonon interaction. The answer to this apparently complicated dilemma comes from the in-depth analysis of the nature of the phonons through their decomposition into molecular translations, rotations and intramolecular distortions: at low frequency, both the acoustic and the optical modes have a hybrid *internal-external nature* giving rise to an efficient relaxation pathway even for a isolated single spin[16]. The presence of internal components in the low-energy phonons can be rationalized in term of mixing between rigid lattice translations and soft molecular modes.

If we limit our study to the case of a spin 1/2 in the presence of an external magnetic field, the hyperfine and the dipolar interaction terms of equation (5.11) can be neglected since in high magnetic fields their contribute is negligible. The spin-phonon coupling coefficients are defined as the derivatives of the spin Hamiltonian terms with respect to the atomic displacements, generally described in terms of normal modes of vibration, as in equation (5.11). However, it is also possible to perform a differentiation in terms of Cartesian coordinates,  $X_{iv}$ , where the coefficients  $i$  and  $v$  run over the atoms and the Cartesian coordinates, respectively[16]. This choice allows to focus on the sole contribution coming from the geometrical distortions. According to this definition, the spin-phonon coupling coefficients are

$$\partial g = \left( \frac{\partial g_{st}}{\partial X_{iv}} \right)_0 \quad (5.12)$$

where the indexes  $s$  and  $t$  run on the three Cartesian coordinates of the

g-tensor and the subscript 0 refers to the derivatives taken at the equilibrium geometry. It is also useful to introduce a molecular-average spin-phonon coupling coefficient as[21]

$$\|\partial g\| = \sum_{i,v}^{M,3} \sum_{s,t}^3 \left( \frac{\partial g_{st}}{\partial X_{iv}} \right)_0^2 \quad (5.13)$$

Recently, a comparative study on a class of Vanadium(IV) coordination compounds[20] has been demonstrated the effect of intermolecular and intramolecular vibrations on the modulation of the Zeeman energy. It has been carried out on four Vanadium(IV)-based complexes, two of them have a pentacoordinated pyramidal geometry and the other two have a hexacoordinated octahedral geometry. The study provides the first insight into the fundamental role played by the coordination geometry and the ligand-field strength in determining the spin-phonon coupling intensity and, consequently, the spin-lattice relaxation time of molecular Qubits. It has been found that the vanadyl-based molecules, having the pyramidal coordination geometry, have low energy-lying vibrational modes with lower average internal contribution, leading to a weaker spin-phonon coupling and longer  $T_1$  with the respect to octahedral ones.

*Lunghi A.* [21] has done an interesting study on the ligand-field contributions to the spin-phonon coupling in a series of Vanadium(IV) molecular complexes in the high external field regime, i.e. when the spin Hamiltonian coincides with the sole Zeeman term. The catecholate ligand donor atoms are changed from Oxygen to Sulphur, Selenium and Tellurium. This work shed light on the correlation between the deviation of the g-parameter from the free-electron value and the average spin-phonon coupling coefficients, displaying the fundamental role of spin-orbit coupling, chemical bond covalency and energy splitting of the  $d$  orbitals in spin relaxation. By using the ligand-field theory, it is possible to obtain the formula (5.14) which correlate the spin-phonon coupling coefficient magnitude to several “chemical” parameters.

$$\left( \frac{\partial g_{xx}}{\partial X_{iv}} \right)_0 = -\frac{\delta g_{xx}}{\Delta} \left( \frac{\partial \Delta}{\partial X_{iv}} \right)_0 \quad (5.14)$$

In equation (5.14),  $\delta g_{xx}$  represents the shift from the free electron value and  $\Delta$  is the energy gap between the excited and ground state. It states that the magnitude of the spin-phonon coupling coefficients is linearly dependent from the g-shift, which is directly linked to the strength of the spin-orbit coupling, it is inversely proportional to the energy difference between the excited state and the ground one and it is also proportional to the energy gap modulation with respect to the atomic displacements, i.e. the geometrical distortions.

## 5.1 Some useful numbers

In table 5.1, the order of magnitude of some physical quantities essential in the understanding of this manuscript are reported. As it is shown, the dynamics of spins and phonons develop on strongly different timescales being the former 4-6 orders of magnitude longer compared to the latter.

Physical quantities of interest	10 K	100 K
Spin lifetimes	1-10 ms	1-100 $\mu$ s
Spin coherence times	1-10 $\mu$ s	0.1-1 $\mu$ s
Phonon lifetimes	0.1-10 ns	1-100 ps

**Table 5.1:** Order of magnitude of some physical quantities of interest at 10 and 100 K.

## References

- [1] Donald Allan McQuarrie and John Douglas Simon. *Physical chemistry: a molecular approach*. Vol. 1. University science books Sausalito, CA, 1997.
- [2] Russel S. Drago. *Physical Methods for Chemists*. Surfside Scientific Publisher, 1977.
- [3] Dante Gatteschi, Roberta Sessoli, and Jacques Villain. *Molecular nanomagnets*. Vol. 5. Oxford University Press on Demand, 2006.
- [4] Edward I. Solomon and A. B. P. Lever. *Inorganic Electronic Structure and Spectroscopy, Volume 1: Methodology*. John Wiley & Sons, Inc., 1999.
- [5] M.H.L. Pryce. “A modified perturbation procedure for a problem in paramagnetism”. In: *Proceedings of the Physical Society. Section A* 63.1 (1950), p. 25.
- [6] John Stanley Griffith. *The theory of transition-metal ions*. Cambridge University Press, 1964.
- [7] Kenneth Jack Standley. *Electron spin relaxation phenomena in solids*. Springer, 2013.
- [8] R Orbach. “Spin-lattice relaxation in rare-earth salts”. In: *Proceedings of the Royal Society of London. Series A. Mathematical and Physical Sciences* 264.1319 (1961), pp. 458–484.
- [9] Hendrik Antoon Kramers. “Théorie générale de la rotation paramagnétique dans les cristaux”. In: *Proc. Acad. Amst* 33.6 (1930).

- [10] J. H. Van Vleck. “Paramagnetic Relaxation and the Equilibrium of Lattice Oscillators”. In: *Phys. Rev.* 59 (9 May 1941), pp. 724–729. DOI: 10.1103/PhysRev.59.724. URL: <https://link.aps.org/doi/10.1103/PhysRev.59.724>.
- [11] JH Van Vleck. “Calculation of energy exchange between lattice oscillators”. In: *Physical Review* 59.9 (1941), p. 730.
- [12] Arthur Schweiger and Gunnar Jeschke. *Principles of pulse electron paramagnetic resonance*. Oxford University Press on Demand, 2001.
- [13] S Lenz et al. “Quantitative prediction of nuclear-spin-diffusion-limited coherence times of molecular quantum bits based on copper (ii)”. In: *Chemical Communications* 53.32 (2017), pp. 4477–4480.
- [14] Sandra S Eaton and Gareth R Eaton. “Relaxation Mechanisms”. In: *EMagRes* (2007), pp. 1543–1556.
- [15] Sushil K Misra. “Relaxation of paramagnetic spins”. In: *Multifrequency Electron Paramagnetic Resonance: Theory and Applications* (2011), pp. 455–495.
- [16] Alessandro Lunghi and Stefano Sanvito. “How do phonons relax molecular spins?” In: *Science Advances* 5.9 (2019). ISSN: 23752548. DOI: 10.1126/sciadv.aax7163. URL: <http://advances.sciencemag.org/>.
- [17] L. Tesi et al. “Giant spin-phonon bottleneck effects in evaporable vanadyl-based molecules with long spin coherence”. In: *Dalton Transactions* 45.42 (2016), pp. 16635–16643. ISSN: 14779234. DOI: 10.1039/c6dt02559e.
- [18] Heinz-Peter Breuer, Francesco Petruccione, et al. *The theory of open quantum systems*. Oxford University Press on Demand, 2002.
- [19] Frank Neese. “Calculation of the zero-field splitting tensor on the basis of hybrid density functional and Hartree-Fock theory”. In: *The Journal of chemical physics* 127.16 (2007), p. 164112.
- [20] Andrea Albino et al. “First-Principles Investigation of Spin–Phonon Coupling in Vanadium-Based Molecular Spin Quantum Bits”. In: *Inorganic chemistry* 58.15 (2019), pp. 10260–10268.
- [21] Alessandro Lunghi. “Ligand-field contributions to spin-phonon coupling in a family of Vanadium molecular qubits from multi-reference electronic structure theory”. In: (Dec. 2019), pp. 1–8. arXiv: 1912.04545. URL: <http://arxiv.org/abs/1912.04545>.

## Part III

# Experimental section





In this part the experimental setups as well as the sample preparation will be presented. The reader will find three chapters, the first is devoted to the discussion of the two THz time-domain spectroscopy setups, one based on photoconductive antennas and the other on plasma generation of THz radiation and Air-Biased Coherent Detection (ABCD), and the raw-data analysis procedure. The second is dedicated to the discussion of the technical aspects of the Time-resolved THz-pump EPR-probe experiment (hereafter TR-THz-EPR) performed at the International Tomography Center and the Free Electron Laser facility of Novosibirsk. The third will discuss the sample preparation. The more performing THz setup, namely that uses the plasma generation and ABCD, has been realized during the second year of PhD in order to achieve a wider spectral window. Moreover, the features of this setup, such as the high-power laser source, allow to plan further implementations as the realization of time-resolved IR-pump THz-probe experiment to get insights into, for instance, the effect of the excitation of a molecular vibration on the phonon structure of the material. Moreover, in the last section of chapter 1 the first experimental results achieved by the plasma-based THz-TDS will be disclosed. The latter has been carried out on liquid water which represents a good test-bed since it is one of the most studied materials in last decades.



## Chapter 6

# Time Domain THz Spectroscopy

### 6.1 Set-up based on photoconductive antennas

The THz-TDS set-up based on photoconductive antennas allows very high signal to noise ratio measurements. It has a frequency window starting from 0.1 up to 4 THz, namely  $3\text{-}130\text{ cm}^{-1}$ . It is able to work both in transmission or reflection configuration. All the samples measured in this work have been measured in the former disposition.

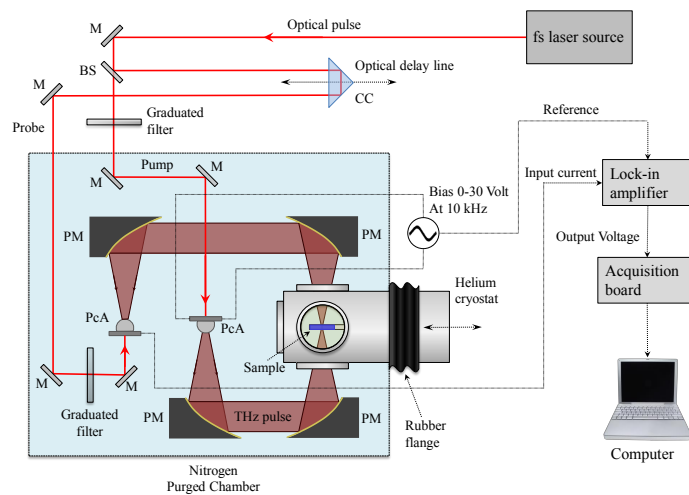


**Figure 6.1:** THz-TDS experimental setup. M: mirror, BS: beam-splitter, CC: corner cube, PM: parabolic mirror, PcA: photoconductive antenna.

## CHAPTER 6. Time Domain THz Spectroscopy

A sketch of the set-up is shown in figure 6.1. Laser pulses (780 nm wavelength, 120 fs duration, 100 MHz repetition rate) produced by a fiber T-light laser by MenloSystem are splitted in two beams called pump and probe ones. The former feeds a low-temperature GaAs photoconductive antenna (PcA) which works as source of THz radiation. The antenna (figure 6.2) is composed by a single dipole of GaAs biased by a 10 kHz sinusoidal 0-30 V voltage. When the laser pulse hits the semiconductor, several free-charges are generated and immediately accelerated by the applied voltage. The electric field in the THz region can be expressed by equation 6.1:

$$E_{THz}(t) \propto \frac{\partial J(t)}{\partial t} \quad (6.1)$$

where  $J(t)$  represents the current density: the more is the time-variation of  $J(t)$  the broader is the emitted THz radiation.

The emitted vertically polarized THz field is efficiently extracted and collected by a hemispheric silicon lens and then collimated and focalized on the sample by a couple of gold-coated 90° off-axis parabolic mirrors (PMs). In order to reduce optical aberrations, the two PMs are symmetrically placed with the respect to the vertical plane between them[1]. A second couple of PMs collects the transmitted field and focalizes it on a another PcA working as detector. The probe pulse, is also brought on the PcA to create free charges that are accelerated by the oscillating THz field resulting in a photocurrent whose intensity is related to the amplitude of the THz field.

The probe pulse is conveniently delayed respect to the pump one to sample the THz field at different times reconstructing the whole time evolution of the THz pulse. The photocurrent is amplified by a lock-in amplifier and recorded by a digital acquisition system. The whole THz set-up is placed inside a nitrogen purged chamber to avoid the absorption of the water vapour.

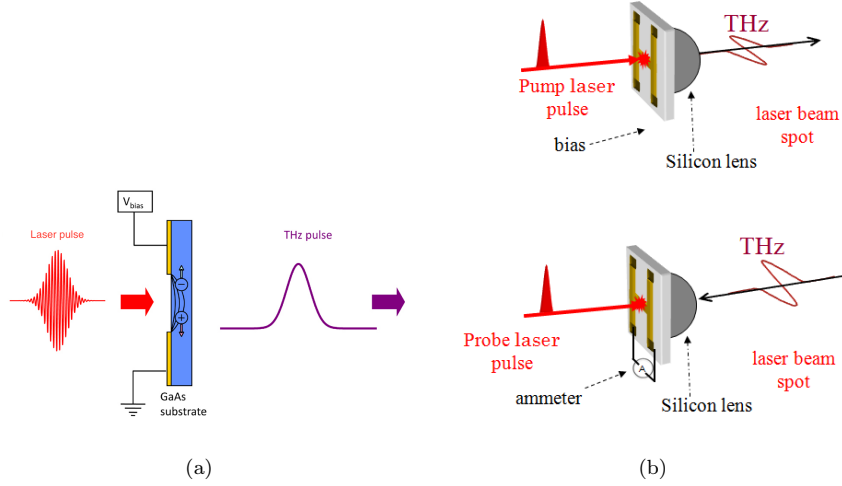


**Figure 6.2:** (a) Free-charges generated by the laser pulse. These are accelerated by the applied voltage generating the THz pulse. (b) On the top: photoconductive antenna working as horizontally-polarized THz source. On the bottom: photoconductive antenna working as THz detector.

## 6.2 Set-up based on plasma and ABC detection

The experiment uses air plasma created by two-color femtosecond laser pulses as THz source and Air-Biased Coherent Detection (ABCD). This allows to gain an ultra-broadband spectrum ranging from 0.5 up to 15 THz, namely from ca. 15 to  $500 \text{ cm}^{-1}$ .

The set-up is shown in figure 6.3. A Ti:Sapphire amplified laser system (Coherent MICRA master oscillator, Coherent LEGEND ELITE regenerative amplifier) produces 35 fs laser pulses at 800 nm, 3.5 mJ energy and 1 kHz repetition rate. The beam is splitted into pump for THz generation and probe for ABCD detection by a variable attenuator. By using it no energy losses are present, since power is variably distributed between the two arms. The pump beam is delivered through a  $\beta$ -BBO crystal in order to have second-harmonic generation (SHG) producing 400 nm pulse train which is perfectly collinear with the fundamental harmonic one. The correctly phase match between the two pulse-trains is achieved by adjusting the position of the crystal. Since the 400 nm beam is orthogonally polarized with respect to 800 nm one, a half-wave plate is placed after the  $\beta$  barium borate (BBO) crystal to rotate of  $90^\circ$  the polarization of the SH wave leaving unchanged that of the fundamental wave[2][3]. Both the waves are focalized in air to create a plasma filament which acts as THz source.

THz generation in plasma via two-colors photoionization can be roughly considered a Four-Wave Mixing (FWM) process[4]

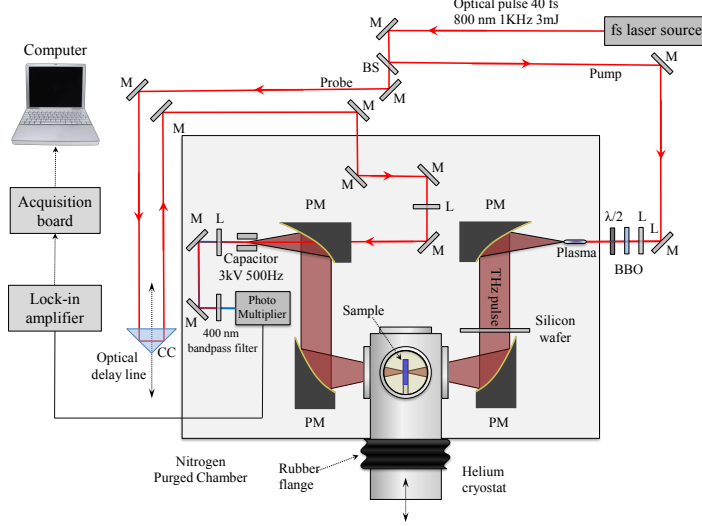


**Figure 6.3:** Experimental setup of THz-TDS based on plasma generation of THz radiation and ABCD. M: mirror, BS: beam-splitter, CC: corner cube, L: lens, PM: parabolic mirror, PcA: photoconductive antenna.

$$E_{THz} = \chi_{plasma}^{(3)} E_{\omega}^2 E_{2\omega} \quad (6.2)$$

in which the  $\chi_{plasma}^{(3)}$  is the third-order susceptibility of the gas plasma. However, this FWM-based interpretation does not take into account the origin of the  $\chi_{plasma}^{(3)}$ , which can be originated either from the free electron in plasma or from the bound electrons in ionized molecules[2][5][6].

The radiation generated by the plasma is collected and collimated by a PM and sent through a silicon wafer to remove the high-frequency components of radiation i.e. visible and UV light. The THz radiation is then focused on the sample by another PM and the transmitted component is collected and re-focused on the ABCD detector by a second couple of PMs. The ABCD detection is based on the principle of THz electric field induced second harmonic generation (TFI-SHG) in air[7][6]. Since air, as well as other gases, possesses a non-zero third-order susceptibility  $\chi_{air}^{(3)}$  it is possible to induce SHG through the Four-Wave Mixing process

$$E_{2\omega}^{THz} = \chi_{air}^{(3)} E_{\omega}^2 E_{THz} \quad (6.3)$$

The ABCD is essentially a heterodyne detection since a modulated 500 Hz DC electric field is applied at the focus of both THz and 800 nm radiations. The DC-bias-field-induced second harmonic acts as local oscillator for the coherent

### 6.3. Extraction of optical parameters from the measurements

detection of the TFI-SHG as reported below[8].

$$E_{2\omega}^{DC} = \chi_{air}^{(3)} E_{\omega}^2 E_{DC} \quad (6.4)$$

$$I_{2\omega} = (E_{2\omega}^{THz} + E_{2\omega}^{DC})^2 = I_{2\omega}^{THz} + I_{2\omega}^{DC} + 2 E_{2\omega}^{THz} E_{2\omega}^{DC} \quad (6.5)$$

By using a lock-in amplifier the heterodyne term is measured.

The ABCD detector is custom built and its core is represented by two electrodes placed at the focal point of fundamental and THz radiation, biased by a DC high-voltage power supply (3 kV). Between them the FWM processes take place and the resulting 400 nm wave is collimated by a lens, goes through a band-pass filter which completely removes the 800 nm radiation, and reaches the photomultiplier. The signal is amplified by the lock-in amplifier and detected by a digital acquisition system. The whole THz path, included the plasma filament, is placed inside a nitrogen-purged chamber to remove the water absorption.

## 6.3 Extraction of optical parameters from the measurements

The optical properties of the material under investigation can be obtained by measuring the variation in amplitude and phase that the THz pulse experiences by passing through the sample. The extraction of the optical parameters such as the refractive index,  $n_s$ , and the absorption coefficient,  $\alpha_s$ , can be achieved through the measurement of the *transfer function* of the material,  $H(\omega)$ , which is defined as the ratio between the Fourier transformed electric field of the transmitted pulse,  $E_t(\omega)$ , and the reference one,  $E_i(\omega)$ . In case the sample is made by a homogeneous material, the THz field hits orthogonally the sample's surface[9] and it is referenced with respect to an empty path, the transfer function reads as follow

$$H(\omega) = \frac{E_t(\omega)}{E_i(\omega)} = \tau\tau' FP(\omega) e^{-i[\hat{n}_s(\omega) - n_0] \frac{\omega d}{c}} \quad (6.6)$$

$$\tau = \frac{2n_0}{n_0 + \hat{n}_s} \quad \tau' = \frac{2\hat{n}_s}{n_0 + \hat{n}_s} \quad \rho' = \frac{n_0 - \hat{n}_s}{n_0 + \hat{n}_s} \quad (6.7)$$

where  $\hat{n}_s$  is the complex refractive index of the material,  $d$  its thickness and  $FP(\omega)$  is the Fabry-Pérot effect due to the multiple reflections inside the sample and can be written as

$$FP(\omega) = \sum_{m=0}^{\infty} \left[ \rho' e^{-2i \hat{n}_s(\omega) \frac{\omega d}{c}} \right]^m \quad (6.8)$$

$\tau$  is the nitrogen-sample transmission coefficient and  $\tau'$ ,  $\rho'$  are the sample-nitrogen transmission and reflection coefficient, respectively. The complex refractive index is defined as  $\hat{n}_s(\omega) = n_s(\omega) - ik(\omega)$ , in which  $n_s(\omega)$  is the refractive index of the sample and  $k(\omega)$  its extinction coefficient. In the THz-TDS experiment in transmission configuration, the optical properties of the material, such as  $n_s(\omega)$ , the absorption coefficient,  $\alpha_s(\omega) = 2\omega k_s(\omega)/c$  as well as the sample thickness,  $d_s$ , are extracted from the experimental transfer function,  $H_{exp}(\omega)$ , through the equations (6.6) and (6.8). Unfortunately, equation (6.6) cannot be analytically solved and, moreover, it is not generally possible measuring the sample's thickness with enough precision, for this reason an iterative procedure is usually applied to obtain the material's optical parameters[10][11][12]. Such procedure is based on the numerical algorithm proposed by Scheller at all[13].

**Step 1.** The first step consists in evaluating both  $n_s$  and  $\alpha_s$  neglecting the Fabry-Pérot term and the imaginary part of  $n_s$  in the Fresnel coefficients (6.7). By this approximation, the analytical solution of  $n_s(\omega)$  and  $\alpha(\omega)$  can be achieved as

$$n_s(\omega) = n_0 - \frac{c}{\omega d} \arg [H(\omega)] \quad (6.9)$$

$$k_s(\omega) = \frac{c}{\omega d} \left\{ \ln \left[ \frac{4 n_0 n_s}{H(\omega)(n_0 + n_s)^2} \right] \right\} \quad (6.10)$$

where  $\arg(z)$  is the argument of a complex number<sup>1</sup>.

By substituting  $H$  with  $H_{exp}$  and measuring the thickness of the sample by means of a micrometer screw gauge,  $n_s(\omega)$  and  $\alpha_s(\omega)$  can be computed, even if they suffer of periodical oscillations due to the omission of the Fabry-Pérot term. If the FP reflections are clearly distinguishable in the time-domain signal, the transfer function can be evaluated just cutting them out and analysing only the signal portion related to the sample. By it, the correct optical parameters are easily recovered. In the case that the reflections are partially superimposed with the sample signal, or if the time evolution of the sample's signal is long-lasting, the above mentioned procedure cannot be applied. The FP oscillations

<sup>1</sup> A complex number  $z = a + ib$  can be expressed in polar coordinates as follow:

$$\begin{cases} a = \rho \cos \theta \\ b = \rho \sin \theta \end{cases}$$

$\theta$  is the argument of the complex number and represents the angle from the positive real axis to the vector representing  $z$ , while  $\rho = |z|$  is the modulus of such vector, from the geometrically point of view.



### 6.3. Extraction of optical parameters from the measurements

suppression is achieved by using a polynomial fitting of the optical parameters, retracing the frequency dependence of  $n_s$  and  $\alpha_s$ . After a preliminary estimation of  $n_s$ ,  $\alpha_s$  and  $d_s$ , the transfer function is easily obtained from (6.6) and (6.8), in which the sum runs over the number of internal reflections.

**Step 2.** The numerical optimization of the optical parameters at some fixed thickness values is attained through the minimization of the difference between the theoretical and the experimental transfer function,  $H(\omega)$  and  $H_{exp}(\omega)$  respectively, at each frequency.

$$\Delta H(\omega) = \sum_{\omega} |H(\omega) - H_{exp}(\omega)| \quad (6.11)$$

Such optimization exploits the Nelder-Mead algorithm, and the further parametrization of both  $n_s(\omega)$  and  $\alpha_s(\omega)$  (equation 6.12 and 6.13) to calculate their new values:

$$n_s^{new}(\omega) = \xi[n_s^{old}(\omega) - 1] + 1 \quad (6.12)$$

$$k_s^{new}(\omega) = \chi k_s^{old}(\omega) \quad (6.13)$$

where  $\xi$  and  $\chi$  are the two fitting parameters. This procedure is repeated for different values of thickness, and for each  $d$ , new values of  $n_s(\omega, d)$  and  $\alpha_s(\omega, d)$  are obtained by means of equations (6.12) and (6.13); they are, then, filtered by the polynomial fit and, finally, they are optimized through the  $\Delta H$  function minimization. Plotting  $\Delta H$  against  $d$ , several minima are usually present. Among them, the absolute minimum corresponds to the real sample thickness,  $d_{min}$ . The entire procedure is then repeated using the obtained parameters  $n_s(\omega, d_{min})$ ,  $\alpha_s(\omega, d_{min})$  and  $d_{min}$  as input values, adding the further parametrization of the thickness,  $d' = \zeta d$ , in order to refine it locally.

**Step 3.** Finally, the optimization of the optical parameters at each frequency  $\omega_i$  is accomplished by minimizing the following expression

$$\Delta H(\omega_i) = |H(\omega_i) - H_{exp}(\omega_i)| \quad (6.14)$$

In doing it, the input values of  $n_s$  and  $\alpha_s$  are those obtained from the previous step. The minimization of  $\Delta H(\omega_i)$  exploits the same algorithm mentioned in step 2 and the parametrization of the optical parameters (equation (6.12) and (6.13)). The only difference consists into keep the  $d = d_{min}$  constant during the whole process. The frequency behavior of  $n_s$  and  $\alpha_s$  can be further refined by repeating the whole procedure for several times. This procedure is necessary in case of

samples which display short optical path. The iterative procedure is summarized in Figure 6.4. A further passage consists in the smoothing of  $n_s$  and  $\alpha_s$  by using both a polynomial fit, to well reproduce the baseline, and an appropriate number of Lorentzian functions to better reproduce the shape of the absorption bands. Clearly, the fit of  $n_s$  requires the imaginary part of the Lorentzian functions, while for  $\alpha_s$  it is required the real part. The above mentioned iterative procedure has been self-implemented in MATLAB code.

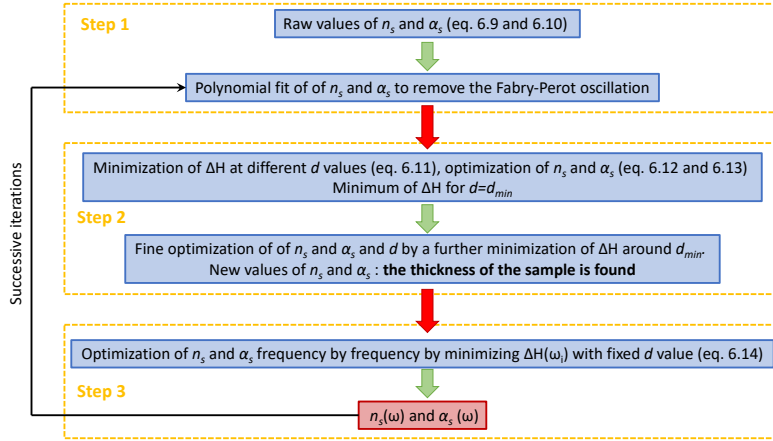


**Figure 6.4:** Schematic representation of the fitting procedure used for the extraction of the refractive index,  $n_s$ , the absorption coefficient  $\alpha_s$ , and the sample thickness  $d$ . The algorithm can be diagrammed in three main blocks. *Step 1*: a preliminary and approximated evaluation of the refractive index and absorption coefficient. *Step 2*: a minimization routine of the function  $\Delta H$  enables the estimation of the correct value of the sample thickness and more reliable values of  $n_s$  and  $\alpha_s$ . *Step 3*: the real frequency dependence of the optical parameters is revealed through the minimization of  $\Delta H$  frequency by frequency. For very thin samples, successive iterations of the process need to be repeated several times as long as the sample thickness has not been stabilized. In each cycle the output parameters of the step 3 are smoothed out by the polynomial fit and used as input parameters again for the step 1.

## 6.4 The THz spectrum

A typical THz spectrum is reported in Figure 6.5(b) and 6.6(b). The available spectral window, in other words the frequency range in which the Fourier Transform of the signal is not very noisy and significantly different from zero at the same time, is strongly connected to the absorption through the so called *Dynamic Range*,  $DR$ . The definition of such quantity is reported in equation (6.15), and can be summarised as the ratio between the maximum signal and the smallest measurable one. It describes the maximum variation of the signal that can be measured.

$$DR = \frac{E_{max}}{N_{rms}} \quad (6.15)$$

In the equation (6.15),  $E_{max}$  is the maximum signal amplitude and  $N_{rms}$  is the root mean square of the noise floor. The Dynamic Range critically depends on the frequency, and it usually decreases at high frequency. In case of transmission configuration, the maximum absorption value,  $\alpha_{max}$ , is limited by the  $DR$  through the following relation[9]

$$\alpha_{max} l = 2 \ln \left[ DR \frac{4n_s}{(n_s + 1)^2} \right] \quad (6.16)$$

where  $l$  and  $n_s$  are the sample's thickness and refractive index, respectively. Since the Dynamic Range of a THz-TDS spectrum decreases with frequency, while the sample absorption typically increases, equation 6.16 sets a limit on the effective measurement bandwidth of optical parameters. At the point where  $\alpha = \alpha_{max}$ , the data becomes very noisy and decreases in line with the  $\alpha_{max}$  curve.

The main difference between the THz-TDS setup based on PcA and that based on plasma and ABCD is the available spectral window. Indeed, the former has a spectral window from 0.2 to 3.5 THz (ca. from 7 to 115  $\text{cm}^{-1}$ ) (Figure 6.5(b)) whereas the latter from 0.5 to 15 THz (ca. from 15 to 500  $\text{cm}^{-1}$ ) (Figure 6.6(b)).

CHAPTER 6. Time Domain THz Spectroscopy

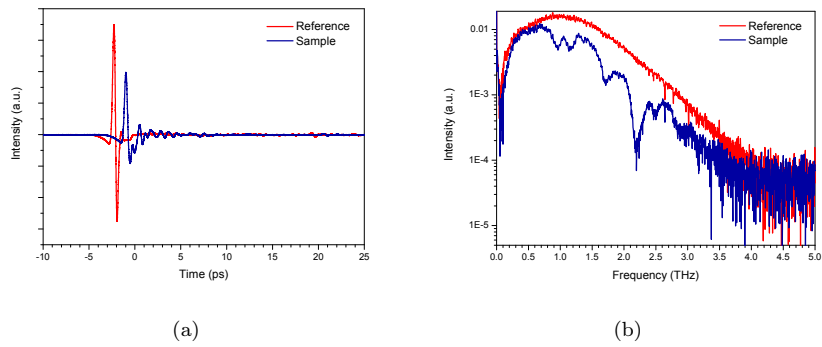


**Figure 6.5:** (a) Time domain signal recorded by the set up based on PcA. (b) Frequency domain signal after a Fourier Transform process. The red solid line is related to the reference while the blue solid one to the sample.

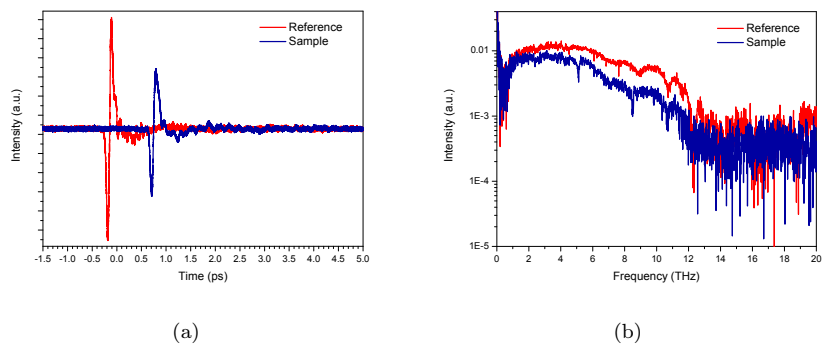


**Figure 6.6:** (a) Time domain signal recorded by the set up based on plasma generation and ABCD. (b) Frequency domain signal after a Fourier Transform process. The red solid line is related to the reference while the blue solid one to the sample.

## 6.5 Investigation of water absorption coefficient in FIR

The THz-TDS setup described in section 6.2 has been tested on liquid water, a well-known sample which deserves a place on the podium of the most studied materials in the history. Although it is the most abundant liquid on Earth and it represents the most important ingredient of life, it is one of the less understood liquid at molecular level, even if  $\text{H}_2\text{O}$  is a particularly simple and stable molecule. It displays many peculiar properties that are mainly related to its ability to establish numerous hydrogen bonds.

Despite IR spectroscopy represents one of the most powerful tools in the investigation of hydrogen bonds, several problems arise in case of water. Indeed,  $\text{H}_2\text{O}$  shows dramatically strong absorption coefficient  $\alpha$  that makes usual experimental absorption setups hard to use. Generally, attenuated total-reflection (ATR) setups are preferred[14] since they allow to overcome such an issue. However, the capability to measure the FIR absorption spectrum of liquid water in transmission configuration represents a great advantage as first step in the implementation of mid-IR-pump THz-probe time-resolved spectroscopy. This experiment should allow the study of the water molecules dynamics after a strong excitation of the O–H stretching with a IR pump pulse (central frequency ca.  $3000\text{ cm}^{-1}$ ). In this framework, it was decided to use a custom cell composed by two diamond windows and a Indium metal spacer with thickness of ca.  $20\text{ }\mu\text{m}$ . Such a cell is placed in a copper holder (Figure 6.7) which is screwed on the cryostat cold finger in order to acquire liquid water spectra in a temperature range from  $-18$  to  $87^\circ\text{C}$ . The extraction of the absorption coefficient  $\alpha(\omega)$  and the refractive index  $n(\omega)$  follows an iterative procedure that is slightly different from that discussed in section 6.3. Indeed, firstly the optical parameters of the diamond windows have been recovered and secondly the water-loaded cell has been measured. The water optical parameters has been obtained considering the sample constituted by three layers: first diamond window, water and second diamond window[15].

The resulting FIR absorption spectra (Figure 6.8(a)) show a well-defined band at  $200\text{ cm}^{-1}$  for supercooled water which progressively becomes smoother increasing the temperature[16], also the absorption coefficient at  $300\text{ K}$  and  $33\text{ cm}^{-1}$ , i.e.  $1\text{ THz}$ , is ca.  $220\text{ cm}^{-1}$ [17] and slightly increases at higher temperature. The refractive index (Figure 6.8(b)) shows a progressively smooth of the knee by raising up the temperature[18][19]. Such outcomes are consistent with what previously reported in literature, confirming the potentiality of the setup. It is worth noting that reaching these results in transmission configuration is not trivial, especially considering the high signal to noise ratio achieved. On this

basis, the implementation of the mid-IR-pump THz-probe experiment has been planned and it is currently under development.

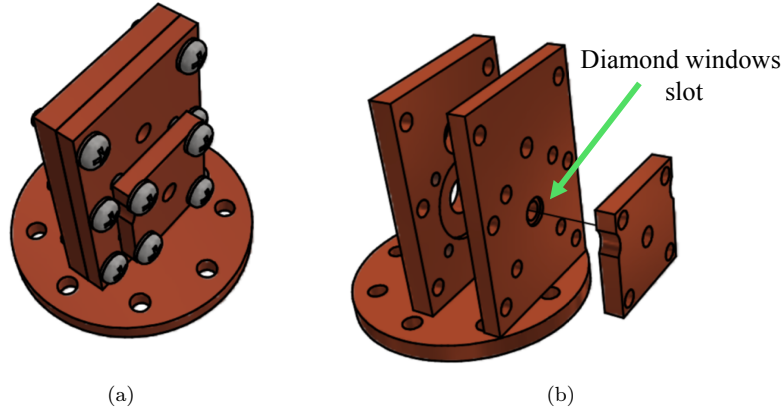


**Figure 6.7:** (a) Closed and (b) opened diamond cell holder. The green arrow indicates where the diamond cell, composed by two diamond windows and a Indium spacer, is placed.

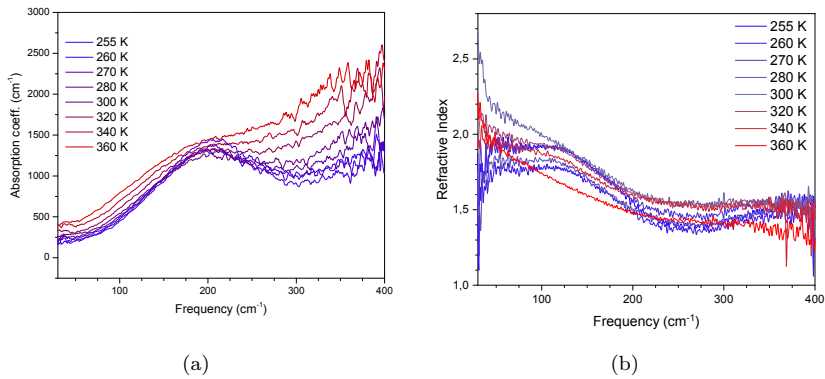


**Figure 6.8:** Experimental liquid water (a) absorption coefficient and (b) refractive index at different temperature as function of frequency. The measurements are carried out in transmission configuration on a water film of ca. 20  $\mu\text{m}$  thickness.

## Chapter 7

# Time-resolved THz-EPR spectroscopy

### 7.1 NovoFEL

The Novosibirsk Free Electron Laser (NovoFEL) facility is composed by three FELs, the electron beam of the same electron accelerator, a multi-turn energy recovery linac (ERL) (Figure 7.1). It operates in quasi-continuous (CW) mode and produces a periodic train of radiation pulses. Starting from low energy injector, electrons pass from one to four times (depending on the FEL used) through accelerating radio frequency (RF) structure. After that, they lose part of their energy in the FEL radiating system (undulator and optical resonator). The used electron beam is decelerated in the same RF structure, and the low-energy electrons are absorbed in the beam dump. The radiation of all three FELs is released through opening in mirrors of the optical resonators, then it passes through the CVD-diamond windows, is directed to the radiation combiner and finally transferred through the nitrogen-filled beamline to the users stations[20].

The FEL 1 (1-st stage FEL) provides a narrow-band terahertz radiation in the wavelength range of 90-240  $\mu\text{m}$  at an average power of up to 0.5 kW and a peak power of up to 1 MW[21]. The FEL 2 (2-nd stage FEL) is based on two track ERL and works in far infrared spectral range (35–90  $\mu\text{m}$ )[22]. The FEL 3 (3-rd stage FEL) is based on four track ERL and the expected spectral range is 5–15  $\mu\text{m}$  (mid infrared)[23]. Energy recovery allows one to achieve a very high average current of the electron beam, which results in high average power of radiation (50 W for the wavelength range of 8.5–9.6  $\mu\text{m}$ )[24]. NovoFEL is capable of producing up to 1 MW peak power in THz range, and owing to its recuperation scheme it is the most powerful source of THz coherent radiation in

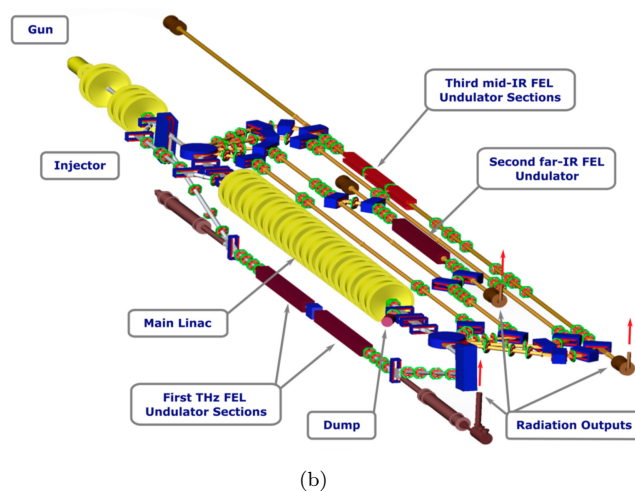
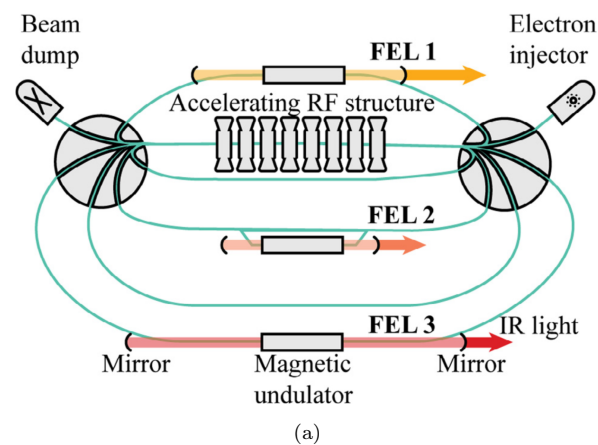


**Figure 7.1:** (a) Schematic view of the Novosibirsk Free Electron Laser (NovoFEL) facility and (b) its spatial disposition. It is based on three FELs in its multi-turn ERL structure.



the world. NovoFEL radiation consists of continuous train of ca. 10-70 ps pulses with a repetition time from 133 to 267 ns (depending on the FEL used)[24]. The radiation wavelength can be precisely tuned within the ranges mentioned above; the relative linewidth of the radiation spectrum is ca. 0.2–1%. The laser radiation is linearly polarized and completely spatially coherent. The laser beam intensity profile has a Gaussian shape[24].

In the normal operation regime (CW), the FEL provides a continuous train of short radiation pulses (50-100 ps), which follow each other with the frequency of ca. 5.6 MHz determined by the optical cavity length. When NovoFEL operates in the power modulation mode, the laser radiation consists of macropulses with minimal duration of about 10  $\mu$ s and arbitrary repetition rate. Each macropulse contains several individual THz radiation pulses and its shape depends on the FEL gain (pulse rise) and the quality factor of the optical cavity (pulse decay)[25].

For the case of FELs based on linear accelerators and thus operating in pulsed mode[26], the FEL lasing can be controlled by the electron beam injection process.

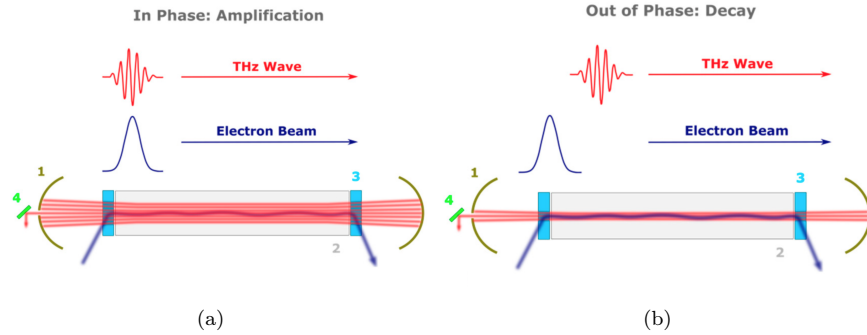


**Figure 7.2:** Schematic representation of THz radiation amplification (a) or suppression (b). The latter is achieved by periodic shift of the phase of the electron bunch injection. The numbers show optical resonator (1), undulator (2), dipole magnets (3) and THz radiation output (4).

In the normal operation mode (CW mode), THz radiation and electron bunches in the optical resonator are required to come to the undulator simultaneously. In that case, stimulated emission occurs, allowing for the amplification of THz radiation. Thus, THz light amplification in the FEL oscillator takes place only when the electron bunch repetition rate is equal to the round-trip frequency of the optical cavity and the electron bunch and optical wave propagate in-phase in the optical cavity (Figure 7.2(a)). When NovoFEL operates in the power modulation mode, THz light amplification should be suppressed in the time between THz macropulses, and this can be done by the suppression of the stimulated emission process. Thus, THz light suppression in the FEL oscillator can be achieved

when the electron bunch repetition rate is still equal to the round-trip frequency of the optical cavity, but the electron bunch is phase-shifted respect to the optical wave in the optical cavity (Figure 7.2(b)). The latter is achieved when the injection phase of the electron bunch is shifted by one or more periods of the radio frequency RF accelerating field, which does not almost influence on beam dynamics in the accelerator[25]. To prevent the formation of a new THz wave, this injection phase shift has to be done periodically.

## 7.2 EPR spectrometer

X-band (ca. 9 GHz) EPR spectrometer combined with NovoFEL is based on modified commercial X-band microwave (MW) bridge ER 046MRPTW (Bruker, Germany). MW frequency was controlled by the Agilent 53131A-124 (Agilent, USA) frequency counter. The EPR spectrometer is equipped with a helium cryostat (Cryotrade Engineering, Moscow, Russia) and LakeShore 335 temperature controller (Lake Shore Cryotronics, Westerville, OH, USA) which allows to perform the EPR experiments in the temperature range of 4–300 K. ER 4118X-MD5 resonator (Bruker, Germany) was used, but the dielectric sapphire insert was replaced by the bismuth germanate (BGO) one (4 mm inner diameter) to improve the quality of baseline in CW experiments[27]. Permalloy based electromagnet of 3 Ohm resistance was used to produce the magnetic field of up to 0.9 T. The power supply SPS 40A-160V (ELIP, Russia) and Hall effect field controller BH 15 (Bruker, Germany) were used to control the magnetic field. The phase-sensitive detection of the EPR signal in CW mode was done using SR830 lock-in amplifier (Stanford Research Systems, USA). The G3-112/1 amplifier was used to amplify 100 kHz modulation sine wave of the SR830 that was applied to modulation coils of the EPR resonator. The maximum available modulation amplitude was 4 G. The detection of the EPR signals locked to the repetition rate of NovoFEL micropulses (3.7–7.5 MHz) can be done with 200 MHz lock-in amplifier SR844 (Stanford Research Systems, USA). Recording of the transient signals in TR mode was performed simultaneously with two Keysight DSOX2012A oscilloscopes (Keysight Technologies, USA) in order to acquire two different sampling scales, e.g. different timescales in case of TR kinetics. THz irradiation of samples inside the resonator is carried out via a specially designed waveguide, which is also used as a sample holder. fsc2 program running under GNU/Linux was used for controlling the spectrometer.

### 7.3 THz waveguide and optical setup

Optical elements used in the cryostat, namely quartz windows, and EPR resonator (sapphire or BGO dielectric insert) are not transparent in certain ranges of far/mid-IR radiation. Therefore, the most straightforward way to carry the radiation directly to the sample in the EPR resonator is to use a sample holder which also plays a role of hollow waveguide for THz radiation. Instead of standard sample holder (a rod of ca. 60 cm length and 8 mm in diameter), a glass tube of the same outer diameter and similar length is used. The inner diameter of the tube is 5 mm. The sample access size of the EPR dielectric resonator is limited by the inner diameter of corresponding dielectric insert: 5 mm for standard sapphire insert and 4 mm for BGO insert used in this work. To fit to this size, the glass tube has a narrowing to 3.6 mm (outer diameter) at one of its ends. Tollens' reagent was used to apply a silver mirror at the inner surface of the tube making it reflective for NovoFEL radiation. The only part of inner surface of the tube which was free of the silver mirror is the narrowed end of the tube positioned in the EPR resonator (Figure 7.3(a)). Relatively low transmission coefficient of the waveguide[24] is mainly caused by conversion losses of the Gaussian beam to main waveguide modes and reflection of the light at the narrowed end of the waveguide. Polarization preservation coefficient of the waveguide is quite high and therefore polarization-sensitive experiments can be performed[24]. The size of the THz beam coming out of the nitrogen-filled beamline of NovoFEL was adjusted to the cross section of THz waveguide using optical system (Figure 7.3(b)) of two 90° off-axis parabolic mirrors. The mirrors compress the THz beam by a factor of ca. 15. Optical system is equipped with mechanical shutter and diaphragms to attenuate the incident radiation; it also has THz power probe and tuning mechanism to align the THz beam and waveguide.

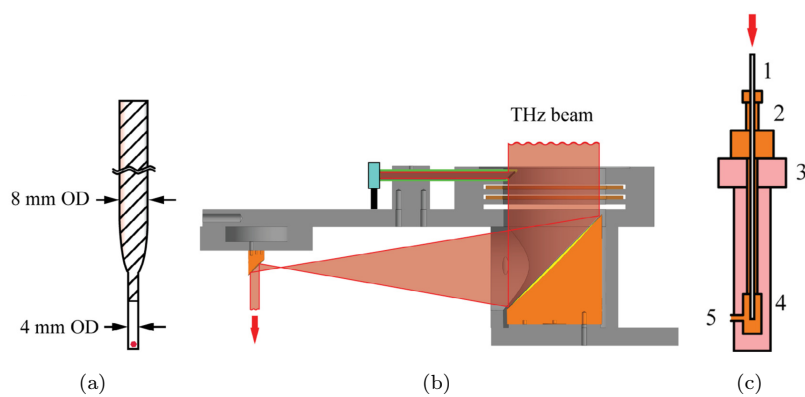


**Figure 7.3:** (a) Sketch of the sample holder used for THz irradiation. Grid lines show silver mirror coating, red circle illustrates the sample. (b) Optical system based on two  $90^\circ$  off-axis parabolic mirrors. THz beam path (red), parabolic mirrors (yellow), THz power probe (green) and power meter (cyan) are shown. (c) Irradiation scheme of the experiment. All parts of the EPR spectrometer except for cryostat and resonator are omitted. (1) sample holder, (2) EPR probehead, (3) EPR cryostat, (4) sample inside the EPR resonator, (5) optical window of the cryostat.

## Chapter 8

# Sample preparation

### 8.1 THz-TDS measurements

All the compounds investigated by THz-TD spectroscopy were microcrystalline powder. The most convenient way to perform the experiment is managing the sample as pellet. This, indeed, allows to adjust the concentration of the investigated compound, according to its absorption coefficient, by dispersing it in high-density polyethylene (HDPE) powder. The latter is also necessary to reduce the pellet's fragility, allowing its easier manipulation. Samples measured by PcA-based THz-TDS have been prepared with HDPE provided by Sigma-Aldrich, CAS Number 9002-88-4, while those investigated by the other setup have been prepared with HDPE provided by Micro Powders, Inc., MPP-620XXF. The mixture of sample's microcrystals and HDPE (ca. 70 mg) were pressed under a manual hydraulic press (ca. 0.8 GPa) to prepare the pellet (13.2 mm diameter, 0.7 mm thickness, ca. 70 mg weight).

### 8.2 TR-THz-EPR measurements

The sample measured in TR-THz-EPR experiment is a small (ca. 2 mm diameter, 0.5 mm thickness) pellet of **VOTPP 2%**. It is prepared by pressing under a manual hydraulic press (ca. 0.8 GPa) about 20 mg of **VOTPP 2%** microcrystals. The sample is then placed at the bottom of the sample holder (THz waveguide) which is covered with polyethylene film cap transparent for THz radiation. Then the waveguide with the sample is inserted into the EPR resonator (Figure 7.3(c)). The THz power is measured at the output of THz power probe by Gentec-EO UP19K-15S-VR detector preliminary calibrated for THz frequencies used in experiments.

## References

- [1] Claudia Brückner, Gunther Notni, and Andreas Tünnermann. “Optimal arrangement of 90 off-axis parabolic mirrors in THz setups”. In: *Optik* 121.1 (2010), pp. 113–119.
- [2] Ki-Yong Kim et al. “High-power broadband terahertz generation via two-color photoionization in gases”. In: *IEEE Journal of Quantum Electronics* 48.6 (2012), pp. 797–805.
- [3] Markus Kress et al. “Terahertz-pulse generation by photoionization of air with laser pulses composed of both fundamental and second-harmonic waves”. In: *Optics letters* 29.10 (2004), pp. 1120–1122.
- [4] DJ Cook and RM Hochstrasser. “Intense terahertz pulses by four-wave rectification in air”. In: *Optics letters* 25.16 (2000), pp. 1210–1212.
- [5] Joseph Penano et al. “Terahertz generation in plasmas using two-color laser pulses”. In: *Physical Review E* 81.2 (2010), p. 026407.
- [6] L Bergé et al. “Terahertz spectroscopy from air plasmas created by two-color femtosecond laser pulses: The ALTESSE project”. In: *EPL (Europhysics Letters)* 126.2 (2019), p. 24001.
- [7] Jianming Dai, Jingle Liu, and Xi-Cheng Zhang. “Terahertz wave air photonics: terahertz wave generation and detection with laser-induced gas plasma”. In: *IEEE Journal of selected topics in Quantum Electronics* 17.1 (2010), pp. 183–190.
- [8] Benjamin Clough, Jianming Dai, and Xi-Cheng Zhang. “Laser air photonics: beyond the terahertz gap”. In: *Materials Today* 15.1-2 (2012), pp. 50–58.
- [9] Withawat Withayachumnankul and Mira Naftaly. “Fundamentals of measurement in terahertz time-domain spectroscopy”. In: *Journal of Infrared, Millimeter, and Terahertz Waves* 35.8 (2014), pp. 610–637.
- [10] Timothy D Dorney, Richard G Baraniuk, and Daniel M Mittleman. “Material parameter estimation with terahertz time-domain spectroscopy”. In: *JOSA A* 18.7 (2001), pp. 1562–1571.
- [11] Ioachim Pupeza, Rafal Wilk, and Martin Koch. “Highly accurate optical material parameter determination with THz time-domain spectroscopy”. In: *Optics express* 15.7 (2007), pp. 4335–4350.
- [12] Maik Scheller. “Real-time terahertz material characterization by numerical three-dimensional optimization”. In: *Optics express* 19.11 (2011), pp. 10647–10655.

## REFERENCES

- [13] Maik Scheller and Martin Koch. “Fast and accurate thickness determination of unknown materials using terahertz time domain spectroscopy”. In: *Journal of Infrared, Millimeter, and Terahertz Waves* 30.7 (2009), p. 762.
- [14] John E Bertie and Hans H Eysel. “Infrared intensities of liquids I: Determination of infrared optical and dielectric constants by FT-IR using the CIRCLE ATR cell”. In: *Applied spectroscopy* 39.3 (1985), pp. 392–401.
- [15] Andrea Taschin et al. “THz time-domain spectroscopic investigations of thin films”. In: *Measurement* 118 (2018), pp. 282–288.
- [16] Yves Maréchal. “The molecular structure of liquid water delivered by absorption spectroscopy in the whole IR region completed with thermodynamics data”. In: *Journal of Molecular Structure* 1004.1-3 (2011), pp. 146–155.
- [17] Jing Xu, Kevin W Plaxco, and S James Allen. “Absorption spectra of liquid water and aqueous buffers between 0.3 and 3.72 THz”. In: *The Journal of chemical physics* 124.3 (2006), p. 036101.
- [18] JK Vij, DRJ Simpson, and OE Panarina. “Far infrared spectroscopy of water at different temperatures: GHz to THz dielectric spectroscopy of water”. In: *Journal of Molecular Liquids* 112.3 (2004), pp. 125–135.
- [19] Jun Zhou et al. “Temperature dependent optical and dielectric properties of liquid water studied by terahertz time-domain spectroscopy”. In: *AIP Advances* 9.3 (2019), p. 035346.
- [20] Boris A Knyazev et al. “Novosibirsk free electron laser as a user facility”. In: *Physics Procedia* 84 (2016), pp. 27–34.
- [21] EA Antokhin et al. “First lasing at the high-power free electron laser at Siberian center for photochemistry research”. In: *Nuclear Instruments and Methods in Physics Research Section A: Accelerators, Spectrometers, Detectors and Associated Equipment* 528.1-2 (2004), pp. 15–18.
- [22] Gennady N Kulipanov et al. “Novosibirsk free electron laser—facility description and recent experiments”. In: *IEEE transactions on terahertz science and technology* 5.5 (2015), pp. 798–809.
- [23] OA Shevchenko et al. “The Novosibirsk Free Electron Laser—unique source of terahertz and infrared coherent radiation”. In: *Physics Procedia* 84 (2016), pp. 13–18.
- [24] Sergey L Veber et al. “X-band EPR setup with THz light excitation of Novosibirsk Free Electron Laser: Goals, means, useful extras”. In: *Journal of Magnetic Resonance* 288 (2018), pp. 11–22.

CHAPTER 8. *Sample preparation*

- [25] Oleg A Shevchenko et al. “Electronic modulation of THz radiation at NovoFEL: Technical aspects and possible applications”. In: *Materials* 12.19 (2019), p. 3063.
- [26] A Marinelli et al. “High-intensity double-pulse X-ray free-electron laser”. In: *Nature communications* 6.1 (2015), pp. 1–6.
- [27] Mikhail Y Ivanov et al. “Bismuth germanate as a perspective material for dielectric resonators in EPR spectroscopy”. In: *Journal of Magnetic Resonance* 271 (2016), pp. 83–89.



## Part IV

# Results and discussion



In this part, the work done during the three years of PhD will be exhaustively discussed. In the first chapter, the reader will find all the information about the investigation of the properties of several potential solid-phase molecular Qubits carried out by the multi-techniques approach. Indeed, this part of the work is founded on the *in-depth* study of the spin properties as well as the crystal lattice features that are able to influence the spin dynamics. The novelty of such a procedure consists in blending two different fields, the molecular magnetism and the vibrational spectroscopy, to obtain complementary information which allow to get new insights into the spin-lattice relaxation mechanisms. The fundamental techniques required to achieve the whole characterization of the Qubit systems are the following: pulsed and continuous wave (CW) Electron Paramagnetic Spectroscopy (EPR), alternative-current (AC) susceptometry for the spin dynamics characterization and THz Time-domain spectroscopy (THz-TDS) for the phonons' structure investigation.

The second chapter is devoted to a novel experiment aimed to shed light on the spin dynamics under THz irradiation; in the 2D-THz EPR experiment, in principle, it is possible to follow the dynamics of a spin system during and after the application of a strong THz radiation. This should permit a detailed comprehension of the coupling between the spin and the phonons, as well as provide a starting point for the manipulation of the spin through coherent THz radiations.

The studies described in the former part have been carried out in collaboration with the Laboratory of Molecular Magnetism (LAMM), led by professor Roberta Sessoli at the Chemistry Department of the University of Florence, that realized the magnetic characterization as well as the synthesis of the compounds. The *ab initio* calculations have been performed by Andrea Albino and professor Federico Totti (LAMM) together with Alessandro Lunghi of the School of Physics, AMBER and CRANN, Trinity College in Dublin. Concerning the work described in the latter part, it has been carried out during two visits of one month each at the Novosibirsk free-electron laser (NovoFEL) facility and the International Tomography Center (ITC), in collaboration with professor Matvey Fedin, Sergey Veber and Anatoly Melnikov.



## Chapter 9

# THz spectroscopy as innovative probe of the molecular Qubits performance

In this chapter the whole pathway from the very beginning of the story to the actual state of the art will be discussed by following the chronological milestones which have characterized this work. In next pages the fundamental role of THz spectroscopy in the evaluation of the Qubits performances will be clarified. The following sections are devoted to discuss the results achieved during the PhD work, in particular each section concerns a specific molecular system as well as a group of similar molecules. The last section aims to summarize such results and compare them to highlight common trends or common features of the investigated molecules. The compounds studied in this chapter are vanadium(IV)-based molecules characterized by a single unpaired electron ( $S=1/2$ ) localized on the metal centre, coupled, at low magnetic field, with the  $I=7/2$  nuclear spin of the most abundant isotope  $^{51}\text{V}$ . Two groups of molecules can be individuated: those containing the vanadyl moiety and those containing tris-chelate V(IV) ions. The former ones have square pyramidal geometry whereas the latter ones have distorted octahedral geometry. The ligand field symmetry imposes a  $d$ -orbital splitting that leaves the  $d_{xy}$  orbital lowest in energy and well-isolated from the others for the penta-coordinated class of molecules while for the exacoordinated ones it leaves the  $d_{z^2}$  orbital lowest in energy.

## 9.1 The Vanadyl prototype: VO(acac)<sub>2</sub>

The Vanadyl-acetylacetonate deserves its own section since it can be considered the prototype from which this work has started on. Its formula is VO(acac)<sub>2</sub> where acac<sup>-</sup> stands for the acetylacetonate anion. It is the simplest  $\beta$ -diketonate ligand that can be used to synthesize a vanadyl-based complex, making VO(acac)<sub>2</sub> also suitable for theoretical *ab-initio* calculations. Moreover, it has interesting physical properties, such as its low sublimation temperature, thanks to which it can be easily evaporated on surfaces[1]. It also crystallizes in large crystals with dimensions up to several millimeters whereby it is possible to perform single-crystal measurements.

### 9.1.1 Molecular and crystal structure

The VO(acac)<sub>2</sub> (Figure 9.1) contains the vanadyl moiety coordinated by the oxygen atoms of the ligands, two for each acetylacetonate, resulting in a distorted square pyramidal geometry. The metal ion is slightly (0.545 Å) above the basal plane, the V=O bond distance is 1.585 Å and the V–O bond length is 1.969 Å (table 9.1). Since the V=O double bond is shorter than the four V–O single bonds and considering the out-of-plane position of the metal centre, the *d* orbitals are affected by a strong axial distortion of the ligand field which results in the *d<sub>xy</sub>* orbital lying at the lowest energy, as shown in Figure 9.2. This well isolated ground level is occupied by a single electron, giving rise to a good S=1/2 Qubit candidate. The compound crystallizes in the triclinic  $P\bar{1}$  space group with two molecules per unit cell.

Space group	Point group	V=O distance (Å)	V–O distance (Å)	V...V shortest distance (Å)
Triclinic $P\bar{1}$	$C_1$	1.585	1.969	5.61

**Table 9.1:** Main parameters of the crystal structures of VO(acac)<sub>2</sub>[1].

### 9.1.2 Magnetic properties

The magnetization dynamics of VO(acac)<sub>2</sub> has been investigated by AC susceptibility on microcrystalline powder samples[1]. The real and the imaginary part of the magnetic susceptibility,  $\chi'$  and  $\chi''$  respectively, can be fitted according to the Debye model[2]

9.1. The Vanadyl prototype:  $\text{VO}(\text{acac})_2$

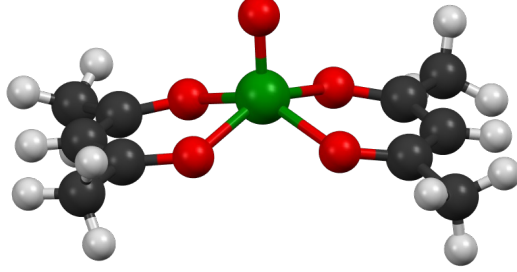


**Figure 9.1:** Molecular structure of  $\text{VO}(\text{acac})_2$ . Color code: V=green, O=red, C=black, H=white.

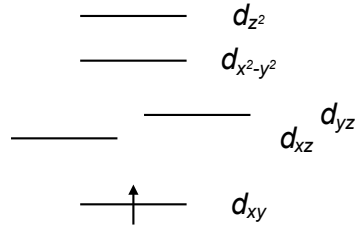


**Figure 9.2:** Ligand field-induced  $d$  orbitals splitting in  $\text{VO}(\text{acac})_2$ .

$$\chi'(\omega) = \chi_S + (\chi_T - \chi_S) \frac{1 + (\omega\tau)^{1-\alpha} \sin(\pi\alpha/2)}{1 + 2(\omega\tau)^{1-\alpha} \sin(\pi\alpha/2) + (\omega\tau)^{2-2\alpha}} \quad (9.1)$$

$$\chi''(\omega) = (\chi_T - \chi_S) \frac{(\omega\tau)^{1-\alpha} \cos(\pi\alpha/2)}{1 + 2(\omega\tau)^{1-\alpha} \sin(\pi\alpha/2) + (\omega\tau)^{2-2\alpha}}$$

where  $\tau$  is the relaxation time,  $\alpha$  represents the distribution of relaxation times,  $\chi_T$  and  $\chi_S$  are the thermal and adiabatic susceptibility, respectively. By using equations (9.1.2), it is possible to extract values of  $\tau$  as a function of the temperature or the applied magnetic field. The relaxation time measured by this technique is generally coincident with the spin-lattice relaxation time,  $T_1$ , since the spin-lattice energy transfer is generally the rate-determining step. In the case of  $\text{VO}(\text{acac})_2$  a significant spin-phonon bottleneck effect has been observed, therefore  $\tau$  does not necessary coincide with  $T_1$  anymore and it now represents the characteristic time of the phonon's energy dissipation toward the thermal bath. This case applies for samples made by crystals with dimensions larger than tens of micrometers (*Crystal* and *Grounded* in Figure 9.3).

The magnetic field dependence of the relaxation time extracted by AC susceptibility measurements (Figure 9.3 and 9.4) can be reproduced by the Brons-van Vleck model[3][4]. This model takes into account the competition between the

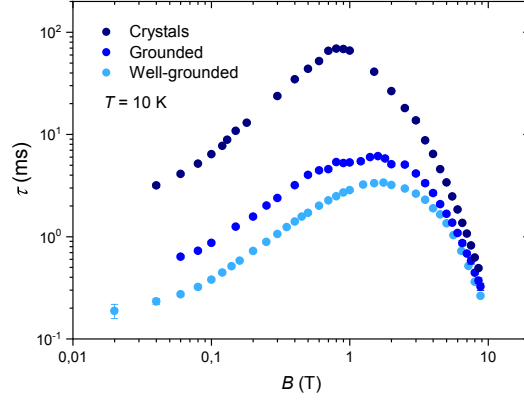


**Figure 9.3:** Magnetic field dependence of the magnetization relaxation time  $\tau$  extracted by AC susceptibility for the same sample of VOacac but with different crystallite sizes: macro-, mid-ground and well-ground crystallites.

sum of intra- and intermolecular effects, i.e. the sum of spin-spin dipolar magnetic interactions and spin-nuclei hyperfine interactions, that are predominant at low fields (ca.  $B < 1$  T), and the direct process at high fields (ca.  $B > 1$  T). The expression used for the analysis is

$$\tau^{-1} = cB^4 + d \frac{1 + eB^2}{1 + fB^2} \quad (9.2)$$

where  $c$  is the coefficient of the direct process,  $d$  is the relaxation rate at zero magnetic field,  $e$  corresponds to the ability of the external magnetic field to suppress the internal relaxation mechanisms, and  $f$  is the attitude of the internal magnetic moments of the molecule to induce relaxation.

It is worth noting that from the temperature dependence of the Brons-van Vleck  $d$  parameter it is possible to get insights into the vibrational modes involved in the spin-lattice relaxation. Indeed,  $d$  shows an Arrhenius-like temperature behavior,  $d \propto e^{U_{eff}/k_B T}$ , and the linear fit of  $\ln(d)$  vs  $1/T$  between 10 and 25 K provides an effective activation energy  $U_{eff} = 22 \text{ cm}^{-1}$ [5].

### 9.1.3 Investigation of low energy vibrations

The characterization of lattice vibrations as well as low energy molecular ones has been performed by the THz-TDS setup described in details in chapter 6. Despite VO(acac)<sub>2</sub> is a very simple molecule, the spectrum in THz regime appears crowded by several bands, as shown in Figure 9.5. Increasing the resolution as well as the possibility to get more information on the phonon's nature become



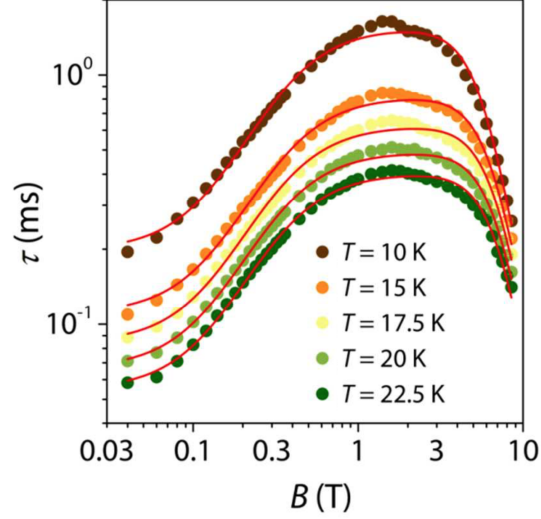


**Figure 9.4:** Field dependence of  $\tau$  extracted from AC susceptibility measurements for  $VO(acac)_2$  at different temperatures. The solid lines represent the best-fits using the Brons-van Vleck model (equation (9.2))

mandatory. In this framework, the possibility to scan the temperature from few Kelvins to room temperature can make the interpretation of the spectrum easier.

Peak label	Frequency ( $\text{cm}^{-1}$ )
<b>1</b>	43.8
<b>2</b>	71.5
<b>3</b>	76.7
<b>4</b>	92.2
<b>5</b>	115.3

**Table 9.2:** Frequency values of the five phonons at 10 K.

Many spectra have been recorded raising up the temperature from 10 to 300 K (Figure 9.6). At the lowest temperature, five peaks are easily discernible: heating up the sample, all of them become broader and some of them shift at lower energy. It is worth to note that **1** falls at  $43.8 \text{ cm}^{-1}$ , that is exactly the value predicted by considering the temperature dependence of the parameters of the Brons-van Vleck model applied to the spin relaxation rate[5]. The temperature behavior of phonons' frequency and linewidth  $\Gamma$  has been obtain by performing a curve-fitting of the spectra with the  $f(\omega)$  fit function (Equation (9.4)), which is composed by five pseudo-Voigt profiles and a polynomial base-line.

CHAPTER 9. THz spectroscopy as innovative probe of the molecular Qubits performance

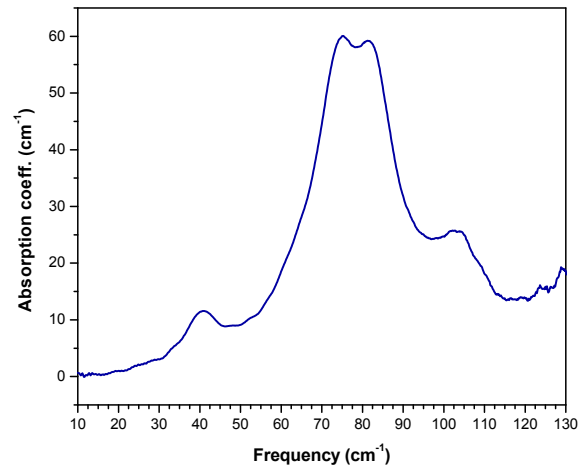


Figure 9.5: THz spectrum of VO(acac)<sub>2</sub> in the 10-130 cm<sup>-1</sup> range at room temperature.

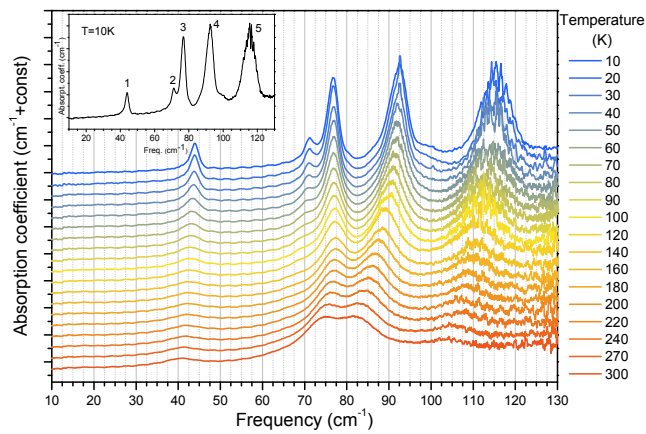
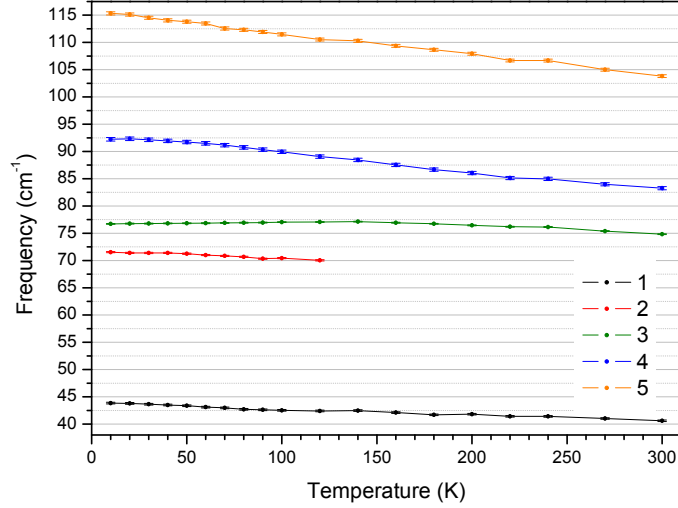


Figure 9.6: THz spectra of VO(acac)<sub>2</sub> in the 10-130 cm<sup>-1</sup> range at different temperatures. *Inset*: spectrum at 10 K in which the five absorption peaks have been labeled.



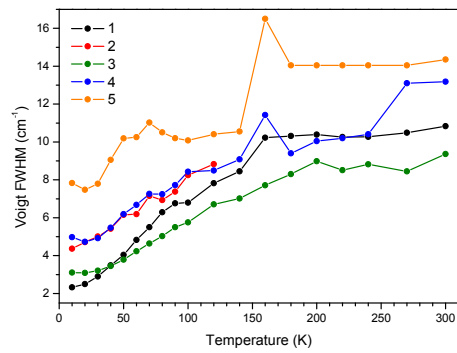
**Figure 9.7:** Temperature dependence of the five peaks' frequency. **2** disappears in the spectra at temperature above 120 K. The error bars represent the standard deviation.

$$f(\omega) = \sum_{i=1}^5 \left( \eta_i A_i \exp \left( -4 \log 2 \frac{(\omega - \omega_i)^2}{\Gamma_{G_i}^2} \right) + (1 - \eta_i) \frac{A_i}{1 + \frac{4(\omega - \omega_i)^2}{\Gamma_{L_i}^2}} \right) + BL \quad (9.3)$$

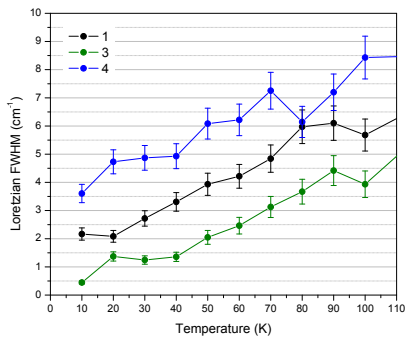
$$BL = B_0 + B_1\omega + B_2\omega^2 + B_3\omega^3 \quad (9.4)$$

In Equation 9.4,  $A_i$  is the amplitude,  $\omega_i$  is the central frequency,  $\Gamma_G$  is the gaussian line width,  $\Gamma_L$  is the Lorentzian line width and  $\eta_i$  varies between 0 and 1. The use of pseudo-Voigt profiles is required to obtain information also on the homogeneous and inhomogeneous contributions to the peaks width. The temperature trend of the phonons' frequency is shown in Figure 9.7. **2** disappears over 120 K since those on its right side get closer and become broader increasing the temperature. However, **1**, **2**, **4** and **5** show a common trend: they shift to lower energy heating up the sample. Such an attitude can be ascribed to the change in the force constant of the bonds. This is due to the anharmonic contribution of the cubic and quartic terms of the potential series expansion which take into account the thermal expansion of the material i.e. the decreasing of the density. On the contrary, **3** does not seem to be affected by the change in temperature. The error analysis, discussed in details in appendix A, leads to a standard deviation less than 1% on the peaks' position. In particular, the relative standard deviation  $\sigma\%$  associated to the determination of the frequency of each

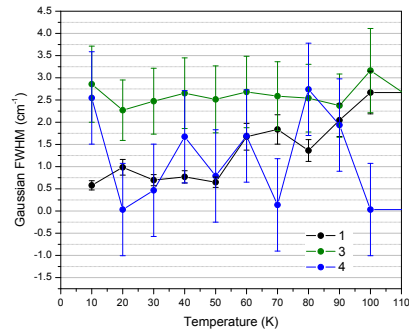
CHAPTER 9. THz spectroscopy as innovative probe of the molecular Qubits performance



(a) Voigt-linewidth



(b) Lorentzian-linewidths



(c) Gaussian-linewidths

**Figure 9.8:** Temperature behavior of the phonons' line width: (a) best-fit values of the Voigt width in the 10-300 K interval, (b) Lorentzian and (c) Gaussian contributions to the line width for 1, 3 and 4 in the 10-100 K range.

peak is listed in Table 9.3.

Peak	$\sigma\%$
<b>1</b>	0.35
<b>2</b>	0.15
<b>3</b>	0.10
<b>4</b>	0.35
<b>5</b>	0.25

**Table 9.3:** Relative standard deviation on the frequency determination of each peak.

Figure 9.8(a) shows how the linewidth of each phonon, in terms of pseudo-Voigt full width half maximum (FWHM), varies by increasing the temperature from 10 to 300 K. Also, the Lorentzian and the Gaussian contributions are recovered in Figure 9.8(b) and 9.8(c) in the 10-100 K temperature range for **1**, **3** and **4**. The Lorentzian broadening is referred to the homogeneous broadening, that is connected to the phonon-phonon interaction through the anharmonic terms of the crystal potential expansion, while the Gaussian contribution takes into account the inhomogeneous broadening. **1**, **3** and **4** show a roughly linear tendency of the homogeneous broadening and an almost stable inhomogeneous one. The relative standard deviation is of the order of 10-20% since  $\Gamma_G$  and  $\Gamma_L$  are particularly sensitive to the irregularity of the peak tails. In particular, the loss of a well definite shape of **2** above 70 K and the higher noise that affects **5** do not allow to deduce a temperature trend as clear as for the other peaks (see appendix A). It is worth noting that achieving such information is not trivial by using THz-TDS spectroscopy because it requires a very high signal to noise ratio together with long time stability of the signal.

#### 9.1.4 Simulation results

In order to shed light on the origin of the peculiar temperature behavior of phonons' frequency, an *ab initio* simulation has been performed. Such simulations were done in collaboration with Andrea Albino and Francesco Totti of the Chemistry Department of the University of Florence, and Alessandro Lunghi of the School of Physics, AMBER and CRANN, Trinity College in Dublin. The method to investigate the spin-phonon coupling is based on a perturbative approach[6]. The calculation of the spin-phonon Hamiltonian parameters was carried out with the ORCA package. As for static magnetic properties calculation, the level of theory used is DFT, with PBE0 hybrid functional. Balanced polarized triple-zeta basis set was adopted (def2-TZVP) for metal and sulfur atom, while polarized double-zeta basis set (def2-SVP) was used for light elements such as carbon and hydrogen atoms. The molecular geometry employed for these simu-

lations was obtained by the periodic DFT calculation of the optimized molecular structure in CP2K.

To accurately reproduce the THz spectrum, it is essential that the unit cell dimensions employed in normal modes calculations are chosen from the crystal structure at the temperature at which the experimental THz spectrum was obtained. It is clear in table 9.4 that a contraction occurred along the  $a$ - axis, and an expansion along the  $b$ - and  $c$ - axes. The observed volume changes between 300 K and 100 K crystal structures outlines a temperature behaviour that is confirmed by 0 K full geometry and cell optimization.

	<b>a</b> (Å)	<b>b</b> (Å)	<b>c</b> (Å)	$\alpha$	$\beta$	$\gamma$	Cell volume (Å <sup>3</sup> )
0 K	7.662	7.802	11.056	70.869	71.162	64.315	549.943
100 K	7.300	8.117	11.178	72.901	72.282	67.064	569.372
300 K	7.513	8.201	11.221	73.174	71.476	66.718	591.445

**Table 9.4:** Simulated cell parameters (0 K) and single-crystal experimental X-ray diffraction data (100 and 300 K).

It was ascertained that small changes in unit cell volumes can have a significant impact on the calculated frequencies and intensities, the resulting effect from any change in dimensions on vibrational frequencies cannot be assumed a priori. Even more, both experimental and simulation reveal a mode-specific red-shift of IR modes while increasing temperature (Figure 9.9). This aspect can be explained with the non-uniform lattice expansion along each crystallographic axis upon heating.

### 9.1.5 Conclusion

The low-temperature THz measurements allow to achieve a high-resolved spectrum (10 K) and to follow both the frequency and line width variations as function of temperature. Moreover, the frequency of the first phonon measured at 10 K, that is in the same temperature range of the AC susceptibility measurements, well correlates with that extracted from the Brons-van Vleck model by considering the relation  $U_{eff} = \hbar\omega_\alpha/2$ . The peculiar temperature behavior of the five phonons has been rationalized performing *ab initio* simulations. Indeed, the calculation clearly shows that the crystal unit cell undergoes a non-uniform expansion along each crystallographic axis upon heating.

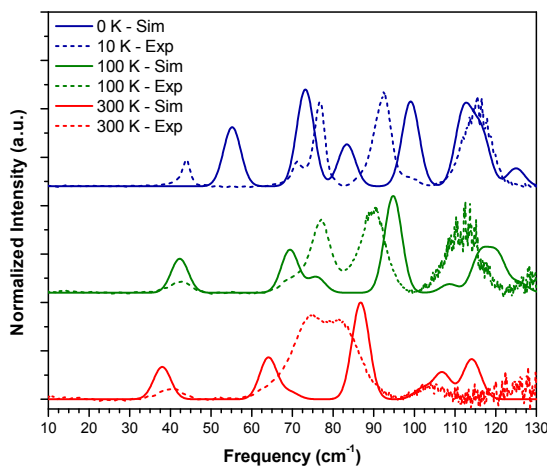


**Figure 9.9:** Simulated (solid lines) and experimental (dashed lines) spectra of  $\text{VO}(\text{acac})_2$  at 0, 100 and 300 K. The 0 K simulated spectrum is compared with the experimental reachable lowest temperature (10 K). The simulated spectra have a fixed FWHM equal to  $5 \text{ cm}^{-1}$ .

## 9.2 The role of the rigidity of the coordination shell

---

### The chapter is based on the following publication

---

“Structural effects on the spin dynamics of potential molecular qubits”. Atzori, M., Benci, S., Morra, E., Tesi, L., Chiesa, M., Torre, R., Sorace, L. and Sessoli, R. In: *Inorganic chemistry* 57(2) (2018), pp. 731-740.

---

This section is devoted to highlight the role of the coordination shell rigidity in four V(IV) complexes:

- $[(\text{Ph})_4\text{P}]_2[\text{V}(\text{cat})_3]$ ,  $[(\text{Ph})_4\text{P}]_2[\text{VO}(\text{cat})_2]$  where *cat* is catecholate and hereafter labelled **Vcat** and **VOcat** respectively;
- $[(\text{Ph})_4\text{P}]_2[\text{V}(\text{naph-cat})_3]$ ,  $[(\text{Ph})_4\text{P}]_2[\text{VO}(\text{naph-cat})_2]$  where *naph-cat* is naphthalene-catecholate and hereafter labelled **Vnaphcat** and **VOnaphcat** respectively.

More specifically, the rigidity of the coordination sphere was modified by

synthesizing tris-chelated octahedral and vanadyl square-pyramidal complexes of the same ligand, while the ligand rigidity was modified by increasing the number of condensed aromatic rings.

### 9.2.1 Molecular and crystal structures

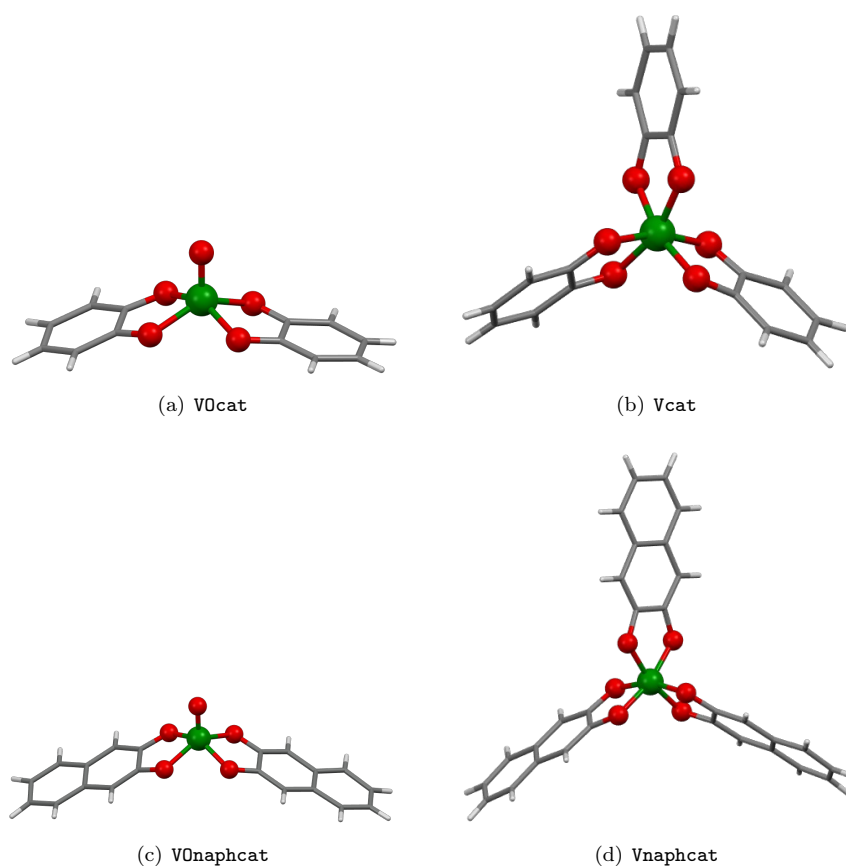


**Figure 9.10:** Molecular structure of (a) **VOcat**, (b) **Vcat**, (c) **VOnaphcat** and (d) **Vnaphcat**. Color code: V=green, O=red, C=grey, H=white.

The **VOcat** crystallizes in the monoclinic  $P2_1/c$  space group with one anionic complex and two tetraphenylphosphonium counterions in the asymmetric unit. Its crystal structure consists of symmetry-related  $[\text{VO}(\text{cat})_2]^{2-}$  anions separated by tetraphenylphosphonium counterions that preclude intermolecular contacts shorter than the sum of the van der Waals radii between metal complexes. As a result, the shortest  $\text{V}\cdots\text{V}$  distance in the crystal structure of **VOcat** is 11.95 Å. The molecular structure of the dianionic complex of **VOcat** is shown in Fig-



## 9.2. The role of the rigidity of the coordination shell

ure 9.10(a). It presents a slightly distorted square pyramidal coordination geometry due to the chelating ligand, with the metal ion slightly above the basal plane (ca. 0.62 Å) formed by the four oxygen donor atoms. The apical position is occupied by an oxo ligand, which forms a double bond with the V(IV) ion, with a resulting V=O bond distance of 1.614 Å, whereas the V–O single bond lengths in the basal plane are in the 1.960-1.980 Å range. Compound **Vcat** (Figure 9.10(b)) crystallizes in the monoclinic  $C2/c$  space group with half anionic complex and one tetraphenylphosphonium in the asymmetric unit, while compound **Vnaphcat** (Figure 9.10(d)) crystallizes in the monoclinic  $P2_1/n$  space group with one anionic complex and two tetraphenylphosphonium counterions in the asymmetric unit. The crystal structures of **Vcat** and **Vnaphcat** consist of homoleptic trischelated  $[V(\text{cat})_3]^{2-}$  or  $[V(\text{naph-cat})_3]^{2-}$  anions showing  $\Lambda$  and  $\Delta$  chirality and tetraphenylphosphonium cations. The shortest V...V distance is 10.12 Å for **Vcat** and 14.30 Å for **Vnaphcat**. The longer distance observed for the latter is clearly due to the presence of a bulkier coordinating ligand. The molecular structures of the complex anions of **Vcat** and **Vnaphcat** are reported in Figures 1b and 1c. The coordination geometry around the V(IV) ion is a trigonally distorted octahedron with an average V–O distance of 1.946 and 1.941 Å for **Vcat** and **Vnaphcat**, respectively. Because of the **VOnaphcat** (Figure 9.10(c)) tendency to slowly convert in solution in **Vnaphcat**, single crystals suitable for x-ray analysis were not obtained. Structural data were taken from the literature for the same anionic complex,  $[VO(\text{naph-cat})_2]^{2-}$ , with a different counterion, namely, trimetylenediammonium[7], provides a V=O bond length of 1.604 Å, and V–O single bond lengths in the 1.927-1.975 Å range, that well compare to those observed for **VOcat**. The above mentioned features of molecules under investigation are summarized in Table 9.5.

Molecules	Space group	Point group	V=O distance (Å)	V–O distance (Å)	V...V shortest distance (Å)
<b>Vcat</b>	monoclinic $C2/c$	$C_2$	-	1.939-1.958	10.12
<b>Vnaphcat</b>	monoclinic $P2_1/n$	$C_1$	-	1.925-1.956	11.20
<b>VOcat</b>	monoclinic $P2_1/c$	$C_1$	1.61	1.960-1.980	11.95
<b>VOnaphcat</b>	hexagonal $P6_522$	$C_2$	1.60	1.927-1.975	7.31

**Table 9.5:** Main parameters of the crystal structures for the four Vanadium(IV)-based molecules.

### 9.2.2 Magnetic properties

Continuous wave-EPR measurements on frozen solution of all the compounds have been done in order to obtain a full description of their electronic properties. It comes out that for **VOcat** and **VOnaphcat** the short V=O bond imposes a  $d$  orbital splitting of the Vanadium atom that leaves the  $d_{xy}$  orbital lowest in energy, similarly to VO(acac)<sub>2</sub>. On the contrary, for **Vcat** and **Vnaphcat** the trigonally distorted octahedral coordination geometry is responsible for a  $d$  orbital splitting that leaves the  $d_{z^2}$  orbital lowest in energy, where  $z$  is the trigonal axis of the distorted octahedron (Figure 9.11).

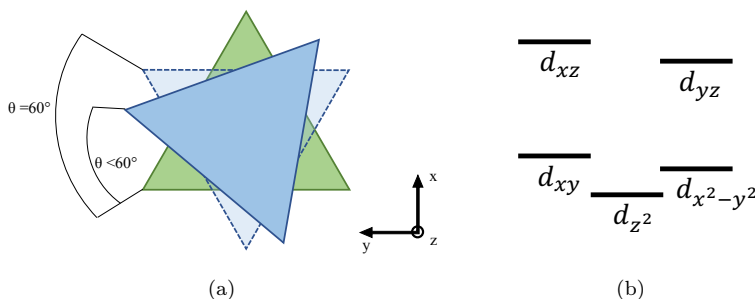


**Figure 9.11:** (a) Trigonally distorted octahedron ( $\theta < 60^\circ$ ) in which the z-axis correspond to the trigonal axis. (b)  $d$ -orbital splitting of a trigonally distorted octahedral coordination.

The spin-lattice relaxation time has been investigated by means of AC susceptibility measurements as a function of temperature and magnetic field.

It is interesting to note that the oxovanadium(IV) complexes **VOcat** and **VOnaphcat** show slow magnetic relaxation up to ca. 70-80 K with exceptionally long relaxation times (Figure 9.12). They range from ca. 10 ms at 10 K to ca. 0.040-0.060 ms at 75 K. The vanadium(IV) complexes **Vcat** and **Vnaphcat** also show slow relaxation of the magnetization, but with relaxation times that are an order of magnitude shorter than the vanadyl counterparts. More specifically, they range from ca. 4.0 ms at 5 K to ca. 0.050-0.072 ms at 30 K, above which they are not measurable. It is worth noting that the square pyramidal oxovanadium-(IV) complexes **VOcat** and **VOnaphcat** show similar absolute values of the relaxation times and similar temperature dependence independently from the structural modification introduced by the different ligand. Analogous consideration holds for the octahedral complexes **Vcat** and **Vnaphcat**. This confirms previous observations on the role played by the different orbital contribution to the ground state in determining the enhancement of the absolute values of  $\tau$  when passing from the square pyramidal to the octahedral coordination[8]. In order to get better insights on the relaxation mechanisms involved in

## 9.2. The role of the rigidity of the coordination shell

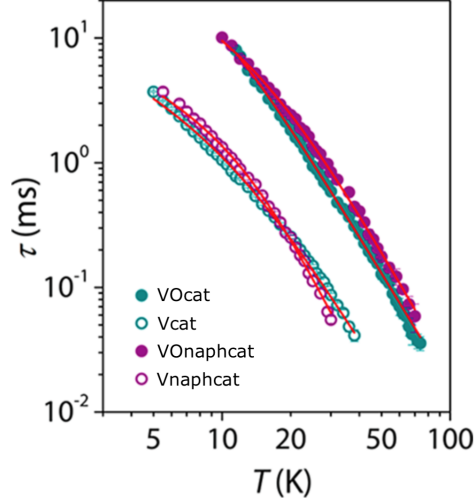


**Figure 9.12:** Temperature dependence of  $\tau$  extracted from AC susceptibility measurements for microcrystalline powders of the investigated compounds.

such compounds, the relaxation time was also investigated as a function of the static magnetic field in a wide field range (0.0-8.5 T) at different temperatures. The relaxation times extracted with the Debye model[2] for the compounds are reported in Figure 9.13.

The field dependence of the relaxation time  $\tau$  shows a nonmonotonous behavior with an extended plateau whose width is slightly reduced passing from **VOcat** to **VOnaphcat**, while it is strongly reduced when passing to **Vcat** and **Vnaphcat**, both showing very similar behaviors. The B dependence of  $\tau$  for the two vanadyl-based compounds herein investigated is well reproduced through the Brons-van Vleck phenomenological model[3][4] (see (9.2)) as in the case of VO(acac)<sub>2</sub>, whereas the vanadium(IV) compounds require an extended Brons-van Vleck law[5], as reported in equation (9.5), to provide an adequate fit of the experimental data suggesting a more-complex relaxation process.

$$\tau^{-1} = cB^4 + d \left( \frac{1 + eB^2}{1 + fB^2} \right) + g \left( \frac{1 + eB^2}{1 + hB^2} \right) \quad (9.5)$$

Interestingly, a complex behavior of the magnetic field dependence of  $\tau$  has been found to be accompanied by the presence of more than one predominant low-energy vibration[5], suggesting a correlation between the observed activation energy and the frequency ( $\omega_\alpha$ ) of the involved phonon of the type  $U_{eff} = \hbar\omega_\alpha/2$ . The same relation has been theoretically proposed for the relaxation time of SMMs characterized by excited magnetic states at high energy, when the anharmonicity, or finite line width, of vibrational modes is taken into account[9]. The

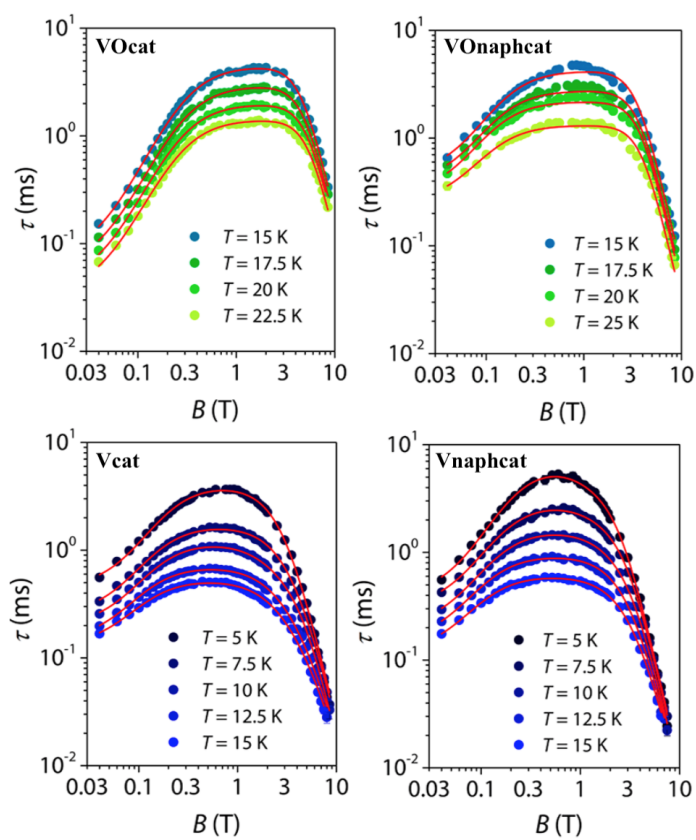


**Figure 9.13:** Magnetic field dependence of  $\tau$  extracted from AC susceptibility measurements for the investigated compounds at different temperatures. Solid lines are the best-fits of the models.

## 9.2. The role of the rigidity of the coordination shell

analysis of the temperature dependence of the  $d$  and  $g$  parameters extracted by the field dependence measurements performed at various temperatures provides a unique value of  $U_{eff}$  for **VOcat** and for **VOnaphcat**. On the other hand, the linear fit of  $\ln(d)$  and  $\ln(g)$  vs  $T^{-1}$  provides a double value of  $U_{eff}$  for **Vcat** and **Vnaphcat** (Figure 9.14). The extracted values are reported in Table 9.6.

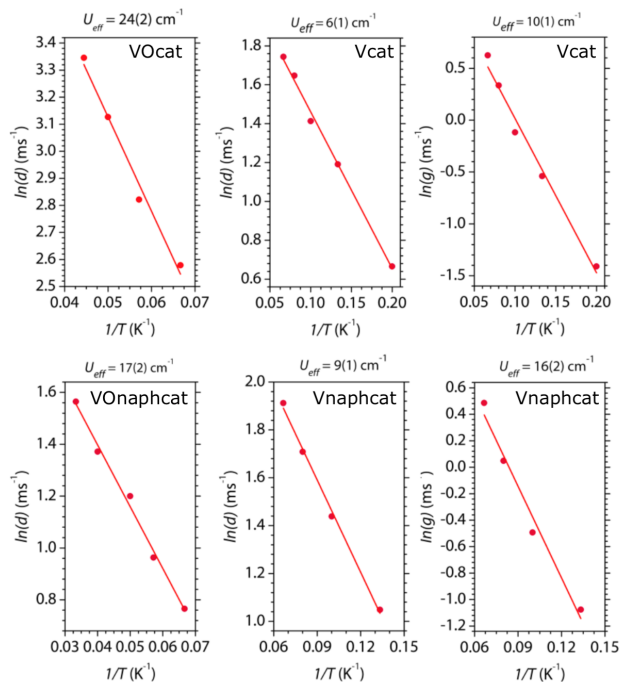


**Figure 9.14:** Arrhenius plots of  $d$  and  $g$  parameters extracted from the fit of the Brons-van Vleck or the extended Brons-van Vleck model.

Molecule	$d$ ( $\text{cm}^{-1}$ )	$g$ ( $\text{cm}^{-1}$ )
<b>VOcat</b>	24	-
<b>VOnaphcat</b>	17	-
<b>Vcat</b>	6	10
<b>Vnaphcat</b>	9	16

**Table 9.6:** Extracted values of the  $d$  and  $g$  parameters. The oxovanadium(IV) complexes show a unique activation energy value, whereas the vanadium(IV) counterparts show double activation energy values.

### 9.2.3 Spectroscopic investigation

An accurate determination of the energy of the active phonons in these compounds is crucial for a better understanding of the correlation between vibra-

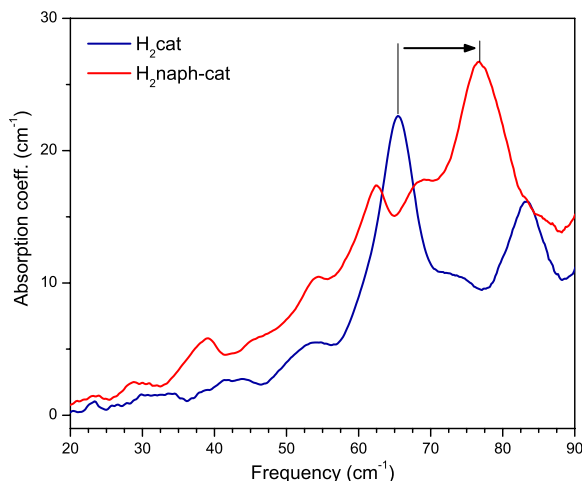


**Figure 9.15:** Comparison between experimental THz spectra of  $\text{H}_2\text{cat}$  and  $\text{H}_2\text{naph-cat}$ . The arrow indicates the blue shift of the predominant lowest energy peak due to the stiffening of the molecular skeleton passing from one to two condensed aromatic rings.

tional modes and the spin dynamics. Room temperature THz spectra, reported in Figure 9.15, have been collected on protonated ligands  $\text{H}_2\text{cat}$  and  $\text{H}_2\text{naph-cat}$ . The comparison between the spectra indicates that the structural modification herein introduced by expanding the ligand from one to two condensed aromatic rings has important implications on the overall molecular rigidity. Indeed, the predominant lowest energy absorption occurs at a frequency ca.  $15\text{ cm}^{-1}$  higher for the  $\text{H}_2\text{naph-cat}$  ligand, with respect to the  $\text{H}_2\text{cat}$  one.

Room-temperature THz-TDS spectra were recorded in the 0.3-3.0 THz range ( $15\text{-}100\text{ cm}^{-1}$ ) to characterize the low energy vibration frequencies of the coordination compounds under investigation (Figure 9.16). Such spectra appear more complicated with respect to those of  $\text{VO}(\text{acac})_2$  mentioned in Chapter 9.1.

This might be partially related to the presence of the  $\text{PPh}_4^+$  counterion, which was absent in the previously studied compound.

The spectra of **VOcat** and **VOnaphcat** show lowest energy absorptions at ca.  $35$  and  $52\text{ cm}^{-1}$ , and  $20$  and  $34\text{ cm}^{-1}$ , respectively. Interestingly, in this frequency region, the lowest-energy vibrational modes are shifted toward higher frequencies for the complex of the smaller catecholate ligand, with respect to that of the naphthalene-catecholate, in agreement with the magnetic analysis. More specifically, assuming the relation  $U_{eff} = \hbar\omega_\alpha/2$  to hold[5][9], the magnetic analysis suggests that the phonons involved in the relaxation mechanism should have a frequency of  $48$  and  $34\text{ cm}^{-1}$ , for **VOcat** and **VOnaphcat**, respectively, which agrees with the spectroscopic findings. Both the oxovanadium(IV) complexes show one additional peak at lower frequencies that was not determined through

9.2. The role of the rigidity of the coordination shell

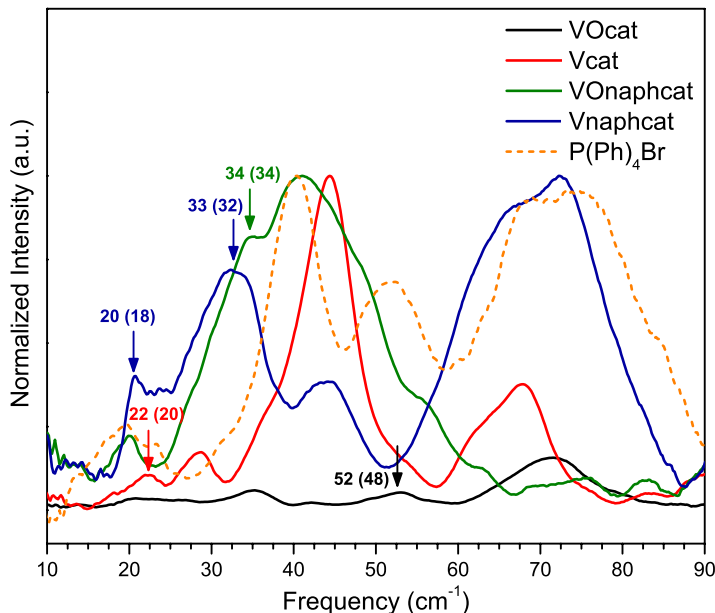


**Figure 9.16:** THz spectra of the investigated complexes and P(Ph)<sub>4</sub>Br (orange dashed line). The arrows indicate the vibrational modes involved in the spin dynamics together with their experimental frequencies and those found through magnetic susceptibility analysis (shown in parentheses).

the magnetic analysis. According to a recently reported study on the role of intramolecular vibrations as mediators of spin-lattice relaxation, each vibrational mode should couple with the spin in a different extent, as a function of the type of vibration and electron occupancy in the metal *d*-orbitals[10]. Consequently, it is not surprising that the lowest-energy vibrational mode observed herein for **VOcat** and **VOnaphcat** is not strongly coupled with the spin to promote efficient relaxation. Indeed, since they have the same coordination geometry, they show the same feature. Accordingly, the nature of the lowest-energy detected vibrational mode is likely to be the same, with a different resonating frequency, because of the different ligand mass. The spectra of the vanadium(IV) tris-chelated complexes **Vcat** and **Vnaphcat** show, in general, low-energy absorption bands, which are shifted toward lower energies, with respect to the vanadyl-based complexes, again in agreement with the findings of the magnetic analysis. More specifically, the former show lowest-energy absorptions at 22 cm<sup>-1</sup> and ca. 28 cm<sup>-1</sup> and the latter at 20 and 33 cm<sup>-1</sup>. A correlation with the magnetic analysis can be found for **Vnaphcat**, with two phonon modes expected at 18 and 32 cm<sup>-1</sup>, whereas, for **Vcat**, relevant phonon modes are expected at 12 and 20 cm<sup>-1</sup>, the former falling out from our detection range. Finally, it should be remarked that all spectra show an absorption at about 40 cm<sup>-1</sup>, where the first vibrational mode of the

$\text{PPh}_4^+$  counterion is observed, but no correspondence to relaxation processes is observed for this vibration. The comparison between the magnetically predicted values of the energy barrier and the measured phonons frequency is reported in table 9.7.

Molecule	Predicted activation values ( $\text{cm}^{-1}$ )		Measured phonons frequencies ( $\text{cm}^{-1}$ )	
<b>VOcat</b>	48		52	
<b>VOnaphcat</b>	34		34	
<b>Vcat</b>	12	20	-	22
<b>Vnaphcat</b>	18	32	20	33

**Table 9.7:** Comparison between the predicted values of the energy barrier, assuming  $U_{eff} = \hbar\omega_\alpha/2$ , and the phonons frequencies measured by THz-TDS. The oxovanadium(IV) complexes show a unique activation energy value, whereas the vanadium(IV) counterparts show double activation energy values. The predicted phonon at  $12 \text{ cm}^{-1}$  for **Vcat** falls out of the available experimental frequency window.

## 9.2.4 Conclusions

We have here investigated the spin-lattice relaxation of four  $\text{V}^{IV}$ -based potential molecular qubits where specific structural modifications have been introduced to study correlations between the spin dynamics and the role played by low-energy vibrational modes as mediators of spin-lattice relaxation. Both the influence of the different coordination geometries, *square-pyramidal* versus *trigonally distorted octahedral*, as well as the increased rigidity of the coordinating ligand, have been correlated to the observed spin-lattice relaxation. The analysis of the temperature dependence of the relaxation time did not show major differences between catecholate and naphthalene-catecholate complexes, while substantial differences between square pyramidal and octahedral complexes were observed. Indeed, the former provide relaxation times that are ca. 10-fold longer, with respect to the latter. A similar factor was also observed for another independent pair of vanadium(IV) and oxovanadium(IV) complexes with a different ligand, thus indicating that the specific coordination geometry plays a key role on the absolute values of the relaxation time, not simply by generically increasing them, but enhancing the relaxation times by a specific factor, independently from the coordinating ligand structure. Analysis of the magnetic field dependence of  $\tau$  confirms the generality of the Arrhenius-type behavior which allows to find further correspondence between the activation energy values obtained by this magnetic analysis and the frequency of the low-energy phonons spectroscopically detected by THz-TD spectroscopy. Concerning the temperature dependence of the spin-lattice relaxation time it emerges that naphthalene-catecholate, that has a more



### 9.3. Investigation of the spin-phonon coupling by first-principles approach

rigid structure than catecholate as established by the THz measurements, provides minor enhancements of the relaxation times only in the high-temperature range. The slower relaxation of **VOcat**, compared to **VOnaphcat**, at low temperatures correlates with the trend of the lowest-energy vibrational modes. Indeed, they occur at slightly lower energy in the latter.

## 9.3 Investigation of the spin-phonon coupling by first-principles approach

---

**The chapter is based on the following publication**

---

“First-Principles Investigation of Spin-Phonon Coupling in Vanadium-Based Molecular Spin Quantum Bits”. Albino, A., Benci, S., Tesi, L., Atzori, M., Torre, R., Sanvito, S., Sessoli, R., and Lunghi, A. In: *Inorganic chemistry* 58(15) (2019), pp. 10260-10268.

---

The comparative study of the previous section is here extended to other two vanadium-(IV) molecular complexes, namely  $[\text{PPh}_4]_2[\text{VO}(\text{dmit})_2]$  and  $[\text{PPh}_4]_2[\text{V}(\text{dmit})_3]$ , hereafter labeled **VOdmit** and **Vdmit** respectively, where  $\text{dmit} = 1,3\text{-dithiole-2-thione-4,5-dithiolate}$  and  $\text{PPh}_4 = \text{tetraphenylphosphonium}$ . In particular, the theoretical investigation of the spin-lattice relaxation on **VOcat**, **Vcat**, **VOdmit** and **Vdmit** has been carried out.

The vibrational modes can be divided in lattice vibrations, i.e. translations and rotations of the molecular units, and molecular vibrations, i.e. internal, which make the length of the covalent bonds as well as the angle between two bonds vary. The first ones will be called rigid motions while the second one nonrigid motions. The efficiency of each normal mode can be ascertained considering the fraction of rigid motions with respect to the fraction of nonrigid motions transferred to the molecule. The geometrical displacement that strongly determines spin-state perturbation is the intramolecular one, which twists molecules affecting the first coordination shell.

### 9.3.1 Molecular and crystal structure

The **VOdmit** (Figure 9.17(a)) crystallizes in the monoclinic  $C2/c$  space group with half of the anionic complex and one tetraphenylphosphonium counterion in the asymmetric unit. Its crystal structure consists of  $[\text{VO}(\text{dmit})_2]^{2-}$  anions alter-

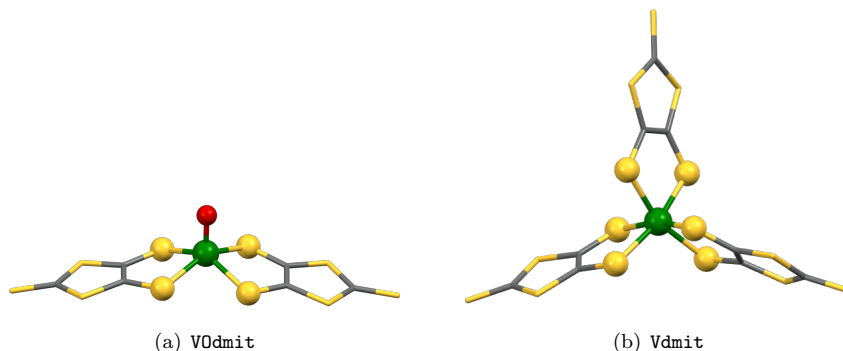


**Figure 9.17:** Molecular structure of (a) **VOdmit**, (b) **Vdmit**. Color code: V=green, O=red, S=yellow, C=grey, H=white.

nated in V=O up and V=O down configurations separated by tetraphenylphosphonium cations. The shortest V...V distance is in the 10.50-15.79 Å range. It presents a distorted square pyramidal coordination geometry with the metal ions slightly above the basal plane (0.68 Å). The apical position is occupied by an oxo ligand which forms a double bond with the Vanadium(IV) ion with a V=O bond distance of 1.594 Å whereas the V–S single bond length is 2.386 Å. **Vdmit** (Figure 9.17(b)) crystallizes in the monoclinic  $P2_1/c$  space group with one anionic complex and two tetraphenylphosphonium counterions in the asymmetric unit. The crystal structure consists of homoleptic tris-chelated  $[V(dmit)_3]^{2-}$  anions showing  $\Lambda$  and  $\Delta$  chirality and tetraphenylphosphonium cations. The shortest V...V distances are in the 9.75-15.98 Å range and are comparable to those observed for **VOdmit**. The coordination geometry around the V(IV) ion is a trigonally distorted octahedron, similarly to **VOcat** and **VOnaphcat**, with an average V–S distance of 2.386 Å. The main parameters described above are summarized in table 9.8. The molecular and crystal structures of **Vcat** and **VOcat** are extensively described in chapter 9.2.1.

Molecules	Space group	Point group	V=O distance (Å)	V–S distance (Å)	V...V shortest distance (Å)
<b>VOdmit</b>	monoclinic $C2/c$	$C_2$	1.594	2.386-2.387	10.50
<b>Vdmit</b>	monoclinic $P2_1/c$	$C_1$	-	2.380-2.394	9.75

**Table 9.8:** Main parameters of the crystal structures for **VOdmit** and **Vdmit**.

### 9.3.2 Spectroscopic investigation

THz-TDS spectra as a function of temperature in the 10-120  $\text{cm}^{-1}$  range have been recorded and used as experimental validation of the simulations.

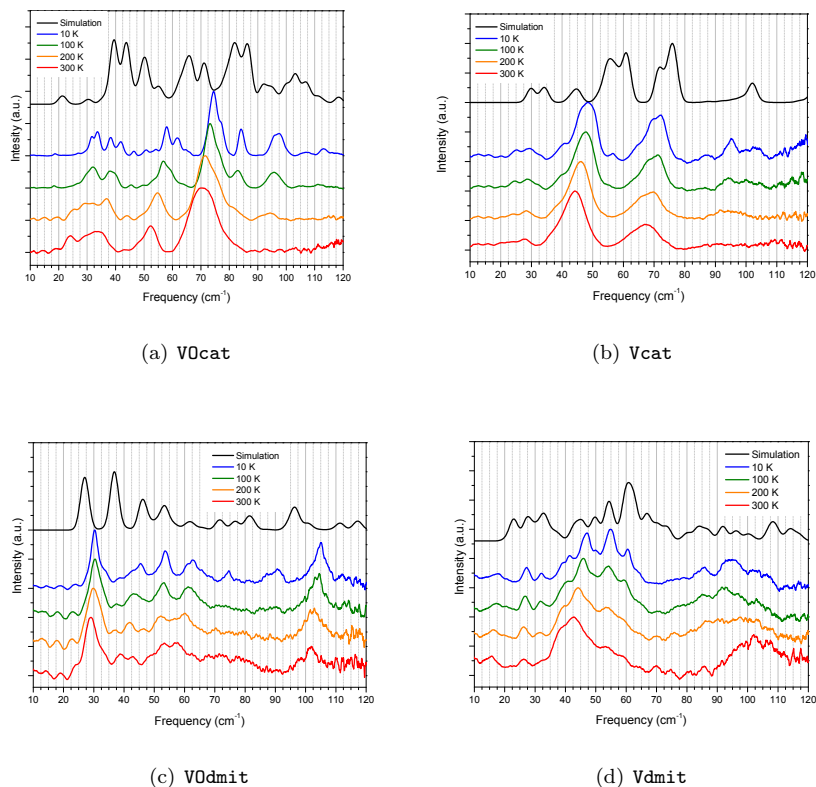


**Figure 9.18:** Experimental and simulated (black solid line) THz spectra in the 10-120  $\text{cm}^{-1}$  range recorded at 10, 100, 200, 300 K of **VOcat** (a), **Vcat** (b), **VOdmit** (d) and **Vdmit** (e).

The simulated spectra of the four complexes show an overall good agreement with the lowest temperature (10 K) experimental ones. A temperature increase causes a shift to lower frequencies of some vibrational modes because of the presence of anharmonic interactions, together with a softening of the crystal lattice. Simulations corresponding to 0 K, indeed, are blue-shifted with respect to the experimental lowest temperature spectra. The lowest calculated vibrations occur at 13.3  $\text{cm}^{-1}$  for **Vdmit** and 18.5  $\text{cm}^{-1}$  for **VOdmit** and also at 27.6  $\text{cm}^{-1}$  for **Vcat** and 20.7  $\text{cm}^{-1}$  for **VOcat**. Dithiolate compounds show vibrations at lower frequencies with respect to the catecholate ones, probably because of the larger radius of the first coordination sphere and the higher atomic mass of sulphur

*CHAPTER 9. THz spectroscopy as innovative probe of the molecular Qubits performance*

atoms. Accordingly, longer bond lengths are generally associated with softer bonds and, therefore, with lower vibrational frequencies. A deconvolution of translations, rotations, and intramolecular motions of the single molecule[11][12] is shown in Figure 9.19. The low-energy modes are dominated, for all compounds, by rigid translations and rotations of the molecule in the crystal, but intramolecular contributions are also present and become the dominant ones in increasing the energy modes. The calculated decomposition shows, for hexacoordinated compounds, a higher average internal contribution. Among the hexacoordinated ones, the catecholate compound shows a reduced rotational contribution.

9.3. Investigation of the spin-phonon coupling by first-principles approach

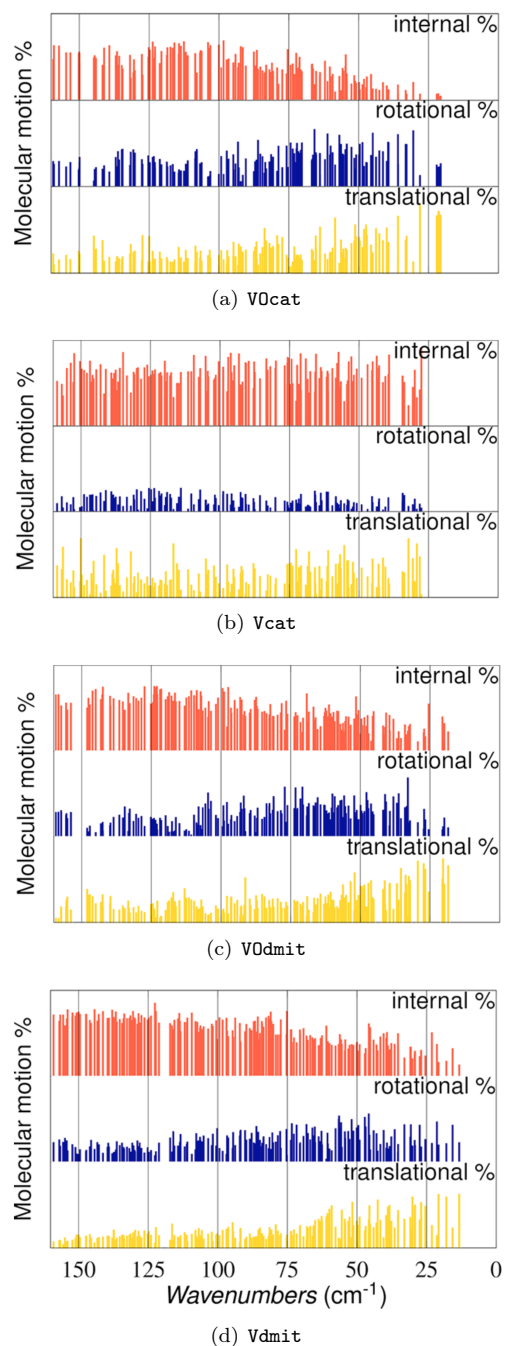


**Figure 9.19:** Total molecular motion associated with normal modes in the low frequency range (0-150 cm<sup>-1</sup>) decomposed in intramolecular percentage (red), rotational percentage (blue), and translational percentage (yellow) for **VOcat** (a), **Vcat** (b), **VOdmit** (d) and **Vdmit** (e).

### 9.3.3 Spin-phonon coupling analysis

The theory of the spin-phonon coupling has been extensively discussed in chapter 5. In the case herein reported, let us limiting the study of the spin dynamics only in the presence of an external magnetic field,  $\mathbf{B}$ . The spin Hamiltonian of an  $S = 1/2$  system will only contain the Zeeman term.

$$\mathcal{H}_{ze} = \mu_B \mathbf{B} \cdot \hat{\mathbf{g}} \cdot \mathbf{S} \quad (9.6)$$

The hyperfine and intermolecular spin-spin dipolar interactions have been neglected in equation 9.6 because in high fields their matrix elements are negligible. When the relaxation properties are taken into account, it is necessary to introduce in the description the effects of the environment on the dynamics of the system described. In this case, the spin system interacts with an environment made of the crystals' phonons. Their Hamiltonian, describing the normal modes of vibration, is displayed in equation (4.3). In the first approximation, assuming a weak coupling between the phonon bath and the spin degrees of freedom, the spin-phonon coupling Hamiltonian can be taken as linear in the atomic displacement, as reported in equation (5.5). The spin dynamics can then be described by the Redfield equations[13], reported in equations (5.6) and (5.7). Understanding the interactions contributing to  $V_{ab}^\alpha$  (equation (5.8)) is the main focus of this work because it contains the spin-phonon coupling coefficients  $\left(\frac{\partial H_s}{\partial q_\alpha}\right)$ , which set the spin relaxation time scale.

Estimating  $\mathcal{H}_{s-ph}$  requires calculation of the derivatives of  $\hat{\mathbf{g}}$  with respect to the structural perturbations and calculation of the periodic crystals' normal modes. The cumulative spin-phonon coupling coefficients (equation (9.7)) represent the sum of every atomic contribution to the spin-phonon coupling and allow us to define dynamical magnetostructural correlations.

$$|\partial g| = \sum_{i,v}^{M,3} \sum_{s,t}^3 \left| \left( \frac{\partial g_{st}}{\partial X_{iv}} \right)_0 \right| \quad (9.7)$$

In equation (9.7) the index  $s$  runs over the number of atoms in the molecule and  $t$  runs over the Cartesian coordinates.

It should be noted that the differences in the cumulative spin-phonon coupling across the series can be due to both the chemical nature of the ligand and the coordinating geometry around the metal center. For complexes with the same ligand, the g-tensor elements are less perturbed in the pyramidal coordination with respect to the octahedral one. When complexes with the same coordination geometry but different ligands are compared, it appears that a stronger effect on the spin-phonon coupling is observed, with the catecholate being more prone to g-

### 9.3. Investigation of the spin-phonon coupling by first-principles approach

tensor perturbations than the dithiolate ones. In order to explain these features, it is important to correlate the  $\mathbf{g}$ -tensor anisotropy and how this is modified by atomic displacements, i.e.,  $\mathbf{g}$  and  $|\partial\mathbf{g}|$ . These two quantities show the same trend across the series of molecules investigated as a consequence of a common microscopic origin, namely, the magnitude of the orbital angular momentum in the ground state[14]. This quantity, accessible from the *ab-initio* calculations, can be conveniently estimated from the magnitude of the 3d orbitals energy splitting[14], shown in Figure 9.20.

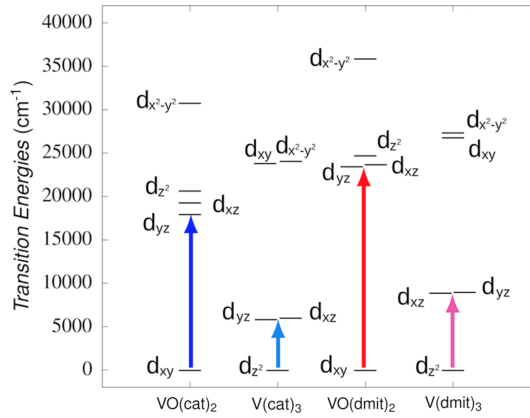


**Figure 9.20:** Energy ladder of the 3d valence shell of the four compounds analyzed calculated by CASSCF+NEVPT2. The arrows represent the lowest-energy electronic transition in each complex.

The difference in the splitting of the  $d$  orbitals is dominated by the oxido versus nonoxido coordination mode. For the same coordination mode, cathecolate ligands induce smaller splitting than dithiolate ones. The transition energy to the first excited state (marked with an arrow in Figure 9.20), calculated by CASSCF+NEVPT2, shows a good correlation with derivatives of  $\mathbf{g}$ , where larger  $|\partial\mathbf{g}|$  correspond to smaller  $\Delta E$ . Interestingly, oxygen-based ligands yield a smaller splitting of the electronic states with respect to the sulphur-based ones. Although useful to understand general trends, the cumulative spin-phonon coupling coefficients do not provide any information concerning the temperature at which specific atoms will start vibrating. This information can be obtained from the study of the spin-phonon coupling coefficients projected on the normal modes:

$$\left(\frac{\partial\mathbf{g}}{\partial q_\alpha}\right)_0 = \sum_i^{3M} \sqrt{\frac{\hbar}{\omega_\alpha m_i}} L_{i\alpha} \left(\frac{\partial\mathbf{g}}{\partial X_i}\right)_0 \quad (9.8)$$

where the index  $\alpha$  runs over the normal modes, the index  $i$  over the  $3M$  molecular Cartesian coordinates,  $L_{i\alpha}$  is the Hessian's eigenvector matrix,  $m_i$  is

the atomic mass, and  $\omega_\alpha$  is the normal mode angular frequency. The subscript 0 indicates that derivatives have been calculated in the DFT-optimized equilibrium configuration. The phonon-projected spin-phonon coupling coefficients as a function of the phonons vibrational frequency are reported in Figure 9.21.

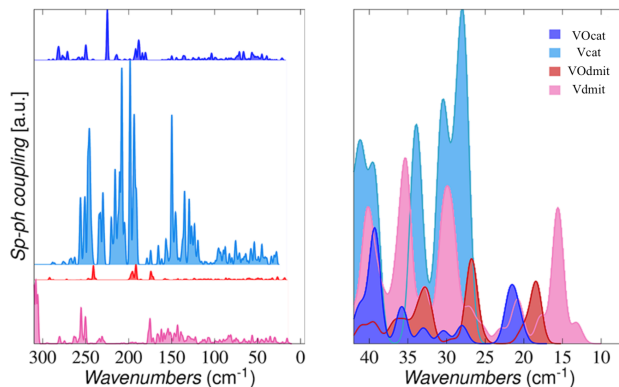


**Figure 9.21:** *Left panel:* Spin-phonon coupling coefficients in the 0-300  $\text{cm}^{-1}$  range for the four analyzed compounds. A Gaussian shape was applied to each harmonic normal mode, considering a width parameter equal to 2  $\text{cm}^{-1}$ . *Right panel:* Zoom of the coupling coefficient patterns in the low-frequency region.

The overall behavior of the spin-phonon coupling follows the one observed for  $|\partial\mathbf{g}|$ , that is, the strength of the coupling, and ranks the molecules in the following order: **VOdmit** < **VOcat** < **Vdmit** < **Vcat**. Thus, the spin-phonon coupling in vanadyl compounds is weaker than that in hexacoordinated molecules. Furthermore, catecholite ligands offer a stronger coupling than dithiolates. The presence of different donor atoms has different effects on the low and high energy ranges of the vibrational spectrum. Indeed, dithiolate ligands, which exhibit a more diffuse coordination sphere because of the softer nature of sulphur atoms, show the presence of several normal vibrations at lower frequencies and a weaker perturbation of the spin states by vibrational modes, as shown by the lower spin-phonon coupling amplitudes (Figure 9.21). The second effect is particularly remarkable in the higher energy vibrations, suggesting that the spin-lattice relaxation time of dithiolate should exhibit a weaker temperature dependence.

### 9.3.4 Conclusions

The spin-lattice relaxation time,  $\tau$ , as function of the external magnetic field and temperature is shown in Figure 9.22 [8][15]. It is clear that at low temperature catecholite complexes relax slower than the dithiolate ones. This is consistent with the low-energy vibrational modes of both compounds. Then, it is worth noting that molecules presenting hexacoordination relax faster than those



### 9.3. Investigation of the spin-phonon coupling by first-principles approach

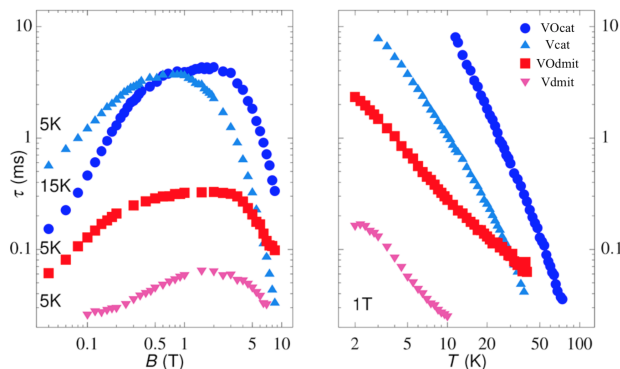


**Figure 9.22:** Spin-lattice relaxation time extracted from AC susceptibility measurements as a function of the external magnetic field (left) and temperature (right). Data have been taken from previous works[8][15].

with pentacoordinated geometry, regardless of the chemical nature of the ligands. Turning to a comparison of the relaxation time among iso-ligand species, we note that **Vcat** relaxes faster than **VOcat** by virtue of a much stronger spin-phonon coupling. This suggests that the spin-phonon coupling intensity and structural rigidity, here assumed proportional to the frequency of the first  $\Gamma$ -point vibration, both participate in the determination of the spin-lattice relaxation time. This picture is confirmed by the behavior of the relaxation times when the temperature increases and higher energy modes become populated. The spin-lattice relaxation time of molecule **VOdmit** decays with temperature at a much slower rate than those of **VOcat** and **Vcat**, and, in fact, there is a crossover between the relaxation times of **Vcat** and **VOdmit** at around 30 K, with another one between **VOcat** and **VOdmit** expected at higher temperatures. This experimental feature correlates well with the weak spin-phonon coupling observed over a wide frequency range for **VOdmit** when it is compared to those of **VOcat** and **Vcat**. Concerning the **Vdmit**, pulsed EPR investigations of crystalline compounds, diluted in diamagnetic analogues, have revealed that its coherence time collapses at ca. 100 K as a result of the sharp decay of  $T_1$  for temperatures above 30 K[8]. This observation correlates with the calculated spin-phonon coupling (Figure 9.21). Indeed, spin-phonon couplings comparable between **VOdmit** and **Vdmit** are observed in the low-frequency range, while in the high-frequency range, **Vdmit** presents larger couplings. At high temperature, as the high-energy modes become more occupied, a significant enhancement of the spin-lattice relaxation in **Vdmit** is therefore expected.

## 9.4 Arranging the Qubit units into a Metal Organic Framework

---

### The chapter is based on the following publication

---

“Scaling Up Electronic Spin Qubits into a Three-Dimensional Metal-Organic Framework”. Yamabayashi, T., Atzori, M., Tesi, L., Cosquer, G., Santanni, F., Boulon, M. E., Morra, E., Benci, S., Torre, R., Chiesa, M., Sorace, L. Sessoli, R., and Yamashita, M. In: *Journal of the American Chemical Society* 140(38) (2018), pp. 12090-12101.

---

This section is dedicated to the acquisition of additional insights into the role of the crystal lattice properties in determining the performance of potential qubit embedded into a 3D metal organic framework (MOF). The selected compound is a porous vanadyl-based 3D MOF of formula [VO(TCPP–Zn<sub>2</sub>–bpy)] (TCPP = tetracarboxylphenylporphyrinate; bpy = 4,4'-bipyridyl), hereafter labeled **VOTCPP**. Also, a comparative study with the representative mononuclear molecular building block [VO(TPP)] (TPP = tetraphenylporphyrinate), hereafter labeled **VOTPP**, has been herein reported. Moreover, their dilutions in a isostructural diamagnetic matrix have been prepared and reported as follow: [VO(TCPP)] and [TiO(TCPP)] in 5:95 molar ratio, hereafter labeled **VOTCPP 5%**, [VO(TPP)] and [TiO(TPP)] in 30:70 molar ratio, hereafter labeled **VOTPP 30%** and [VO(TPP)] and [TiO(TPP)] in 2:98 molar ratio, hereafter labeled **VOTPP 2%**. It is worth nothing that an extensive study of **VOTPP** and its 2% dilution concerning the influence of strong THz radiation on the spin dynamics will be discussed in chapter.

### 9.4.1 Molecular and crystal structure

The **VOTCPP** crystallizes in the tetragonal  $P_4$  space group with one anionic complex, two Zn<sup>2+</sup> ions, and one bpy molecule in the unit cell, the asymmetric unit being one-fourth of the molecule. The peripheral carboxyl substituents of the porphyrin macrocycle interact with Zn<sup>2+</sup> to form 2D layers where the porphyrin units are connected in a 4-folded symmetry through [Zn<sub>2</sub>(COO)<sub>4</sub>] subunits. The pillar-like bpy ligands then allow connection between the 2D layers to form a 3D MOF by further axial coordination between pairs of [Zn<sub>2</sub>(COO)<sub>4</sub>] subunits (Figure 9.23(a)). The obtained structure has 3D channels with a pore dimension

#### 9.4. Arranging the Qubit units into a Metal Organic Framework

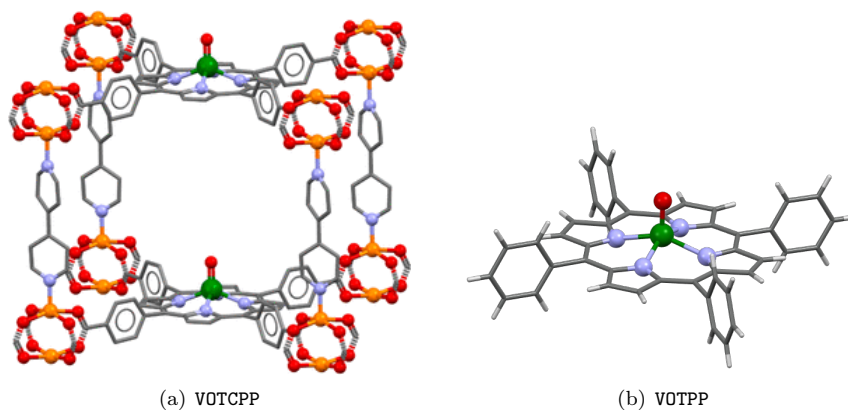


**Figure 9.23:** Molecular structure of (a) **VOTCPP**, (b) **VOTPP**. Color code: V=green, O=red, N=violet, C=grey, H=white, Zn=orange.

of  $1.66 \times 1.38 \text{ nm}^2$  along the  $a$  and  $b$  axes. The coordination geometry of the  $\text{Zn}^{2+}$  ions, which templates the formation of the overall crystal structure, consists of a square pyramid where pairs of  $\text{Zn}^{2+}$  ions are bridged in a  $\mu$ -type binding mode by four carboxylate ligands. The resulting equatorial plane around each  $\text{Zn}^{2+}$  ion is thus formed by four oxygen donor atoms, while the axial position of the square pyramid is occupied by the nitrogen donor of a bpy ligand, which bridges pairs of  $\text{Zn}^{2+}$  ions from adjacent 2D layers. The molecular structure of the anionic complex  $[\text{VO}(\text{TCPP})]^{4-}$  shows a vanadium(IV) ion in a square pyramidal coordination geometry with the metal ion slightly above the basal plane (ca.  $0.59 \text{ \AA}$ ) formed by the four nitrogen donor atoms of the porphyrin macrocycle. The  $\text{V}=\text{O}$  moiety is sitting on the 4-fold symmetry axis and is disordered on two positions, symmetric with respect to the macrocycle ring, with 50:50 occupancy factors, leading to a nonpolar crystal structure. The  $\text{V}=\text{O}$  and  $\text{V}-\text{N}$  distances,  $1.60$  and  $2.09 \text{ \AA}$ , respectively, are in agreement with what is usually encountered for similar vanadyl complexes. The planes of the phenyl substituents are  $90^\circ$  tilted with respect to the plane of the porphyrin macrocycle. This leads to an overall crystal structure of tetragonal symmetry where all vanadyl moieties are oriented along the  $c$  axis. The  $\text{V} \cdots \text{V}$  shortest distances in the crystal structure correspond to the unit cell distances, i.e.,  $13.9 \text{ \AA}$  along the  $c$  axis and  $16.6 \text{ \AA}$  in the  $ab$  plane. Finally, it should be noted that the pyridine rings of the bpy ligand appear disordered in two  $90^\circ$ -tilted orientations, with the orientation of the two independent rings  $45^\circ$ -tilted with respect to each other.

The **VOTPP** crystallizes in the tetragonal  $I_4$  space group with two neutral complexes in the unit cell; the asymmetric unit is one-fourth of the molecule also in this case. The crystal structure consists of neutral vanadyl tetraphenylpor-

phyrinate complexes with all V=O units lying on the 4-fold symmetry  $c$  axis. The shortest V...V distance is 10.9 Å and involves metal complexes of adjacent layers. No significant intermolecular contacts involving the phenyl rings are present. The molecular structure of the complex is reported in Figure 9.23(b). The coordination geometry around the V<sup>(IV)</sup> ion is a square pyramid with a V=O distance of 1.58 Å and V–N distances of 2.11 Å. As already observed for **VOTCPP**, the metal-oxido cationic moiety is disordered along the tetragonal axis on two positions with equal occupancy factors, with the metal center lying 0.58 Å from the basal plane of the porphyrin macrocycle. The main parameters of the crystal structure of both the compound are reported in the table 9.9.

Molecules	Space group	Point group	V=O distance (Å)	V–N distance (Å)	V...V shortest distance (Å)
<b>VOTCPP</b>	tetragonal $P_4$	$C_4$	1.60	2.09	13.9
<b>VOTPP</b>	tetragonal $I_4$	$C_4$	1.58	2.11	10.9

**Table 9.9:** Main parameters of the crystal structures for **VOTCPP** and **VOTPP**.

### 9.4.2 Magnetic properties

AC susceptibility measurements were performed on microcrystalline samples of **VOTCPP** and **VOTPP** and the crystalline dispersion **VOTPP 30%** to investigate their magnetization dynamics. The choice to study the dilution **VOTPP 30%** is due to the pronounced difference in the spin concentration between **VOTCPP** and **VOTPP**. Indeed, the former has a spin concentration of 0.26 spin nm<sup>-3</sup>, whereas the latter 1.1 spin nm<sup>-3</sup>. **VOTPP 30%** provides a spin concentration of 0.34 spin nm<sup>-3</sup>, which is closer to that of **VOTCPP** and thus associated with a comparable dipolar internal magnetic field. The magnetization dynamics was studied as a function of the static magnetic field in a wide magnetic field range (0.0-8.5 T) at different temperatures (5.0, 7.5, and 10.0 K) for each compound. The relaxation time,  $\tau$ , which is representative of the spin-lattice relaxation time, for **VOTCPP**, **VOTPP**, and **VOTPP 30%** has been obtained applying the Debye model[16], and are reported in Figure 9.24. **VOTCPP** and **VOTPP 30%** have a comparable values of spin-lattice relaxation times in a wide range of temperature, whereas **VOTPP** has a lower one. Indeed, it follows the trend of the spin concentration. All compounds show the expected nonmonotonous behavior, as already seen in the previous chapters. A striking feature in the magnetic field dependence of the relaxation times is the

#### 9.4. Arranging the Qubit units into a Metal Organic Framework

dip shown by all compounds at 2.0 T. This feature is particularly pronounced for **VOTPP** and less pronounced for its 30% dilution, suggesting that the presence of this dip might be related to the spin-phonon bottleneck effect.

The magnetic field dependence of  $\tau$  for the MOF is reproduced by the Brons-van Vleck model[3][4] with a slight modification, equation (9.9).

$$\tau^{-1} = cB^m + d \left( \frac{1 + eB^2}{1 + fB^2} \right) \quad (9.9)$$

In which the first term, related to the direct process, has the exponent  $m$  of the magnetic field,  $B$ , set free to vary. In previous cases,  $m$  was kept fixed and equal to 4. The best fit of the experimental data shows a value of  $m = 3$ , highlighting a weaker magnetic field dependence of the relaxation time. The extended Brons-van Vleck model has been used to properly reproduce the data obtained for **VOTPP 30%**:

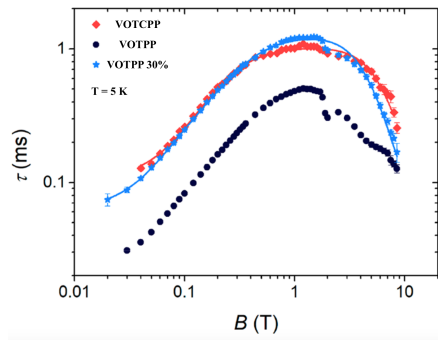
$$\tau^{-1} = cB^m + d \left( \frac{1 + eB^2}{1 + fB^2} \right) + g \left( \frac{1 + eB^2}{1 + hB^2} \right) \quad (9.10)$$

as already done for **Vcat** and **Vnaphcat** in chapter 9.2. Finally, it should be highlighted that the modeling of the magnetic field dependence of the spin-lattice relaxation time for **VOTPP** is not feasible because the distortions observed between 2.0 and 7.0 T do not allow for reasonable fits with either standard or extended Brons-van Vleck models.

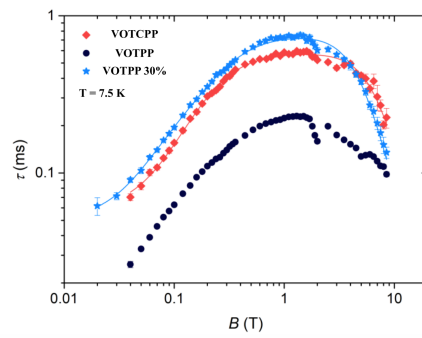
Continuous wave (CW) and pulsed EPR measurements have been performed on magnetically diluted samples **VOTCPP 5%** and **VOTPP 2%**. The CW-EPR spectrum is shown in Figure 9.25, and is characterized by the 8-fold structure due to the coupling between the  $S=1/2$  electronic spin of Vanadium(IV) and the  $I=7/2$  nuclear spin of its most abundant isotope  $^{51}\text{V}$ .

Inversion recovery experiments[17] were performed in the 5.0-290 K temperature range at X-band frequency to investigate the temperature dependence of the spin-lattice relaxation time ( $T_1$ ) at the resonant magnetic field corresponding to the hyperfine transition  $M_I = -1/2 \rightarrow +1/2$  (Figure 9.26). The temperature dependence of  $T_1$  for the magnetically diluted samples **VOTCPP 5%** and **VOTPP 2%** shows an increase of the slope on increasing the temperature, which is characteristic of the crossover from a dominating direct process of relaxation at low temperature to a Raman mechanism at high temperatures.  $T_1$  values of the former at low temperature are ca. one order of magnitude lower than that of latter despite the similar spin concentration of the two compounds. As the temperature increases, the spin-lattice relaxation time for **VOTPP 2%** starts to decrease more abruptly above 30 K, whereas the MOF shows such a behavior only at higher temperature and with a weaker temperature dependence.

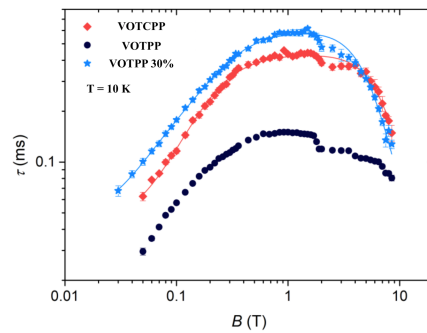
CHAPTER 9. THz spectroscopy as innovative probe of the molecular Qubits performance



(a) 5.0K



(b) 7.5K



(c) 10.0K

**Figure 9.24:** Magnetic field dependence of  $\tau$  extracted from AC susceptibility measurements for microcrystalline samples of **VOTCPP**, **VOTPP** and **VOTPP 30%** in the 0.0-8.5 T range at 5.0 K (a), 7.5 K (b) and 10.0 K (c). Solid lines are the best fit of the models.

#### 9.4. Arranging the Qubit units into a Metal Organic Framework

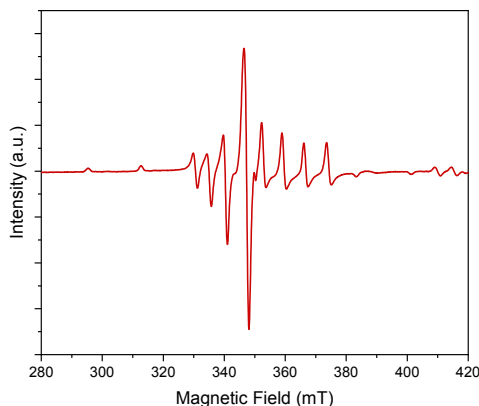


**Figure 9.25:** Experimental CW-EPR spectrum of **VOTPP** at X-band frequency (9.7 GHz).

Consequently, the curves for the two compounds intersect around 60 K, and at room temperature, the spin-lattice relaxation time for **VOTCPP 5%** reaches a value of ca.  $1 \mu\text{s}$  vs  $0.6 \mu\text{s}$  observed for **VOTPP 2%**. To investigate the quantum coherence in detail and to determine the phase memory time ( $T_m$ ) for both the diluted samples as a function of the temperature, echo decay experiments[17] were also performed. Because  $T_1$  values, which limit the  $T_m$  values especially at high temperatures[8], are sufficiently long for both compounds in the whole investigated temperature range, echo decay traces (Figure 9.26) were detected up to room temperature for both the compounds. The thermal variations of  $T_m$  for **VOTCPP 5%** and **VOTPP 2%** show an almost temperature independent behavior in the 5.0-100 K range for the former (ca.  $0.5 \mu\text{s}$ ) and in the 5.0-60 K range for the latter (ca.  $1.0 \mu\text{s}$ ), with relative values that follow the corresponding  $T_1$  values. At 150 K,  $T_m$  assumes the same value for the two samples (ca.  $0.4 \mu\text{s}$ ) and decreases to reach the lowest values at room temperature (ca.  $0.14 \mu\text{s}$ ). It is interesting to note that a crossover between the  $T_m$  values occurs in much the same way as observed for  $T_1$  at slightly lower temperatures.

#### 9.4.3 Spectroscopic investigation

THz spectra in the  $10\text{-}110 \text{ cm}^{-1}$  range were recorded on polycrystalline powder of **VOTCPP** and **VOTPP** dispersed in polyethylene pellets (Figure 9.27). A striking difference between the isolated [VO(TPP)] units and the extended structures of the MOF is observed. Indeed, **VOTPP** shows a well-defined absorption band at ca.  $67 \text{ cm}^{-1}$  at room-temperature, which is absent in **VOTCPP**.

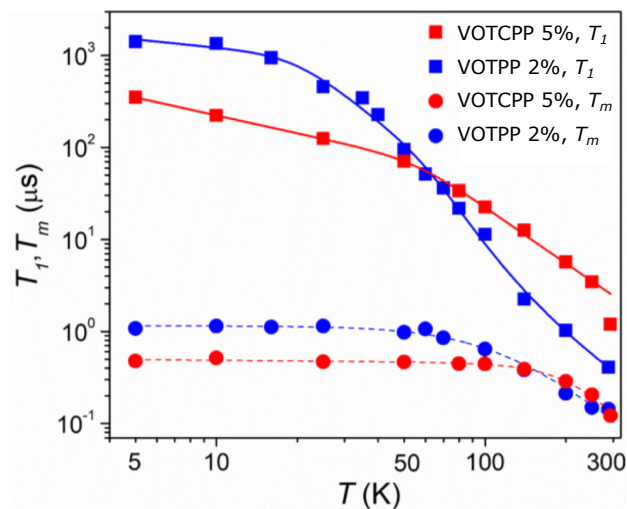


**Figure 9.26:** Temperature dependence of  $T_1$  and  $T_m$  for **VOTCPP 5%** and **VOTPP 2%** from pulsed EPR inversion recovery experiments at X-band frequency (9.7 GHz).

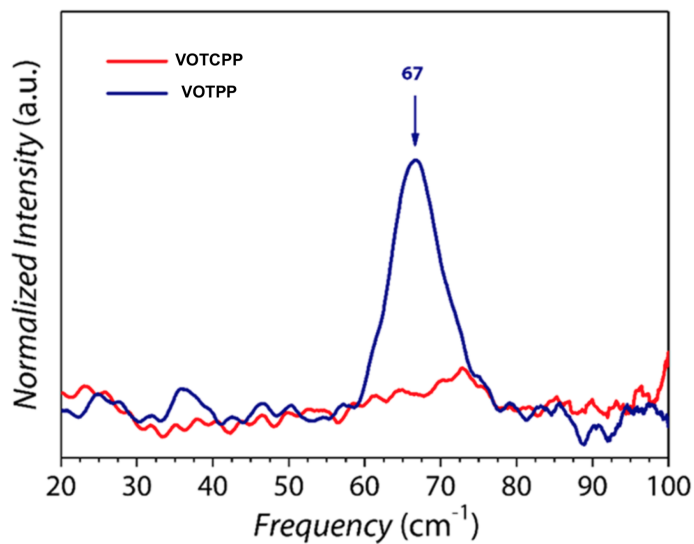


**Figure 9.27:** THz spectra in the  $20\text{-}100\text{ cm}^{-1}$  (0.6-3.0 THz) of **VOTCPP** and **VOTPP** recorded at 295 K. The arrow indicates the frequency of the absorption line.



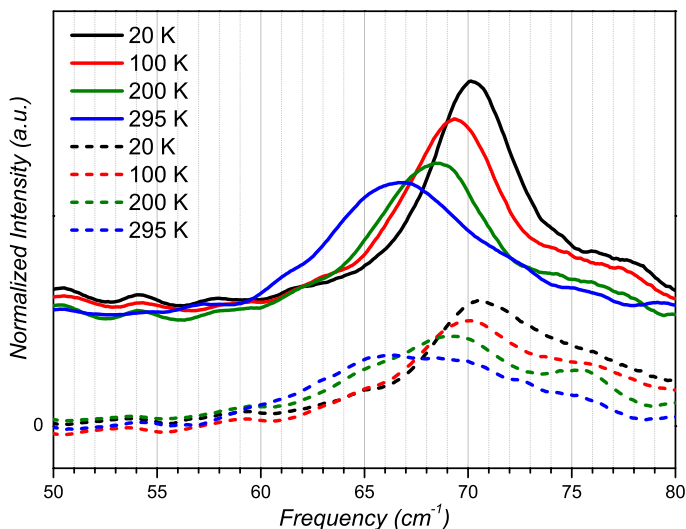


**Figure 9.28:** THz spectra in the 10-110  $\text{cm}^{-1}$  range of **VOTPP** (solid lines) and **TiOTPP** (dashed lines) at different temperatures.

Assignment of the low-energy absorption of **VOTPP** is not straightforward because porphyrinate complexes show metal-ligand vibrations that are often mixed with porphyrin ring deformations[18][19]. Moreover, in the Terahertz frequency range, a strong admixing between local and collective degrees of freedom is present[5], as already mentioned in chapter 9.1 for  $\text{VO}(\text{acac})_2$ . Spectra of **VOTPP** and **TiOTPP** at different temperatures are shown in Figure 9.28. The temperature dependence of the unique vibrational mode of **VOTPP** and **TiOTPP** in the investigated frequency window is shown in Figure 9.29. On lowering the temperature, both the bands have a pronounced narrowing and they shift to higher frequency. The slightly difference of the central frequency of the absorption bands for the vanadyl and titanyl complexes is due to the different atomic mass of the metal. According to the idea that structure stiffening at low temperature is expected to increase the vibration energy of collective modes, we can deduce that a significant contribution of collective vibrations to the nature of this mode is present. This is also in agreement with the lack of this mode in the covalent lattice of **VOTCPP**, as well as its similar frequency in the titanyl analogue.

#### 9.4.4 Conclusions

The different phonons structure of the MOF with respect to its representative molecular building block originates remarkable differences in the temperature de-

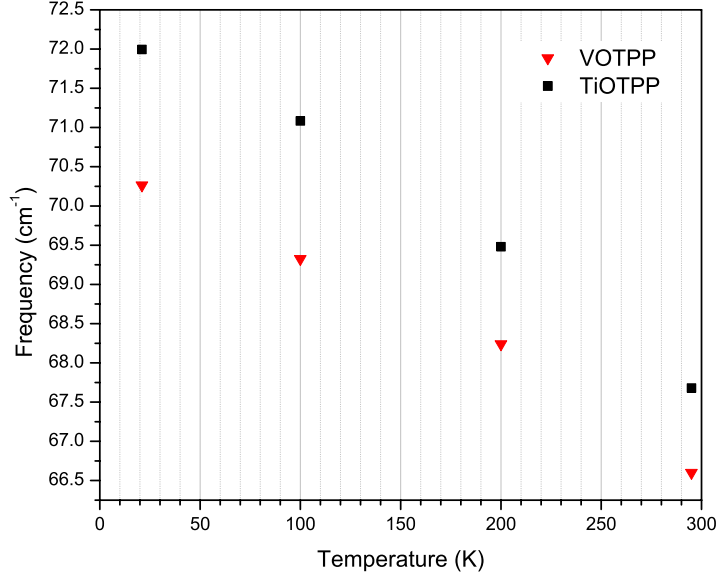


**Figure 9.29:** Temperature dependence of the unique absorption band's frequency for **VOTPP** and **TiOTPP**.

pendence of  $T_1$  above 30 K. The temperature dependence of the spin-lattice dynamics can be successfully reproduced through the phenomenological model[20]:

$$T_1^{-1} = a_{dir}T^x + a_{loc} \frac{\exp(\hbar\omega/k_B T)}{(\exp(\hbar\omega/k_B T) - 1)^2} \quad (9.11)$$

where  $\omega$  is the frequency of the vibrational mode and  $a_{dir}$  and  $a_{loc}$  are coupling coefficients. The  $T_1$  data of **VOTCPP** are successfully simulated with  $x = 0.64$  and  $\omega = 184 \text{ cm}^{-1}$ , thus suggesting that the first active mode occurs at a frequency higher than our accessible spectral range. Data simulation of **VOTPP** was performed by fixing the frequency of the vibration mode to  $67 \text{ cm}^{-1}$ , accordingly to spectroscopic findings. The whole temperature range is well reproduced when including a second mode at higher frequency,  $303 \text{ cm}^{-1}$ , to the model. This is reasonable because an increasing number of active vibrational modes are expected to be present at higher frequencies. In conclusion, arranging vanadyl spin units in a 3D covalent network allows to retain spin coherence up to room temperature. Surprisingly, it does not affected the low-temperature regime and the  $n < 1$  exponent in the  $T_1 \propto T^{-n}$  power law seems rather typical of the rigidity of the tetraphenylporphyrin coordination environment. On the contrary, linking the vanadyl units in the 3D network has pronounced effects on the temperature dependence of  $T_1$  in the intermediate temperature regime.

## 9.5 Summary

A series of vanadyl- and vanadium-based molecules has been investigated here through a multi-technique approach constituted of cw-EPR, AC susceptometry, THz-TD spectroscopy and pulsed EPR. This investigation has been firstly focused on the structural properties of these systems, whose magnetic properties are accounted for by an electronic spin  $S = 1/2$  coupled with a nuclear spin  $I = 7/2$  for weak magnetic fields. Indeed, at high magnetic fields the spin system can be described simply as a two-levels system. These features are common to all the investigated molecules. Vanadyl and tris-chelate molecules can be differentiated on the basis of their ground electronic state that is a well-isolated  $d_{xy}$  orbital for the former and a more mixed  $d_{z^2}$  orbital for the latter. This is reflected in the magnetization dynamics that shows longer relaxation times,  $\tau$ , for the vanadyl species, both as a function of temperature and magnetic field. Such relaxation times were extracted by AC susceptibility measurements performed on pure microcrystalline compounds within 2 and 70 K, and they are of the order of milliseconds. The behaviour of the thermal variation of  $\tau$  can be explained by taking into account two relaxation processes: the direct at low temperatures and the Raman at higher temperature. A more detailed analysis focused on the temperature dependence of  $T_1$  allowed to relate the spin dynamics features with the experimental low-energy vibrational modes, i.e. between 10-150  $\text{cm}^{-1}$ . Indeed, it has been found that molecules with few vibrational modes and mainly located at high frequencies exhibit relaxation times with weaker temperature dependence. In addition, from this analysis it has emerged that the efficiency of the vibrational modes is not only related to its energy, and it is not surprising that the phonon most active in inducing spin relaxation does not correspond to the lowest one. Indeed, such efficiency is a combination of the thermal population of the vibrational mode and the spin-phonon coupling. In this frame, a more accurate model should not be limited to the vibrational modes at the  $\Gamma$ -point of the Brillouin zone, and it should consider the spin-phonon coupling of each vibrational mode. This type of investigation can be done only by using an *ab initio* approach and, nevertheless its complexity, it is now in progress and the earlier results are described in chapter 9.3.

Additional evidences about the role of the low-energy vibrational modes in the spin-lattice relaxation can be achieved by comparing the results obtained by the magnetic analysis of the magnetic field dependence of  $\tau$ , extracted by AC susceptometry, with the THz spectroscopy findings. It should be remarked that the possibility to perform measurements of the relaxation time as a function of the magnetic field is one of the great advantages of AC susceptometry. From these measurements it has been evidenced a non-monotonous behaviour shared

CHAPTER 9. THz spectroscopy as innovative probe of the molecular Qubits performance

by all the Vanadium(IV)-based molecules investigated. This originates from the competition between the internal contributions, such as dipolar fields produced by spin-spin and spin-nuclei interactions, and the direct process. Moreover, though the entire temperature dependence of  $\tau$  does not vary following an Arrhenius-like behaviour, this type of dependence applies for some parameters extracted by fitting the magnetic field dependence of  $\tau$  with the Brons-van Vleck model. From the analysis of their temperature dependence, indeed, it is possible to extract an effective activation energy,  $U_{eff}$ . Interestingly, the  $U_{eff}$  values extracted seem to well correlate with some of the low-energy vibrational modes experimentally observed, when the relation  $U_{eff} = \hbar\omega_\alpha/2$  is taken into account. This relation has been theoretically derived to explain the spin-lattice relaxation for Single-Molecule Magnets when the anharmonicity of phonons is not neglected.

The phonons structure investigation as function of temperature, even if related only to the  $\Gamma$ -point of the Brillouin zone, can shed light on several aspects such as the deformation of the unit cell by varying the temperature. Moreover, it offers a crucial validation for the extracted activation barriers related to the spin-lattice relaxation pathways as well as for the *ab initio* calculations. Indeed, theoretical calculations of low energy phonons are not trivial and are often affected by significant errors. It is worth noting that the possibility to acquire far-IR vibrational spectra with such high signal to noise ratio is one of the great advantages of THz-TD spectroscopy. Once more, these results evidence the involvement of phonons in determining the behavior of the spin-lattice relaxation time, highlighting the fundamental role of a spectroscopic investigation to obtain a full description of the systems.

## Chapter 10

# Spin dynamics under THz irradiation

This chapter is devoted to the investigation of how the THz radiation, produced by FEL, affects the spin dynamics of **VOTPP**. This compound (see chapter 9.4) has been chosen because of its peculiar low-energy vibration spectrum which shows a single IR-active phonon below  $100\text{ cm}^{-1}$  ( $67\text{ cm}^{-1}$  at 300 K). This, indeed, makes it suitable for such study cause it allows to test the system response at different THz irradiation wavelengths, e.g. on resonance with the phonon band or not, on the band central frequency as well as on its edge, being sure to not perturb any other vibrational modes. The latter is a crucial point, otherwise it would be impossible to discern the origin of any effect. In this framework, a system having a well-isolated and separated phonon is the best candidate. Moreover, the **VOTPP** shows remarkably long spin-lattice and phase memory times, that allows to perform EPR measurements in a wide range of temperatures. The idea behind this experiment is to directly observe the influence of the phonons on the spin relaxation mechanisms, confirming, in a certain sense, the work summarized in the previous chapters. The study has been mainly performed during two stays of one month each at the International Tomography Center and the Free Electron Laser facility of Novosibirsk. Indeed, for the best of our knowledge, the latter provides the unique laboratory with a EPR spectrometer coupled with a Free Electron Laser able to produce high-power radiation in THz regime. During these periods, it has begun a fruitful collaboration with Prof. Matvey Fedin, Sergey Veber and Anatoly Melnikov. The chapter is organized according to each experiment: in the first two sections, some preliminary measurements are reported, such as pulse and CW-EPR investigation. The following sections contain the results of the Time-resolved THz EPR experiments (TR-THz-EPR)

as function of MW power, temperature, frequency and power of the THz radiation. The last section is focused on the simulation of the experimental data by a simple model based on a modified version of Bloch equations.

## 10.1 Pulse EPR investigation

In this section the reader will find the information about the temperature and the magnetic field dependence of the spin-lattice relaxation time,  $T_1$ , and of the phase-memory time,  $T_m$ , which is a good approximation of the spin-spin relaxation time,  $T_2$ , obtained by pulsed EPR measurements on microcrystalline powders.  $T_1$  has been, firstly, measured at 7 and 70 K in a wide magnetic field range (280-440 mT) by Inversion Recovery pulse sequence. The spin-lattice relaxation time has been obtained by a double exponential decay fitting of the signal. Also, a comparative extrapolation with a single exponential decay has been performed. Moreover,  $T_1$  has been investigated as a function of temperature in the 5-125 K range at the magnetic field value corresponding to the maximum of the signal. The  $T_m$  has been measured at 7 and 70 K in the 280-440 mT magnetic field range by Electron Spin Echo Envelope Modulation (ESEEM) protocol. The phase-memory time has been obtained, in analogy with the  $T_1$ , by both a double and single exponential decay fitting of the signal.

### 10.1.1 $T_1$ measurements at 7 and 70 K in a wide magnetic field range

The spin-lattice relaxation time of **VOTPP 2%** has been measured at 7 and 70 K in the 280-440 mT magnetic field window by Inversion Recovery sequence. The results are summarized in table 10.1.

#### Analysis with a double-exponential fitting

The  $T_1$  values have been extracted by a double exponential decay fitting (Figure 10.3 and 10.6):

$$S(t) = Ae^{-t/T_1^a} + Be^{-t/T_1^b} + BL \quad (10.1)$$

in which  $A$  and  $B$  are the exponential amplitudes,  $T_1^a$  and  $T_1^b$  the decay constants and  $BL$  represents the base line correction.

The  $T_1^a$  and  $T_1^b$ , as well as the  $A$  and  $B$  magnetic field dependence obtained by the least-square fitting with the equation 10.1 of the data at 7 K is shown in Figure 10.1 and 10.2, respectively. The characteristic times  $T_1^a$  and  $T_1^b$  at the

maximum of the signal (345.6 mT) are equal to 1.84 and 9.87 ms, respectively (Figure 10.3).

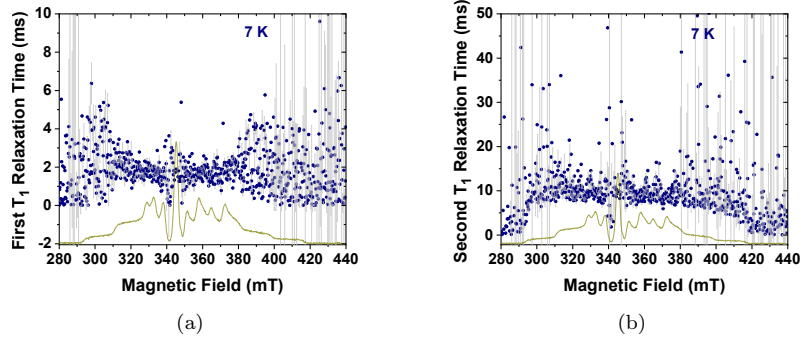


**Figure 10.1:**  $T_1$  relaxation time as a function of magnetic field. Experimental data was measured at 7 K by Inversion Recovery and fitted by two exponential decay function. Gray lines represent the standard deviations of obtained parameters of the fits. Inversion-recovery absorption spectrum is shown by green line. Panel (a) shows the values of  $T_1^a$  (ca. 1.5 ms), while panel (b) of  $T_1^b$  (ca. 9 ms).

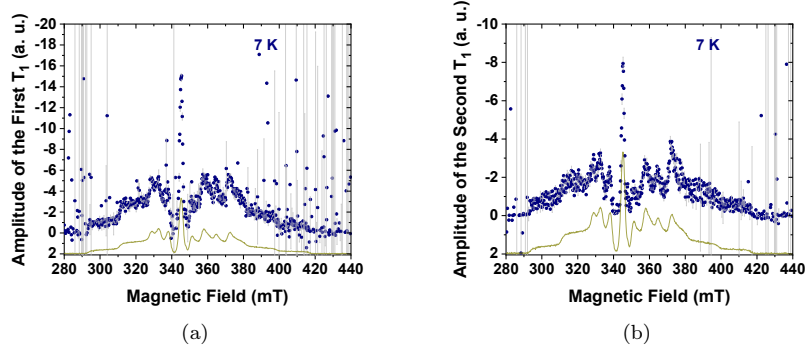


**Figure 10.2:** Amplitudes  $A$  (a) and  $B$  (b) of exponents as a function of magnetic field. Gray lines represent the standard deviations of obtained parameters of the fits. Inversion-recovery absorption spectrum is shown by green line.

While those at 70 K are shown in Figure 10.4 and Figure 10.5. The characteristic times  $T_1^a$  and  $T_1^b$  at the maximum of the signal (345.6 mT) are equal to 18.1 and 67.1  $\mu\text{s}$ , respectively (Figure 10.6).

### Analysis with a single-exponential fitting

The same data analysis of the Inversion Recovery data has been also carried out by using a single exponential decay fit function (equation 10.2) in order to

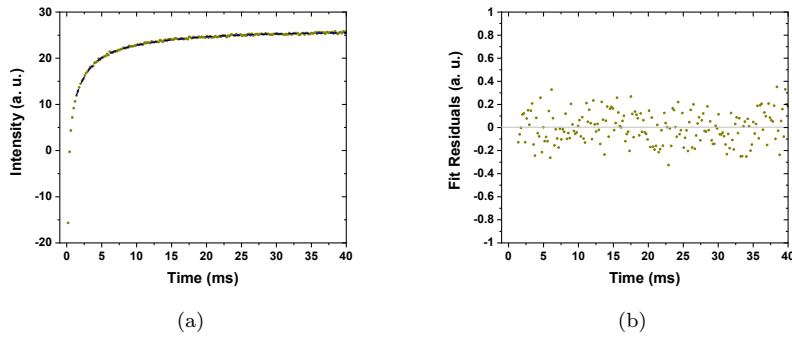


**Figure 10.3:** (a) Inversion recovery kinetics at 7 K and magnetic field of 345.6 mT (green dots) and the best double exponential fit of experimental data (dashed dark blue line). Characteristic times are equal to 1.84 and 9.87 ms. (b) Residuals of the fit.

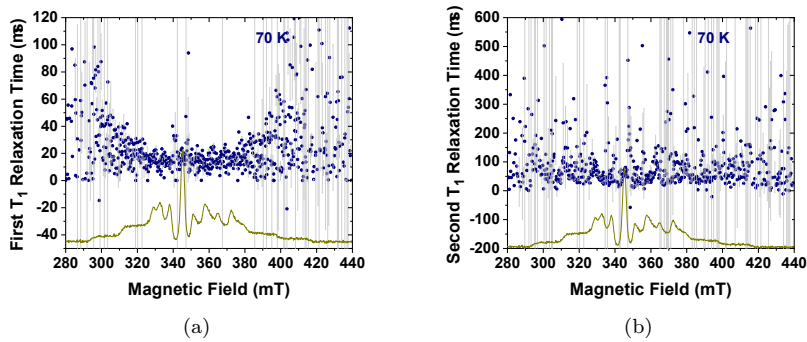


**Figure 10.4:**  $T_1$  relaxation time as a function of magnetic field. Experimental data was measured at 70 K by Inversion Recovery and fitted by the double exponential decay function. Gray lines represent the standard deviations of obtained parameters of the fits. Inversion-recovery absorption spectrum is shown by green line. Panel (a) shows the values of  $T_1^a$  (ca. 18.1  $\mu$ s), while panel (b) of  $T_1^b$  (ca. 67.1  $\mu$ s).



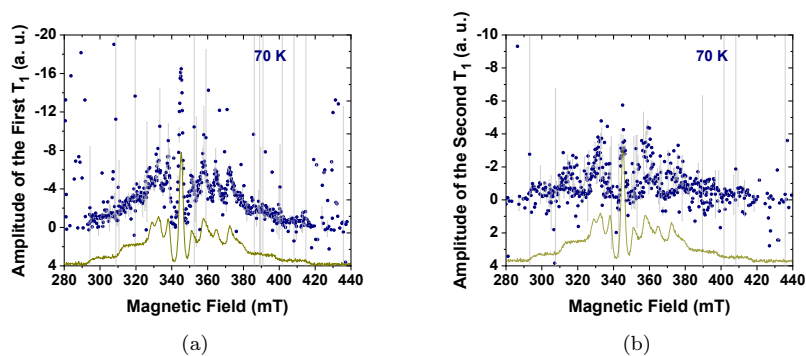


**Figure 10.5:** Amplitudes  $A$  (a) and  $B$  (b) of exponents as a function of magnetic field. Gray lines represent the standard deviations of obtained parameters of the fits. Inversion-recovery absorption spectrum is shown by green line.

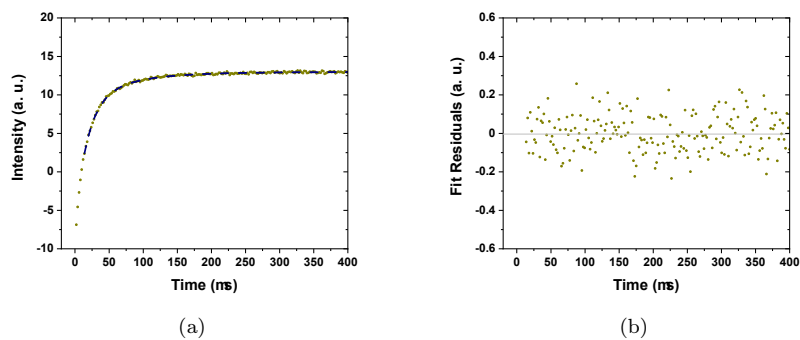


**Figure 10.6:** (a) Inversion recovery kinetics at 70 K and magnetic field of 345.6 mT (green dots) and the best two exponential fit of experimental data (dashed dark blue line). Characteristic times are equal to 18.1 and 67.1  $\mu\text{s}$ . (b) Residuals of the fit.

compare the quality of the fit.

$$S(t) = Ae^{-t/T_1} + BL \quad (10.2)$$

The results at 7 K are shown in Figure 10.7 and 10.8. The  $T_1$  value is equal to 4.87 ms.

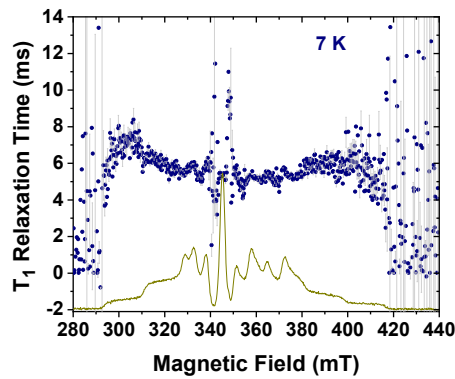


**Figure 10.7:**  $T_1$  relaxation time as a function of magnetic field. Experimental data was measured at 7 K by inversion recovery fitted by one exponent with characteristic time of about 5.5 ms. Gray lines represent the standard deviations of obtained parameters of the fits. Inversion-recovery absorption spectrum is shown by green line.

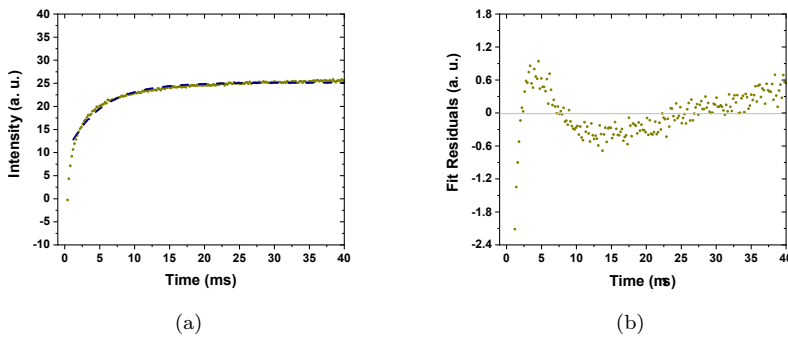


**Figure 10.8:** (a) Inversion recovery kinetics at 7 K and magnetic field of 345.6 mT (green dots) and the best single exponential fit of experimental data (dashed dark blue line). The characteristic time is equal to 4.87 ms. (b) Residuals of the fit.

The results at 70 K are shown in Figure 10.9 and 10.10. The  $T_1$  value is equal to 31.1  $\mu$ s.

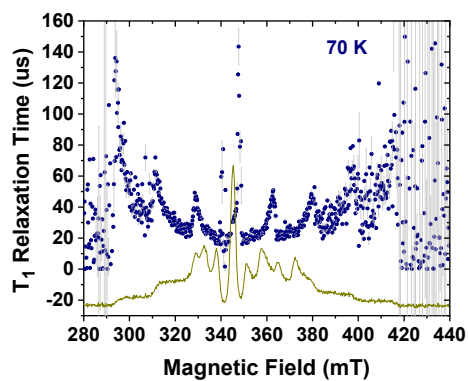


**Figure 10.9:**  $T_1$  relaxation time as a function of magnetic field. Experimental data was measured at 70 K by inversion recovery fitted by one exponent with characteristic time of about  $35 \mu\text{s}$ . Gray lines represent the standard deviations of obtained parameters of the fits. Inversion-recovery absorption spectrum is shown by green line.

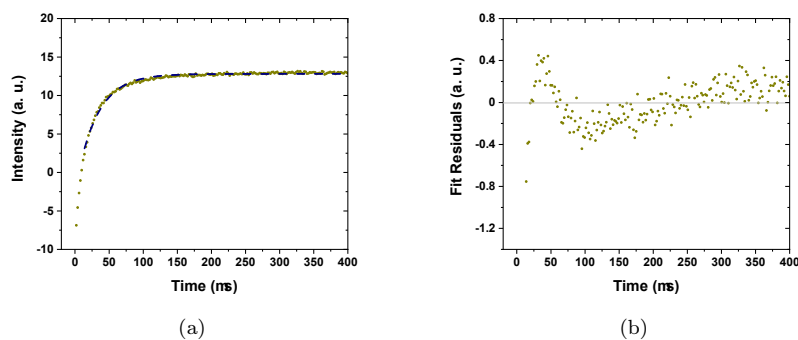


**Figure 10.10:** (a) Inversion recovery kinetics at 70 K and magnetic field of 345.6 mT (green dots) and the best single exponential fit of experimental data (dashed dark blue line). The characteristic time is equal to  $31.1 \mu\text{s}$ . (b) Residuals of the fit.

Temperature (K)	Double exponential fit		Single exponential fit
	$T_1^a$	$T_1^b$	$T_1$
7	1.84 ms	9.87 ms	4.87 ms
70	$18.1 \mu\text{s}$	$67.1 \mu\text{s}$	$31.1 \mu\text{s}$

**Table 10.1:** Characteristic times extrapolated by the analysis of Inversion Recovery data at 7 and 70 K.

### 10.1.2 Temperature dependence of $T_1$

The temperature dependence of  $T_1$  in the range of 5–125 K has been also measured. It was done using Inversion Recovery protocol at the magnetic field corresponding to the maximum of signal (345.1 mT at 9.746 GHz). Since the experimental kinetics is not perfectly reproduced by a single exponential function, the fit has been also performed using the three exponential fit function (10.3), which perfectly reproduce the trend. The choice of the fit function (10.3), instead of a double exponential decay as in previous sections, is required for the simulation discussed in section 10.8.

$$S(t) = Ae^{-t/T_1^a} + Be^{-t/T_1^b} + Ce^{-t/T_1^c} + BL \quad (10.3)$$

Typical examples of fittings are given in Figure 10.11 and 10.12.

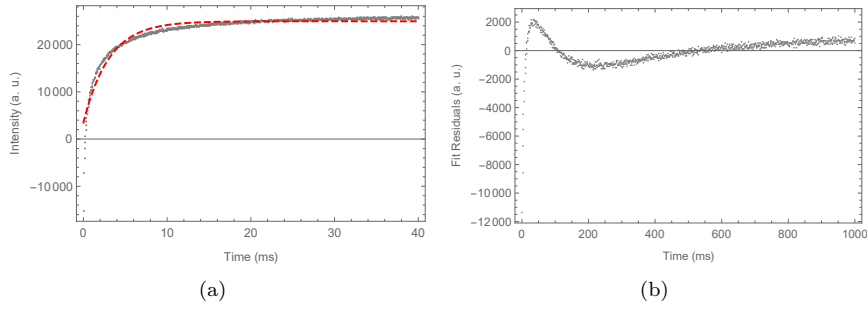


**Figure 10.11:** (a) Examples of inversion recovery kinetics (gray dots) at 7 K and its one exponential fitting (dashed red line). (b) Residuals of the fit.

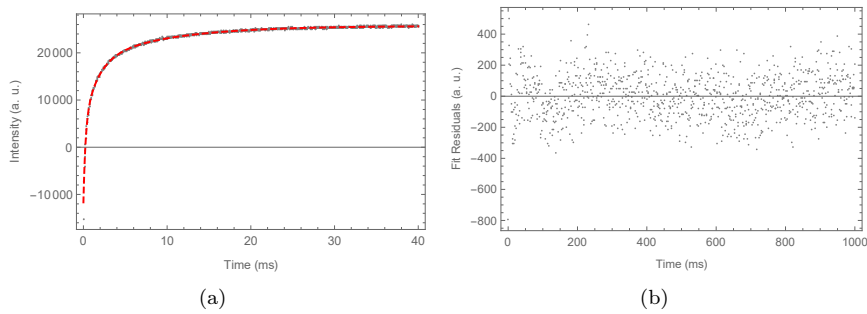


**Figure 10.12:** (a) Examples of inversion recovery kinetics (gray dots) at 70 K and its three exponential fitting (dashed red line). (b) Residuals of the fit.

Figure 10.13 shows the temperature dependence of the spin-lattice relaxation time whether it is equal to the longest of the three exponential decay times or equal to the decay time of the single exponential fit.

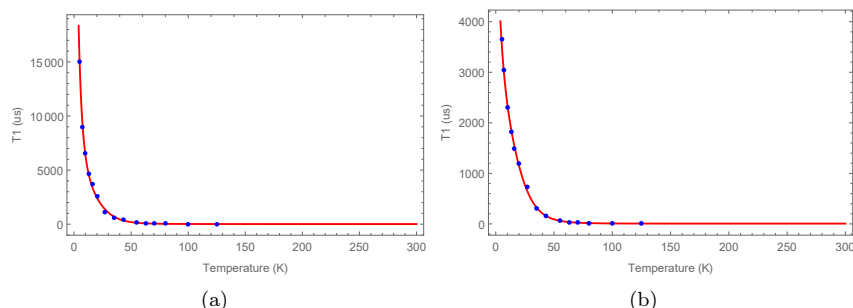


**Figure 10.13:**  $T_1$  as function of temperature obtained using the longest relaxation time from three exponential fit (a) and from single exponential fit (b). Blue dots show the experimental  $T_1$  values, and the red line the best-fit.

In section 10.8, these two types of fitting will be used for two sets of simulation. The use of one “averaged” exponent helps to take into account, to some extent, the presence of **VOTPP** molecules with different relaxation time. On the contrary, the use of the longest  $T_1$  from the three exponential fitting helps to elucidate the impact of long relaxation time on the amplitude of the effect.

### 10.1.3 $T_2$ measurements at 7 and 70 K

The spin-spin relaxation time of **VOTPP 2%** has been measured at 7 and 70 K in the 280-440 mT magnetic field window by Electron Spin Echo Envelope Modulation (ESEEM) sequence. The  $T_2$  values have been extracted by a single exponential decay fitting:

$$S(t) = Ae^{-t/T_2} + BL \quad (10.4)$$

where  $T_2$  represents the spin-spin relaxation time.

The  $T_2$  as function of the magnetic field resulting from the least-square fitting with the equation 10.4 of the data at 7 K is shown in Figure 10.14 and 10.15. The characteristic time  $T_2$  at the maximum of the signal (345.6 mT) is equal to 0.32  $\mu\text{s}$ .

The results at 70 K are shown in Figure 10.16 and 10.17. The characteristic time  $T_2$  at the maximum of the signal (345.6 mT) is equal to 0.24  $\mu\text{s}$ .

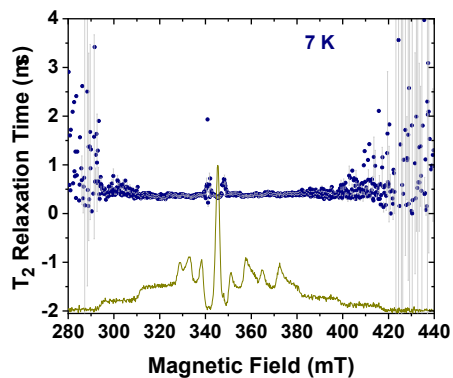


**Figure 10.14:**  $T_2$  relaxation time as a function of magnetic field. Experimental data was measured at 7 K by ESEEM and fitted by one exponent with characteristic time of about  $0.4 \mu\text{s}$ . Gray lines represent the standard deviations of obtained parameters of the fits. ESEEM absorption spectrum is shown by green line.

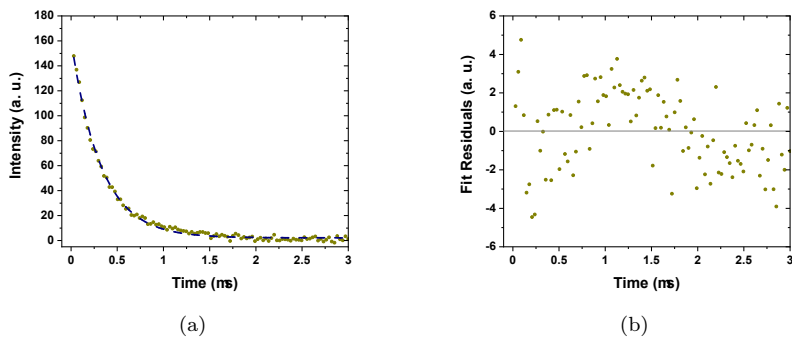


**Figure 10.15:** (a) ESEEM kinetics at 7 K and magnetic field of 345.6 mT (green dots) and the best single exponential fit of experimental data (dashed dark blue line). The characteristic time is equal to  $0.32 \mu\text{s}$ . (b) Residuals of the fit.

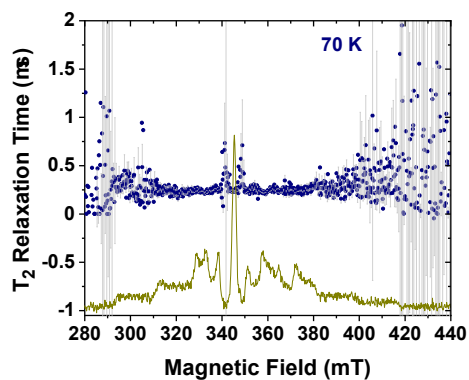


**Figure 10.16:**  $T_2$  relaxation time as a function of magnetic field. Experimental data was measured at 70 K by ESEEM and fitted by one exponent with characteristic time of about  $0.3 \mu\text{s}$ . Gray lines represent the standard deviations of obtained parameters of the fits. ESEEM absorption spectrum is shown by green line.

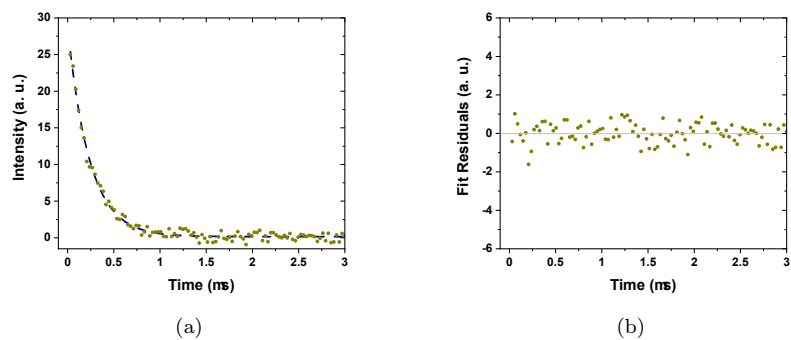


**Figure 10.17:** (a) ESEEM kinetics at 70 K and magnetic field of 345.6 mT (green dots) and the best single exponential fit of experimental data (dashed dark blue line). The characteristic time is equal to  $0.24 \mu\text{s}$ . (b) Residuals of the fit.

## 10.2 CW-EPR measurements

A standard investigation of the spin dynamics by CW-EPR aims to obtain the saturation curves, i.e. the intensity of the central line of the **VOTPP 2%** CW-EPR spectrum as function of the microwave (MW) power, in order to know at which MW power the sample approaches the saturation. Such information is, indeed, crucial in the interpretation of the TR-THz-EPR measurements.

### 10.2.1 Saturation curves of VOTPP 2%

The CW-EPR spectra of **VOTPP 2%** in X-band measured at different temperatures and MW power are shown in Figure 10.18.

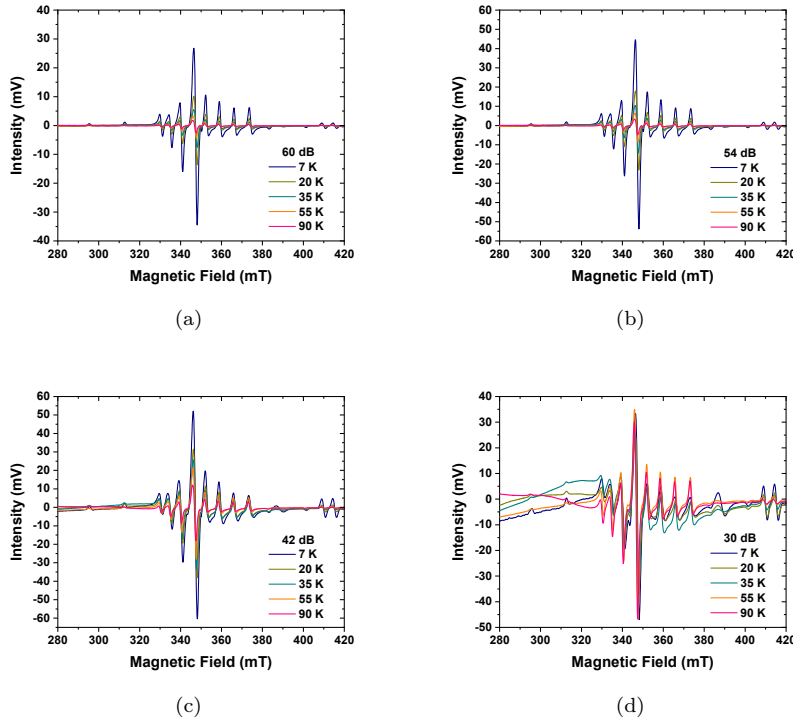


**Figure 10.18:** CW-EPR spectra of **VOTPP 2%** at different temperature in the range of 7–90 K. The MW frequency is 9.760 GHz, the modulation frequency is 100 kHz, the modulation amplitude is 1.3 G, the time constant is 30 ms. The MW power is  $0.2 \mu\text{W}$  (60 dB) (panel (a)),  $0.8 \mu\text{W}$  (54 dB) (panel (b)),  $12.8 \mu\text{W}$  (42 dB) (panel (c)),  $204.8 \mu\text{W}$  (30 dB) (panel (d)).

The corresponding saturation curves have been obtained by measuring the peak-to-peak signal intensity of the central line as function of the MW power, at different temperatures (Figure 10.19).



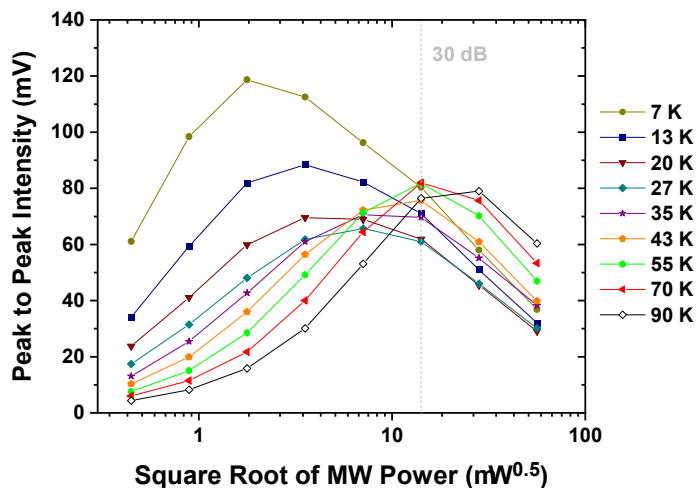


**Figure 10.19:** Saturation curves at different temperatures in the range of 7–90 K. The square root of MW power corresponds to attenuation in the range of 60–18 dB with steps of 6 dB. 60 dB corresponds to  $0.2 \mu\text{W}$  of MW power. The MW frequency is 9.760 GHz, the modulation frequency is 100 kHz, the modulation amplitude is 1.3 G, the time constant is 30 ms.

As expected from pulsed EPR data in section 10.1, the EPR signal of **VOTPP 2%** can be easily saturated. At 20 K and ca. 40 dB (ca.  $20 \mu\text{W}$ ), the signal reaches its maximum intensity and starts to decrease when MW power is further increased. In Figure 10.20, it is shown the comparison between the EPR signal intensities for the **VOTPP 2%** central line and an example of non-saturated signal, as function of the square root of microwave power. Saturation measurements allow to make a rough estimation of the “spin system temperature” at different MW power, according to equation 10.5:

$$T_{spin} = T_{cryostat} \frac{I_{NS}}{I_s} \quad (10.5)$$

where  $T_{cryostat}$  is the temperature of the environment in which the sample is placed,  $I_{NS}$  the intensity of the non-saturated signal and  $I_s$  the intensity of the EPR signal of the sample at that MW power. The estimation of the spin temperature is shown in Figure 10.21.

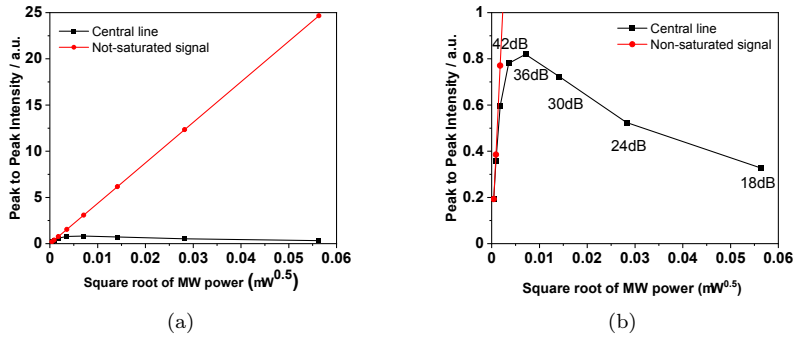


**Figure 10.20:** Different behavior of the CW-EPR signal intensity in case of easily saturable (black line) and not saturable (red line) spin system. Panel (b) shows a zoom of panel (a) in the 0-1 peak to peak intensity.

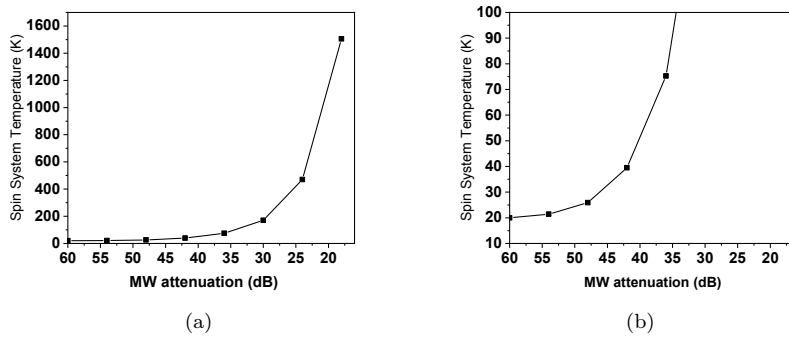


**Figure 10.21:** Estimation of the spin temperature as function of the MW power according to the simple model of equation 10.5. Panel (b) shows a zoom of panel (a) in the 10-100 K.

### 10.2.2 Estimation of the sample T-jump

Intense THz radiation substantially heats the sample and increases its real temperature. The estimation of the temperature jump experienced by the sample can be done comparing the saturation curves under THz irradiation with those obtained in the previous section. The THz macropulses used in the experiment have a duration of 50 and 60  $\mu\text{s}$ , respectively, at 400 Hz rep. rate (Figure 10.22). The central frequency is  $71.4\text{ cm}^{-1}$  ( $140.1\ \mu\text{m}$ ), as shown in the spectrum (Figure 10.23). Such a high rep. is necessary to the lock-in detection of CW-EPR spectra modulated by THz pulses.

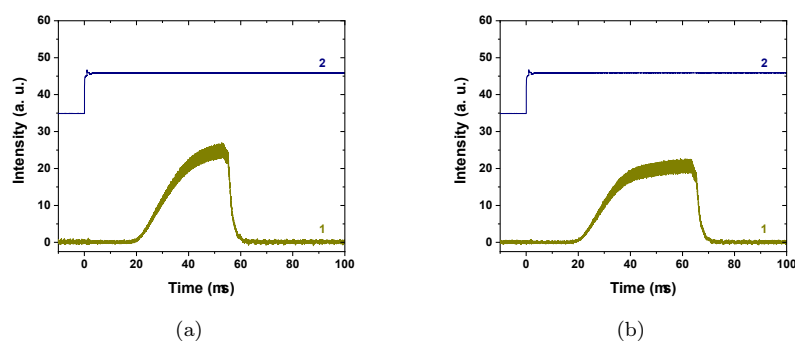


**Figure 10.22:** THz macropulse of 50  $\mu\text{s}$  (a) and 60  $\mu\text{s}$  (b) used in the experiments. (1) is THz macropulse measured by Gentec fast pyroelectric detector QS5-IF; (2) is the trigger signal for electronic modulation system of NovoFEL.

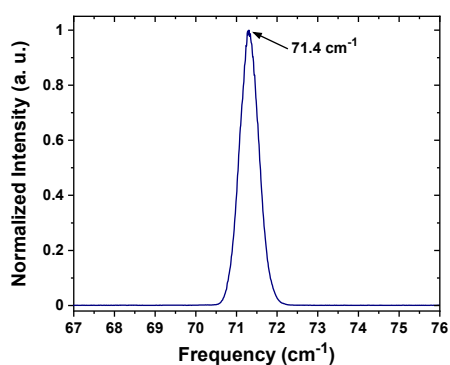


**Figure 10.23:** Spectrum of THz radiation used in the CW-EPR experiments under THz irradiation.

The procedure consists in acquiring the THz-CW-EPR spectrum in lock-in detection mode: by varying the THz pulse duration, the THz power is adjusted

to produce a central line peak-to-peak intensity, measured at 60 dB ( $0.2 \mu\text{W}$  MW power) and 13 K, which exactly matches that of a signal measured without THz radiation at higher temperature at the same MW power. It results in a T-jump values of 14 and 22 K for a THz macropulses of, respectively,  $50 \mu\text{s}$  and  $60 \mu\text{s}$  at 400 Hz rep. rate (Figure 10.24). The time constant in these experiments has been set at 30 ms, which means that approximately 12 THz pulses are integrated over the time constant of the lock-in detection.

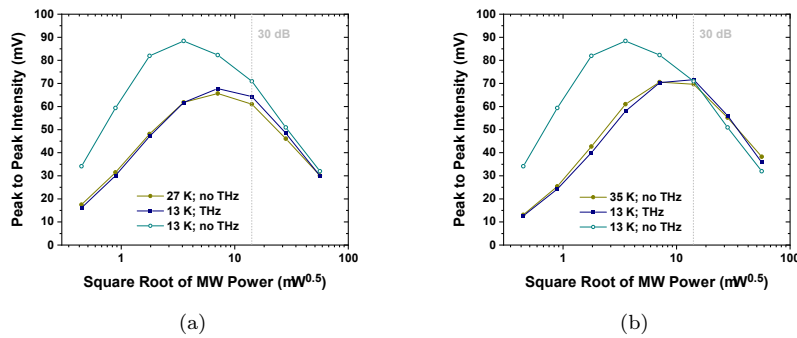


**Figure 10.24:** (a) Comparison of saturation curves at 13 K (dark grey) and 27 K (dark green) and that measured under THz irradiation at 13 K (dark blue). The real sample temperature under THz radiation is 27 K (estimated at 60 dB) when the sample is irradiated by THz macropulses of  $50 \mu\text{s}$ . (b) Comparison of saturation curves at 13 K (dark grey) and 35 K (dark green) and that measured under THz irradiation at 13 K (dark blue). The real sample temperature under THz radiation is 35 K (estimated at 60 dB) when the sample is irradiated by THz macropulses of  $60 \mu\text{s}$ . Square root of MW power corresponds to attenuation in the range of 60–18 dB with steps of 6 dB. 60 dB attenuation corresponds to  $0.2 \mu\text{W}$  of MW power. The MW frequency is 9.760 GHz, the modulation frequency is 100 kHz, the modulation amplitude is 1.3 G, the time constant is 30 ms, the THz repetition rate is 400 Hz.

### 10.3 2D-THz-EPR experiments

The 2D-THz-EPR experiment reveals a 2D map in which the x- and y-axes represent, respectively, the time evolution of the transient signal and the magnetic field at which the transient signal is acquired (Figure 10.25).

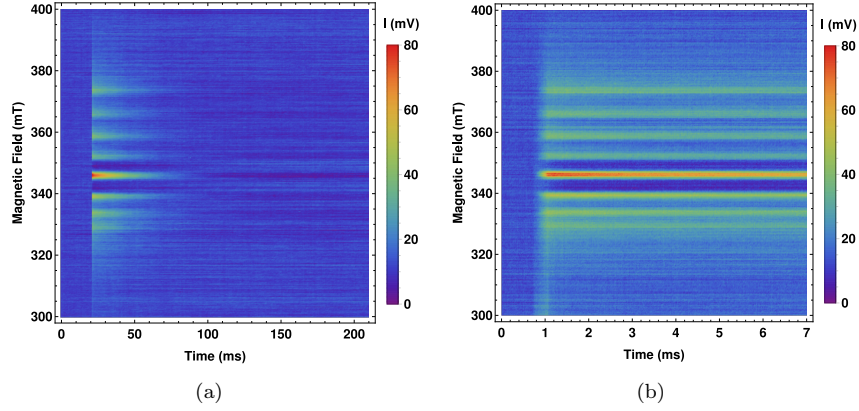


**Figure 10.25:** (a) Detailed 2D-THz-EPR spectrum of **VOTPP 2%** measured at 20 K. MW frequency is 9.758 GHz, MW power is  $200 \mu\text{W}$ , THz radiation pulse length is  $350 \mu\text{s}$ , rep. rate is 1.8 Hz. (b) Zoom of the 2D-THz-EPR spectrum at shorter times.

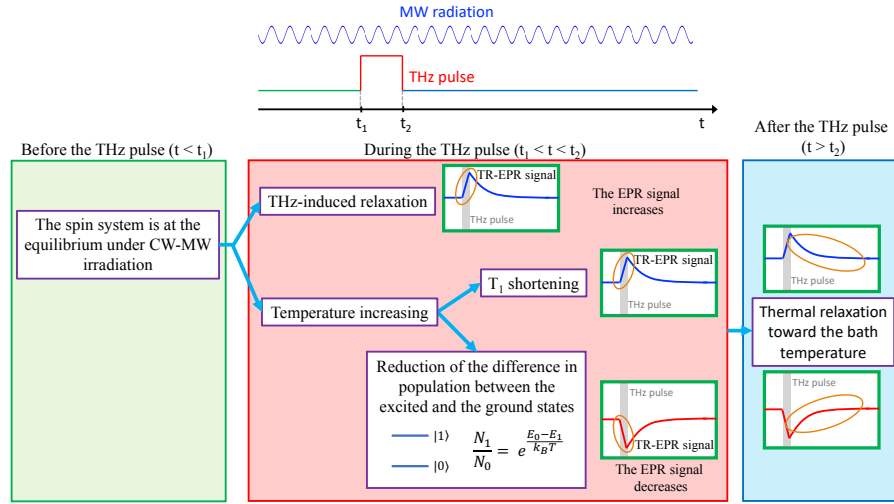


**Figure 10.26:** (top) Sketch of the irradiation sequence. The sample is continuously irradiated by the MW resulting in a certain value of the CW-EPR signal intensity. At  $t_1 < t < t_2$ , the THz pulse irradiates the sample causing the three phenomena schematically represented below. (bottom) Situations experienced by the sample during the three time-lapses: before, during and after the THz irradiation.

After a proper delay time ( $t_1$  in Figure 10.26), the THz macropulse irradiates

## CHAPTER 10. Spin dynamics under THz irradiation

and perturbs the sample moving it away from its equilibrium condition. The transient signal, hereafter called kinetics, is originated from the changing in the CW-EPR spectrum intensity. This is due to three effects (Figure 10.26) that are listed below:

1. the heating of the sample, which depends on the THz pulse-length and on the THz power. The temperature jump makes the spin population change its distribution between the two levels, according to the Boltzmann factor. It results in a reduction of the difference in population between the excited and the ground states causing the decrease of the CW-EPR signal intensity and the drop of the TR-EPR one;
2. the shortening of  $T_1$  during the T-jump, according to its temperature dependence. This causes a higher spin relaxation rate promoting the fast increase in population difference between the two spin states. It results in an increment of the CW-EPR signal intensity and in the rise of the TR-EPR one;
3. the THz-induced spin relaxation that further boosts the difference in the spin population between the two levels. This also produces a TR-EPR signal rise, similarly to the  $T_1$  shortening.

The relative contribution of these phenomena depends mainly on whether the spin system is saturated or not and it will be exhaustively discussed section 10.4. It is worth noting that fine structure of the THz macropulse emitted by the FEL it is not considered in this work since the spin is not sensitive to it. Indeed, the spin system can experience perturbations which develop on long timescales, approximately having the same order of magnitude of the spin dynamics or longer (from few  $\mu\text{s}$  up). Conversely, the spin can only feel an average effect of the perturbation.

After the THz perturbation, the thermal relaxation of the sample occurs restoring the initial Boltzmann distribution. This promotes the slow return of the TR-EPR signal to its initial value.

To acquire the 2D-THz-EPR map, it is used a THz pulse of 350  $\mu\text{s}$  with central frequency of  $71.4 \text{ cm}^{-1}$  (Figure 10.27) at a 1.8 Hz rep. rate with an average power per single pulse of 112 W. The repetition rate is set by the time needed to the sample to relax back to its equilibrium temperature. Indeed, the highest achievable rep. rate is that at which the transient signal is independent from the rep. rate value.

A vertical cut of the 2D map reveals the cross-section of the 2D-spectrum that strongly resembles to the “integrated” CW-EPR spectrum. Indeed, the map is built acquiring a kinetic curve at each magnetic field value, therefore the

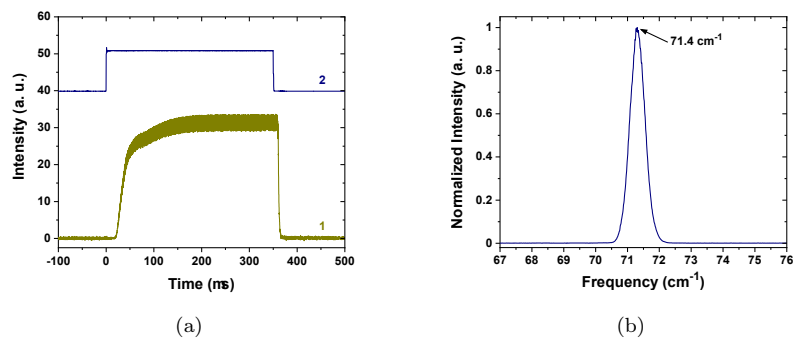


**Figure 10.27:** (a) THz macropulse with 350  $\mu\text{s}$  duration measured by Gentec fast pyroelectric detector QS5-IF (1) and trigger signal for electronic modulation system of NovoFEL (2). (b) Spectrum of the THz macropulse with central frequency of  $71.4\text{ cm}^{-1}$ .

transient signal is maximized when the MW radiation is on resonance with the EPR transitions. Figure 10.28(a) shows how the cross-section varies at three different times after the THz pulse. It is interesting to note that during the THz irradiation another broad transient absorption is superimposed to the left side of the sample signal. This is due to paramagnetic species contained in the sample holder (see chapter 7.3) whose signal decays about 20 times faster compared to that of the **VOTPP 2%** (Figure 10.30). The decay time of the sample signal measured on the tops (Figure 10.28(b)) as well as on the deeps (Figure 10.28(c)) of the cross-section is comparable and equal to ca. 30 ms. It is worth noting that the decay time measured in the two negative deeps (ca. 344 and 352 mT) is significantly longer.

A possible explanation comes from the fact that negative kinetics are only limited by thermal relaxation whereas positive ones are also limited by the temperature dependence of  $T_1$  which acts to shorten their decay. (Figure 10.29).

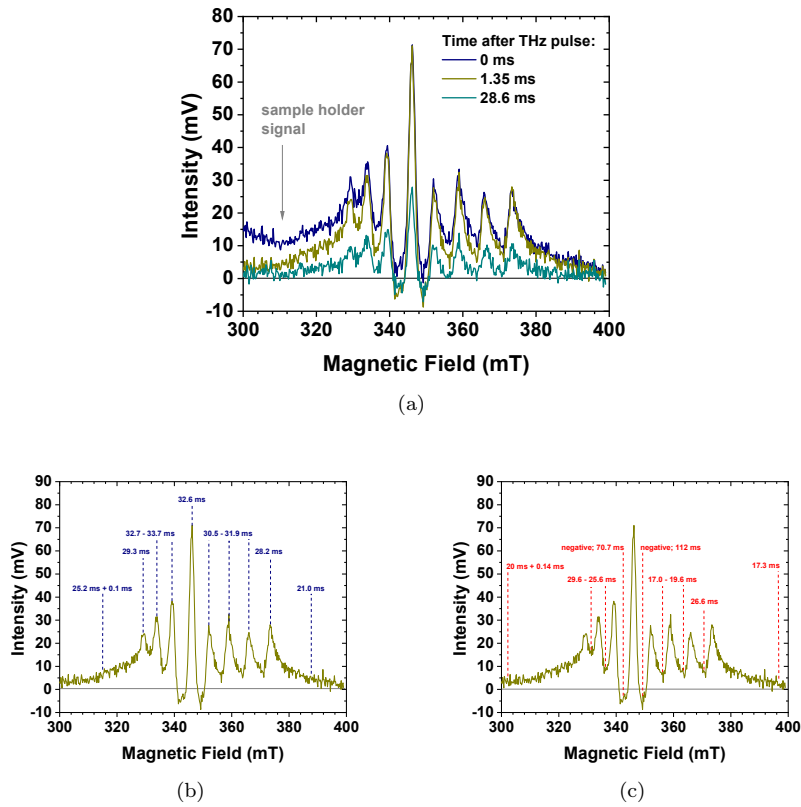


**Figure 10.28:** (a) Cross-section of 2D-THz-EPR spectrum at 20 K at three different times after the THz pulse: (blue line) 0 ms; (green line) 1.35 ms; (light blue) 28.6 ms. (b) Cross-section of 2D-THz-EPR spectrum at 1.35 ms: blue numbers are the characteristic times obtained by one exponential fitting in the maxima the spectrum, while (c) red numbers are those in the minima. MW frequency is 9.758 GHz, MW power is 200  $\mu$ W, THz radiation pulse length is 350  $\mu$ s, rep. rate is 1.8 Hz.



### 10.3. 2D-THz-EPR experiments

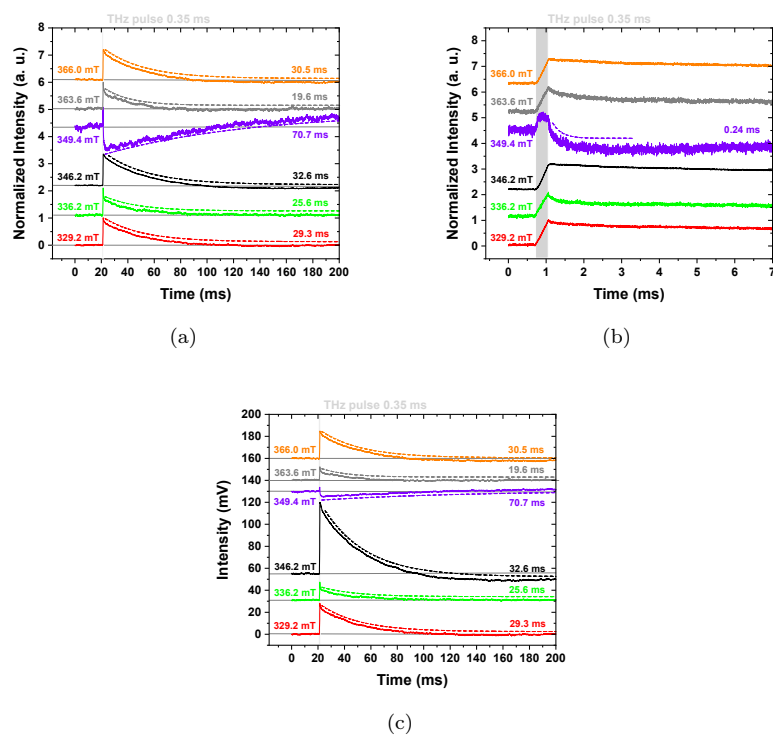


**Figure 10.29:** (a) Kinetics of 2D-THz-EPR spectrum at different magnetic field: 329.2, 346.2, 366.0 mT (maxima of the cross-section), 336.2, 349.1, 363.6 mT (minima of the cross-section) at 20 K. (b) Zoom of the kinetics at shorter times. (c) Not-normalized kinetics show that the intensity of the signal is much higher in the maxima with respect to the minima. Dashed lines show one exponential best-fit with its characteristic times. MW frequency is 9.758 GHz, MW power is 200  $\mu$ W, THz radiation pulse length is 350  $\mu$ s, rep. rate is 1.8 Hz.

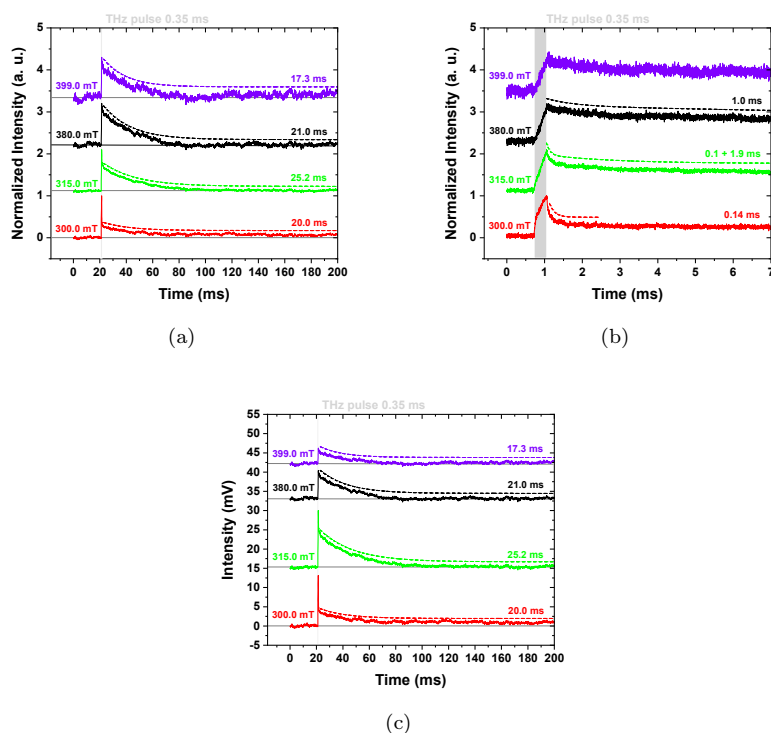


**Figure 10.30:** (a) Kinetics of 2D-THz-EPR spectrum at different magnetic field: 300.0, 399.0 mT (edges of the spectrum), 315.0, 380.0 mT (tails of the spectrum) at 20 K. (b) Zoom of the kinetics at shorter times. (c) Not-normalized kinetics show that the intensity of the signal is much higher in the maxima with respect to the minima. Dashed lines show one exponential best-fit with its characteristic times. MW frequency is 9.758 GHz, MW power is 200  $\mu$ W, THz radiation pulse length is 350  $\mu$ s, rep. rate is 1.8 Hz.

## 10.4 MW power dependence of TR-THz-EPR signal

In this section TR-THz-EPR kinetics as function of the MW power will be investigated. This is the most informative characterization because reveals a unprecedented behavior of the spin system response to THz irradiation. THz radiation has the spectrum shown in Figure 10.23 which is centered at  $71.4 \text{ cm}^{-1}$ . The macropulse lasts  $350 \mu\text{s}$  (Figure 10.27(a)), with a rep. rate of 1.8 Hz and averaged power of 100 W and 105 W for 20 and 55 K measurements, respectively.

Data was measured in a narrow magnetic field range around the top of the central line of 2D-THz-EPR map (346.1–346.2 mT). MW power was changed from  $0.2 \mu\text{W}$  (60 dB) to ca.  $3170 \mu\text{W}$  (18 dB) by steps of 6 dB.

The kinetics traces show a very different behavior when MW power is changed: at high attenuation levels, namely low MW power, the transient signal shows a fast decay follows by a slower rise to the equilibrium value. Such a tendency can be explained by considering the spin system, which is far from the saturation condition (at 20 K it approaches the saturation at ca. 40 dB and at 55 K at 30 dB as shown in section 10.2), experiences a sudden temperature jump due to the THz pulse, making the spin population change its distribution between the two levels, according to the Boltzmann factor. Indeed, a temperature rise makes the difference in population between the excited and ground states reduces, causing a drop of the EPR signal[21]. It is worth noting that the decay time is much longer compared to the THz pulse duration (Figure 10.31(c) and 10.31(d)) because of **VOTPP 2%** behaves as slow-relaxing system, namely the spin populations are not able to follow the fast temperature change. The fact that the signal decay time passes from ca. 0.40 ms at 20 K to ca. 0.15 ms at 55 K is explained taking into account the  $T_1$  shortening as shown by pulse-EPR data (see section 10.1.2). After that, the sample temperature slowly relaxes back to that of the thermal bath and the spin population restores its initial Boltzmann distribution. This leads to a gradual rising of the TR-EPR signal toward its initial value.

By increasing the MW power, the spin system is gradually pushed toward the saturation condition and, when the latter is approached, the transient signal suddenly changes its trend: it raises almost linearly during the THz pulse and then slowly decays to its equilibrium value. This can be explained considering a fast increase in population difference between the two spin states. Indeed, two phenomena contribute to such a fast growth, namely the shortening of  $T_1$  by increasing the temperature (see section 10.1.2) and a THz-induced spin relaxation mechanism which, to the best of our knowledge, can be related to a phonon-induced spin relaxation through spin-phonon coupling. The shorter

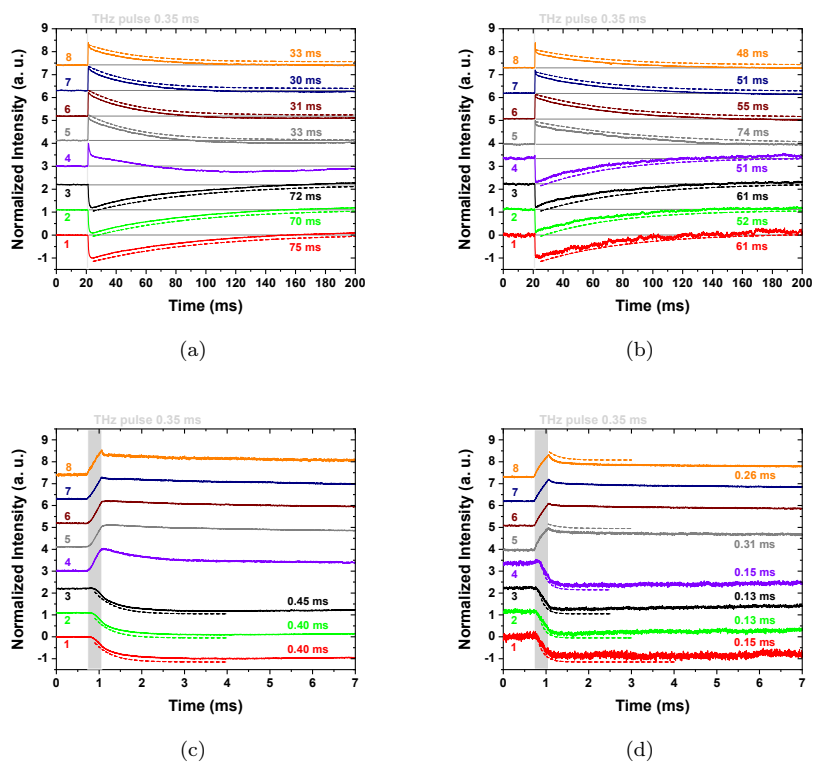


**Figure 10.31:** TR-THz-EPR kinetics of **VOTPP 2%** measured in magnetic field range of 346.1-346.2 mT, i.e. on the central line, at 20 K (long time-scale (a) and short time-scale (c)) and 55 K (long time-scale (b) and short time-scale (d)), at different microwave power attenuation: (1) 60 dB; (2) 54 dB; (3) 48 dB; (4) 42 dB; (5) 36 dB; (6) 30 dB; (7) 24 dB; (8) 18 dB. MW frequency is 9.760 GHz, THz pulse length is 350  $\mu$ s, rep. rate is 1.8 Hz. The kinetics are horizontally shifted for a better comparison. Dashed lines show the single exponential best-fit with its characteristic times. Solid gray lines represent the base level for each kinetics.

#### 10.4. MW power dependence of TR-THz-EPR signal

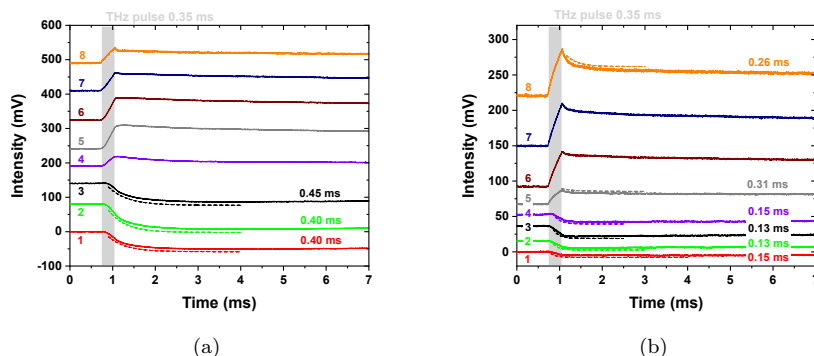


**Figure 10.32:** Not-normalized averaged TR-THz-EPR kinetics of **VOTPP 2%** measured in magnetic field range of 346.1-346.2 mT, i.e. on the central line, at 20 K (a) and 55 K (b), at different microwave power attenuation: (1) 60 dB; (2) 54 dB; (3) 48 dB; (4) 42 dB; (5) 36 dB; (6) 30 dB; (7) 24 dB; (8) 18 dB. MW frequency is 9.760 GHz, THz pulse length is 350  $\mu$ s, rep. rate is 1.8 Hz. The kinetics are horizontally shifted for a better comparison. Dashed lines show the single exponential best-fit with its characteristic times. Solid gray lines represent the base level for each kinetics.

thermal relaxation compared to the not saturated situation can be attributed to the  $T_1$  variation by changing the temperature. Indeed, the temperature dependence of  $T_1$  heavily contributes when the spin system is close to the saturation condition, since the temperature variation does not affect the difference in the spin population as strong as when the system is far from the saturation.

Figure 10.32 shows kinetics traces without the normalization and it is clear that also the intensity of the signal jump (negative at low MW power and positive at high MW power) dramatically depends on the MW power, as shown in Figure 10.33.

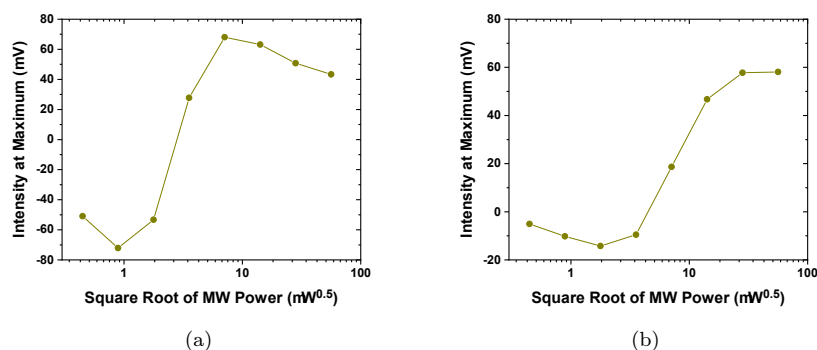


**Figure 10.33:** Dependence of the intensity of signal at the maximum (minimum) as function of the square root of MW power, at 20 K (a) and 55 K (b).

## 10.5 Temperature dependence of TR-THz-EPR signal

The TR-THz-EPR signal shows an interesting temperature dependence which deserves to be discussed in this section. The applied THz radiation has the spectrum shown in Figure 10.23 whose central frequency is  $71.4 \text{ cm}^{-1}$ . The pulse duration is again  $350 \text{ }\mu\text{s}$  with the profile shows in Figure 10.27(a) and rep. rate of  $1.8 \text{ Hz}$ . The MW power is kept fixed at  $200 \text{ }\mu\text{W}$  (ca.  $30 \text{ dB}$ ) maintaining the **VOTPP 2%** in saturation condition. Since this kind of experiments is relatively time-consuming and the power stability over such a long time of FEL-generated THz radiation is not ensured, the latter has been measured several times at each temperature set on the cryostat and its average is reported in table 10.2.

Temperature (K)	Average THz power (W)
7	82
7	70
13	70
13	100
20	87
27	86
35	86
43	82
55	86
70	76

**Table 10.2:** THz power measured during the experiment at each temperature. At 7 and 13 K the power has been measured two times because of FEL instability.

The intensity at the maximum of TR-THz-EPR signals for each temperature has been normalized on the same reference THz power equal to  $86 \text{ W}$  by using the calibration function  $I(mV) = -5.71 + 0.74 \cdot P(W)$  ( $I_{int}(a.u.) = -12.3 + 1.5 \cdot P(W)$  for the integral intensity).

The 2D-THz-EPR spectrum around the central line of the TR signal (see Figure 10.25) is shown in Figure 10.34. The temperature dependence of the cross-section and the kinetics signal (positive), have been investigated at  $21.4 \text{ ms}$  (white dashed line) and at  $346.2 \text{ mT}$  (red dashed line), respectively.

The cross-section as a function of temperature is shown in Figure 10.35(a) while its intensity at the maximum ( $346.2 \text{ mT}$ ) and its integral intensity are shown in Figure 10.35(b) and Figure 10.35(c), respectively.

Both the intensity and the integral intensity show the same behavior, being almost constant from  $7$  to  $43 \text{ K}$  followed by a decrease at higher temperatures.

### 10.5. Temperature dependence of TR-THz-EPR signal

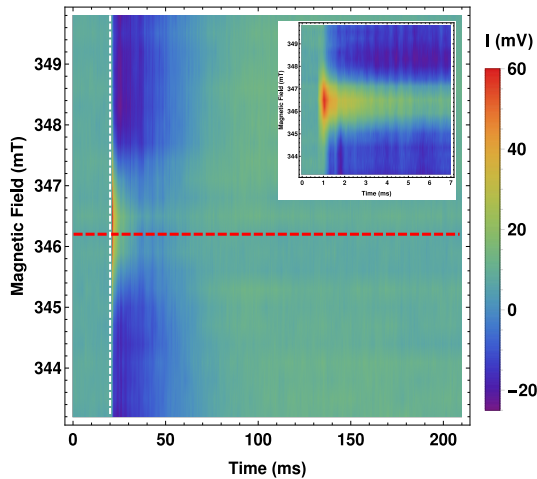


**Figure 10.34:** 2D-THz-EPR spectrum around the central line at 7 K. MW frequency is 9.758 GHz, MW power is  $200 \mu\text{W}$ , THz radiation pulse length is  $350 \mu\text{s}$ , rep. rate is 1.8 Hz. Red and white dashed lines show the magnetic field (346.2 mT) and the time (21.4 ms), respectively, at which the temperature dependence of the positive signal has been sampled. The inset show the zoom at short time of the 2D map.

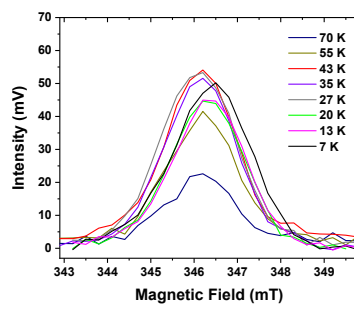
The kinetics as function of temperature are shown in Figure 10.36(a). It is worth noting that not only the intensity of the signal (Figure 10.35(b)), but also its decay is affected by the temperature. Indeed, the decay time rises until 43 K followed by a slightly decrease as shown in Figure 10.36(b). It is interesting to note that the shape of the kinetics changes according to the temperature showing a sharp decay to negative values followed by a rise toward the equilibrium value at the two lowest temperature. The curves gradually change to a slower decay directly to the equilibrium value at temperature higher than or equal to 20 K (Figure 10.36(c)).

This peculiar behavior cannot be reproduced by the model discussed in section 10.8, since a more complex thermal relaxation mechanism should take into account through multi-exponential decay.

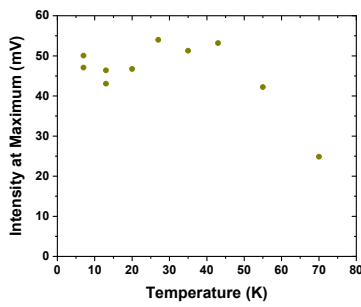
Not only the positive signal, but also the negative one between the central line at 346.2 mT and the following at ca. 352 mT has been analyzed as a function of temperature. The cross-section as well as the kinetics has been investigated at 27 ms (white dashed line) and 349.8 mT (red dashed line), respectively (Figure 10.37).

The temperature behavior of the cross-section is shown in Figure 10.38(a) and the intensity at 349.8 mT is reported in Figure 10.38(b). The amplitude of the signal decays very fast reaching a constant value already at 20 K.

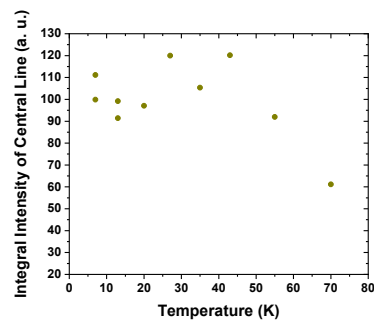
The kinetics at 349.8 mT as function of temperature are shown in Fig-



(a)



(b)



(c)

**Figure 10.35:** (a) Spectra of the central line at 21.4 ms at different temperatures. (b) Temperature dependence of the intensity and (c) of the integral intensity of the signal at 346.2 mT and 21.4 ms. The intensity was recalculated to the same averaged power of 86 W. MW frequency is 9.758 GHz, MW power is 200  $\mu$ W, THz radiation pulse length is 350  $\mu$ s, rep. rate is 1.8 Hz.



10.5. Temperature dependence of TR-THz-EPR signal

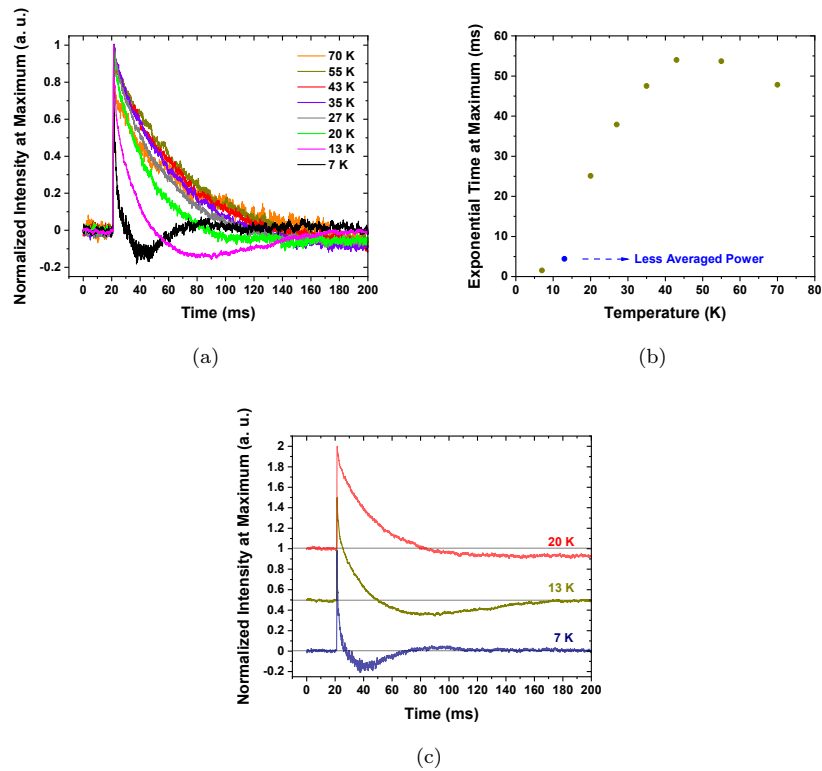


**Figure 10.36:** (a) Normalized kinetics at 346.2 mT at different temperatures. (b) Temperature dependence of the characteristic time of the single exponential best-fit. The fit takes into account also the negative part of kinetics, which substantially affects their shape. (c) Comparison of the normalized kinetics at 7, 13, and 20 K at 346.2 mT. Kinetics at 13 and 20 K are horizontally shifted for a better comparison. Gray lines represent the base level for each kinetics.

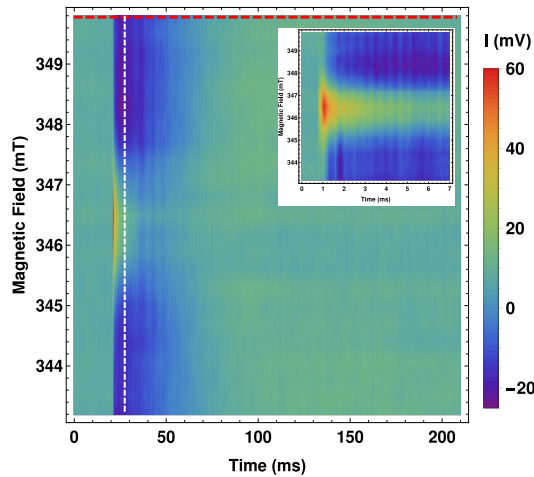


**Figure 10.37:** 2D-THz-EPR spectrum around the central line at 7 K. MW frequency is 9.758 GHz, MW power is  $200 \mu\text{W}$ , THz radiation pulse length is  $350 \mu\text{s}$ , rep. rate is 1.8 Hz. Red and white dashed lines show the magnetic field (349.8 mT) and the time (27 ms), respectively, at which the temperature dependence of the negative signal has been sampled. The inset show the zoom at short time of the 2D map.

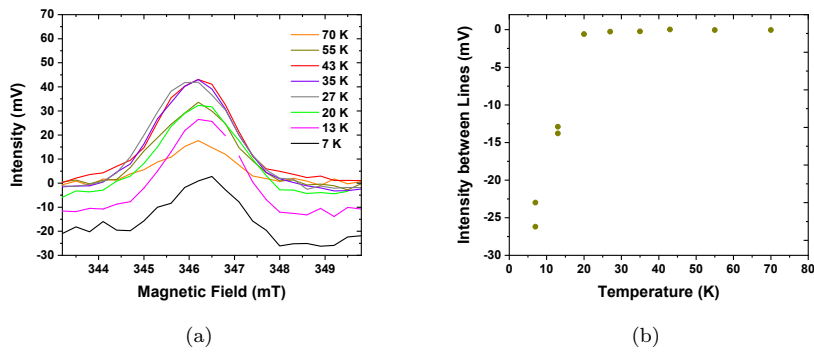


**Figure 10.38:** (a) Spectra of the negative signal between the central line and the following one at 27 ms at different temperatures. (b) Temperature dependence of the intensity of the signal at 349.8 mT and 27 ms. The intensity was recalculated to the same averaged power of 86 W. MW frequency is 9.758 GHz, MW power is  $200 \mu\text{W}$ , THz radiation pulse length is  $350 \mu\text{s}$ , rep. rate is 1.8 Hz.

### 10.5. Temperature dependence of TR-THz-EPR signal

ure 10.39(a) and the single exponential best-fit decay time of the kinetics at 7, 13, 20 and 27 K is reported in Figure 10.39(b). Indeed, the decay time of the negative signal increases becoming ca. two times longer passing from 7 to 30 K.

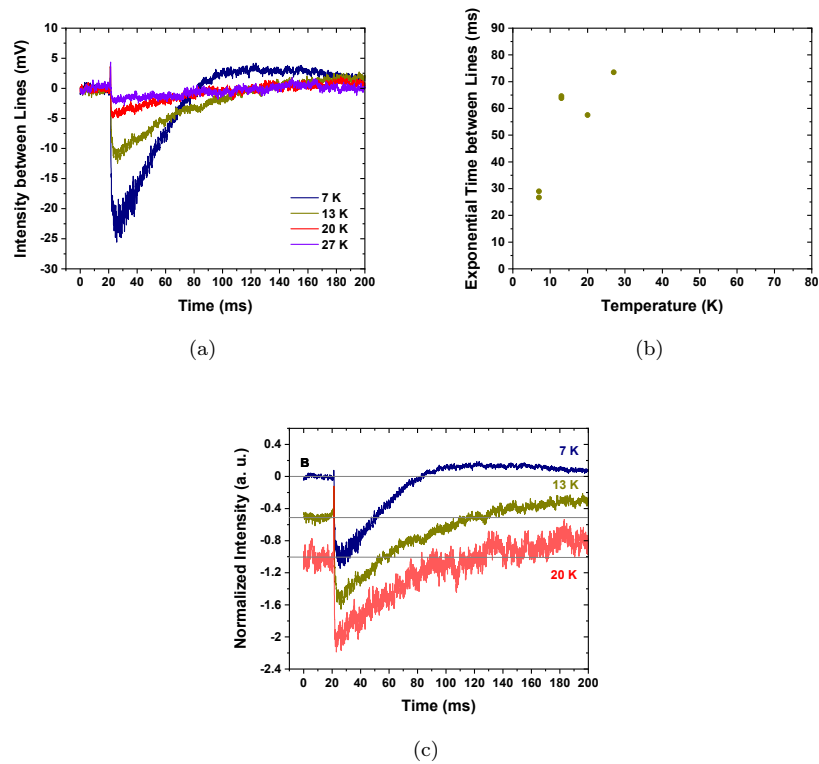


**Figure 10.39:** (a) Normalized kinetics at 349.8 mT at different temperatures. (b) Temperature dependence of the characteristic time of the single exponential best-fit. (c) Comparison of the normalized kinetics at 7, 13, and 20 K at 349.8 mT. Kinetics at 13 and 20 K are horizontally shifted for a better comparison. Gray lines represent the base level for each kinetics.

The behavior of the negative signal is similar to that observed for a not saturated spin system, despite the MW power keeps the spin system in the saturation regime. Perhaps it depends on sample inhomogeneity that could lead to have a small part of [VO(TPP)] molecules with much shorter spin-lattice relaxation time.

## 10.6 THz radiation frequency dependence of the TR-THz-EPR signal

In this section it will be investigated the effect of the THz irradiation frequency in a range around the phonon band (central frequency  $71.3 \text{ cm}^{-1}$  at 10 K), when the spin system is saturated by the MW radiation. It was previously discussed that the spin relaxation shortening during the THz irradiation is strongly connected to the lowest-energy vibrational mode of the **VOTPP 2%** crystal. In this frame, the resonance condition of THz radiation with the energy of the unique observed phonon has to be mandatory in the detection of the positive TR-EPR signal. The spectra of the THz radiation at the selected frequencies are shown in Figure 10.40. Since the THz radiation passes through the air at least from the exit of the beamline station to the EPR resonator, the water vapour absorption must be taken into account in the choice of the THz wavelength. Indeed, choosing a radiation wavelength coinciding with an absorption band of water vapour would reduce dramatically the power experienced by the sample. In this frame, the selected THz frequencies fall as far as possible from the water absorption bands (red solid line in Figure 10.40).

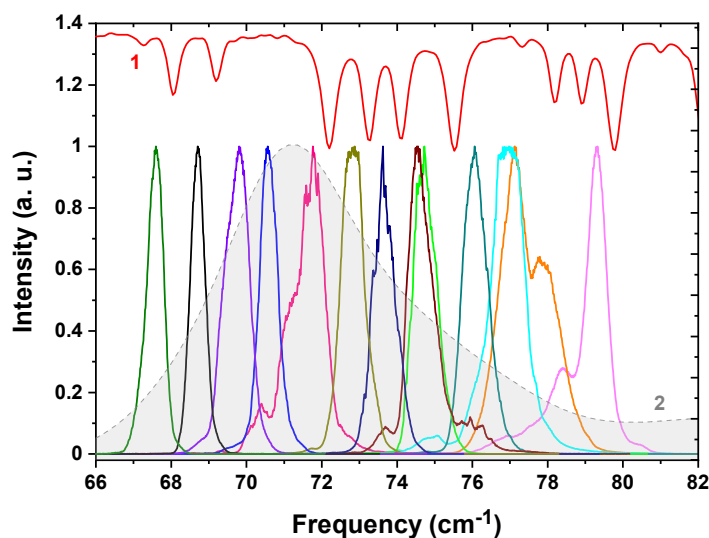


**Figure 10.40:** Spectra of THz radiation used in the experiments for measuring the THz frequency dependence. Red line (1) schematically shows the transparency of atmosphere for 0.2 m of optical length. The maximum of absorption band at  $75.5 \text{ cm}^{-1}$  corresponds to 15% of transparency. Dashed gray line (2) schematically shows **VOTPP 2%** FIR spectrum at 10 K. The maximum of absorption band at  $71.3 \text{ cm}^{-1}$  is equal to 0.357 a.u. of optical density.

As for the investigation of temperature dependence of TR-THz-EPR signal,

10.6. THz radiation frequency dependence of the TR-THz-EPR signal

the THz power has been monitored during the experiment and its value is reported in table 10.3 for each THz frequency.

THz frequency ( $\text{cm}^{-1}$ )	THz power (W)
67.6	36.0
68.7	54.5
69.8	66.5
70.6	66.8
71.6	65.0
72.8	68.3
73.7	59.0
74.6	60.5
74.8	72.5
76.1	71.0
76.9	72.0
77.2	65.5
79.4	68.6

**Table 10.3:** THz power at different THz frequency used to measure the dependence of the TR-THz-EPR signal on the THz frequency.

Also in this case, the cross-sections measured as function of the THz frequency are normalized on the reference power value of 66 W. As for the previous experiments, the THz pulse length is 350  $\mu\text{s}$  and the rep. rate is 1.8 Hz. The cross-section around the central line (346.2 mT) as function of the THz irradiation frequency is shown in Figure 10.41(a). Its intensity and integral intensity, normalized on the reference THz power, are shown in Figure 10.41(b) and 10.41(c).

It is interesting to note that both the intensity and the integral intensity follow the absorption band profile of the phonon (dashed blue line).

The normalized kinetics measured at 346.2 mT for each THz frequency are shown in Figure 10.42. The difference in the shape of the kinetic profiles, i.e. the decay times, measured very close to the top of the phonon band and on its upper edge can be related to the lower efficiency in perturbing the spin system when the irradiation frequency is set out of the resonance with the phonon at 71.3  $\text{cm}^{-1}$ .

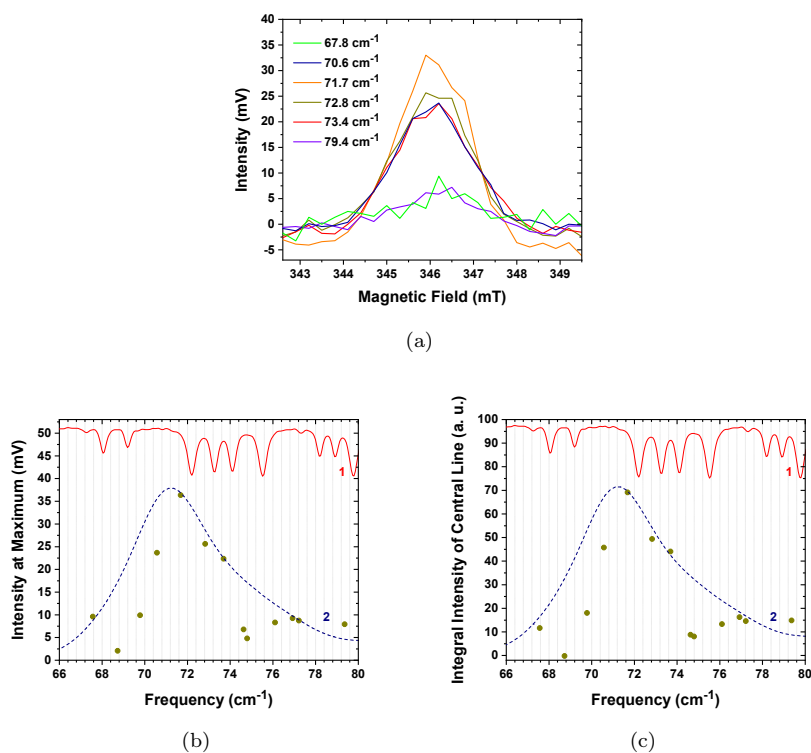


**Figure 10.41:** (a) Several cross-sections of the central line (around 346.2 mT) at 21.4 ms at different THz frequency. (b) Dependence of the intensity and (c) of the integral intensity of positive signal on THz radiation frequency at 342.6 mT and 21.4 ms. The temperature is 20 K, MW frequency is 9.760 GHz, MW power is 200  $\mu$ W, THz radiation pulse length is 350  $\mu$ s, rep. rate is 1.8 Hz. The intensity was recalculated to the same averaged power of 66 W. The red line (1) schematically shows the transparency of atmosphere for 0.2 m optical length. Dashed dark blue line (2) schematically shows VOTPP 2% FIR spectrum at 10 K.

### 10.7. THz power dependence of the TR-THz-EPR signal

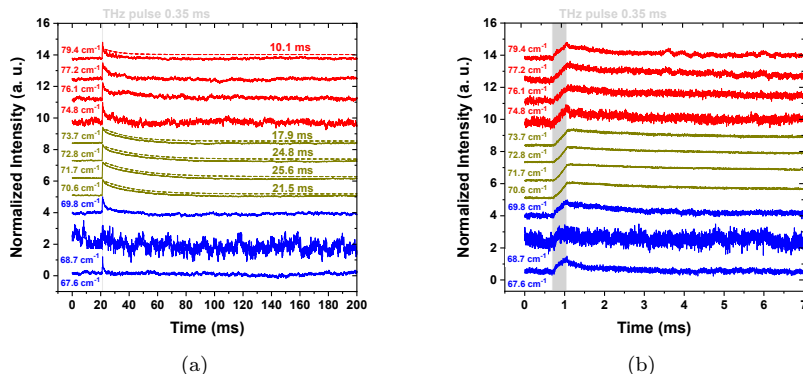


**Figure 10.42:** Normalized kinetics of positive signal at different THz radiation frequencies at the magnetic field corresponding to the maximum signal (averaged in the range of 345.6–346.6 mT) in two different timescales. Kinetics taken at THz frequencies lower than the resonance value are shown in blue, those taken very close to the resonance are shown in dark green, and those taken at frequencies higher than the resonance value are shown in red. Each kinetics shows the THz irradiation frequency on the left side. Each subsequent kinetics is horizontally shifted. Dashed lines show one exponential fit with the characteristic times shown on the right side of the figure. The temperature is 20 K, MW frequency is 9.760 GHz, MW power is 200  $\mu$ W, THz radiation pulse length is 350  $\mu$ s, rep. rate is 1.8 Hz.

## 10.7 THz power dependence of the TR-THz-EPR signal

This section is devoted to the characterization of the THz power dependence of the TR-THz-EPR signal. Indeed, since it is a THz-induced phenomenon, it should show a well-defined dependence on THz power. For this purpose, several power values have been tested, from 8 to 110 W. The spectral band of THz radiation is centered at 71.3  $\text{cm}^{-1}$  (Figure 10.23), the pulse duration is 350  $\mu$ s (Figure 10.27(a)) at a rep. rate of 1.8 Hz. The cross-sections of the TR-THz-EPR signal around the central line at 21.4 ms and the kinetics at 346.2 mT as function of THz power are shown in Figure 10.43. The intensity and the integral intensity of the cross-section (346.2 mT) at 21.4 ms at different THz power are shown in Figure 10.44.

It is clear that both of them show a perfectly linear trend that reveals the “single-photon” or, considering the effect as phonon-mediated, “single-phonon” nature of the phenomenon, according to the Fermi’s Golden Rule (see equation (10.6)).

$$\Gamma_{if} = \frac{2\pi}{\hbar} |M_{if}|^2 \rho_f \propto I_{THz} \quad (10.6)$$

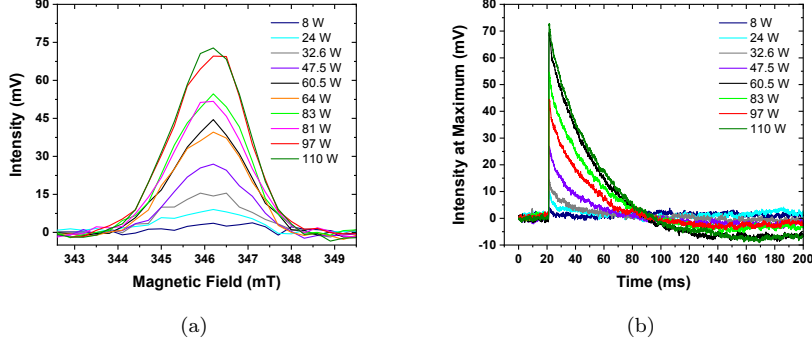


**Figure 10.43:** (a) Cross-sections around the central line at different average power of THz radiation at 21.4 ms. (b) Kinetics of positive signal at different average power of THz radiation at 346.2 mT. Temperature is 20 K, MW frequency is 9.760 GHz, MW power is 200  $\mu$ W, THz radiation pulse length is 350  $\mu$ s, rep. rate is 1.8 Hz.

In the equation (10.6),  $\Gamma_{if}$  represents the transition probability between the ground and the excited states,  $M_{if} = \langle f | \mathcal{H}' | i \rangle$  is the matrix element of the perturbation  $\mathcal{H}'$  between the final and initial states and  $\rho_f$  is the density of states at the energy  $E_f$ . Indeed, the Fermi's Golden rule states the linear dependence of the transition probability by the THz power considering  $\mathcal{H}' \propto E_{THz}$ , where  $E_{THz}$  is the electric field of the THz radiation.

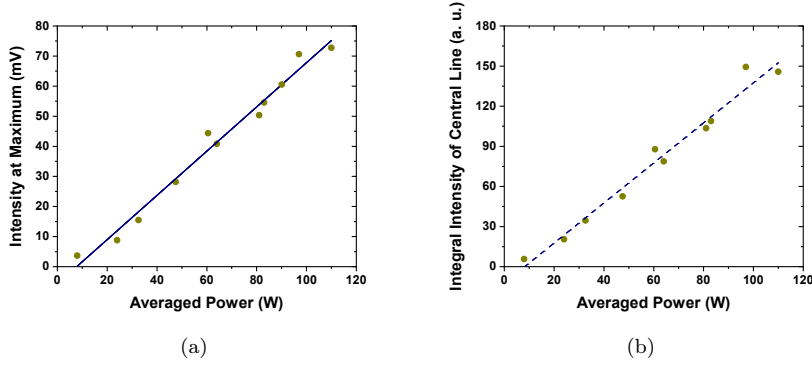


**Figure 10.44:** Dependence of the intensity (a) and of the integral intensity (b) of the positive signal on average power of THz radiation at 346.2 mT and 21.4 ms. Temperature is 20 K, MW frequency is 9.760 GHz, MW power is 200  $\mu$ W, THz radiation pulse length is 350  $\mu$ s, rep. rate is 1.8 Hz.

Also the decay time of the kinetics (Figure 10.45(b)) shows an almost linear dependence from the THz power. This feature is still unclear and further studies are required.



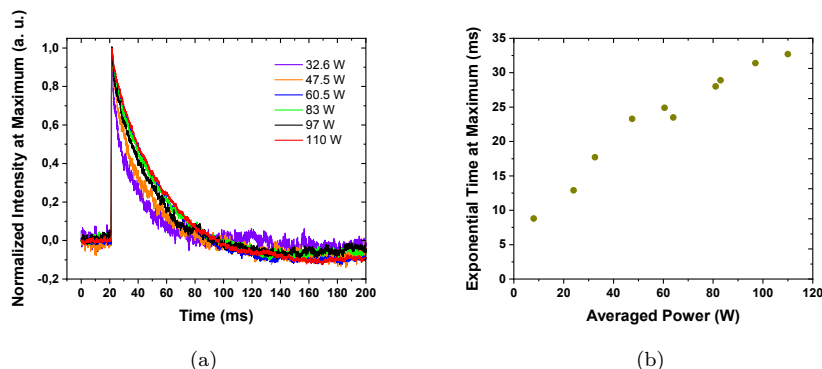


**Figure 10.45:** (a) Normalized kinetics of positive signal at different average power of THz radiation at 346.2 mT. (b) Dependence of the decay time of the single exponential best-fit of the signal relaxation on average THz power at 346.2 mT. Temperature is 20 K, MW frequency is 9.760 GHz, MW power is 200  $\mu$ W, THz radiation pulse length is 350  $\mu$ s, rep. rate is 1.8 Hz.

## 10.8 Simulations

The simulation of time-resolved EPR experiment under pulsed THz irradiation is based on a modified version of the Bloch equations (the origin of the standard Bloch equations are discussed in Appendix B). This is the simplest model which is able to take into account the main manifestations of THz-induced spin relaxation. Indeed, it includes not only the saturation of the spin system by MW radiation, but also the heating of the sample by THz radiation and the temperature dependence of  $T_1$ . Moreover, an additional term which takes into account the phonon-mediated THz-induced relaxation of the spin system is included. The latter will be alternatively considered or neglected in the simulations to highlight the different results in comparison with the experimental data. By this model, two aspects will be simulated, namely the MW power dependence and the THz power dependence of the TR-THz-EPR signal, respectively mentioned in section 10.4 and 10.7. Running the simulations requires to know the temperature dependence of the spin-lattice relaxation time, reported in section 10.1.2, that of the spin-spin relaxation time which is taken from chapter 9.4 and [22], and the heat capacity,  $C_v$ , of **VOTPP**. The latter is obtained by *ab initio* calculations and it is shown in Figure 10.46. It is very similar to that of VO(acac)<sub>2</sub> which is, to the best of our knowledge, the only relevant experimental data in literature concerning the heat capacity of vanadyl-based complexes at helium temperatures[23].

The calculated heat capacity values were fitted by using an arbitrary polynomial function  $C_v(T) = a + bT + cT^2 + dT^3 + eT^4$  to have an approximation of it

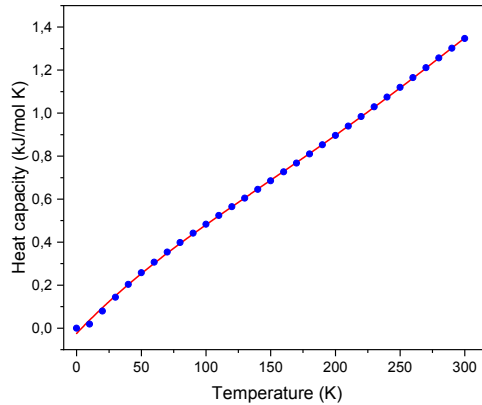


**Figure 10.46:** Calculated heat capacity of VO(TPP) (blue dots) and its polynomial fit (red line).

at different temperature.

As mentioned in section 10.1.2, the recovery kinetics has been fitted by using:

- a single exponential decay function;
- a three exponential decay function.

The former allows to take into account the presence of [VO(TPP)] molecules with different relaxation time, whereas the latter permits to highlight the effect of long relaxation time on the amplitude of the phenomenon. The temperature behaviour of  $T_1$ , either extrapolated by the single exponential decay best-fit or coincident with the longer decay time of the three exponential best-fit, is shown in Figure 10.13(b) and 10.13(a) in section 10.1.2. The  $T_1$  temperature dependence was also fitted by using an arbitrary smooth function  $g(T) = a e^{(-T/b)} + c + dT + eT^2$ . The aim was not the physically correct description of  $T_1$  behavior, but having a reasonable approximation of experimental  $T_1$  at different temperatures.

### 10.8.1 Description of the model

The model consists in a set of three modified Bloch equations (see equations 10.9). The one related to the dynamics of the  $z$ -component of the magnetization changes according to the time lapse of the experiment:

1. before the THz pulse irradiates the sample;
2. during the sample irradiation;

3. after the pulse.

These three time lapses affect the  $z$ -component of the Bloch equation as follow

$$\frac{dM_x}{dt} = -\frac{M_x}{T_2(T_{\text{experiment}})} \quad (10.7)$$

$$\frac{dM_y}{dt} = \omega_1 M_z - \frac{M_y}{T_2(T_{\text{experiment}})} \quad (10.8)$$

$$\frac{dM_z}{dt} = \begin{cases} -\omega_1 M_y - \frac{M_z - M_0}{T_1(T_{\text{experiment}})} & \text{when } 0 \leq t < \tau_1 \\ -\omega_1 M_y - \frac{M_z - M_0(1 - H(t, T))}{T_{\text{THz}}} - \frac{M_z - M_0(1 - H(t, T))}{T_1(T_{\text{pulse}})} & \text{when } \tau_1 \leq t \leq \tau_1 + \tau_2 \\ -\omega_1 M_y - \frac{M_z - M_0 \left( 1 - H(t, T) \exp\left(-\frac{t - \tau_1 - \tau_2}{T_{\text{term}}}\right) \right)}{T_1(T_{\text{after}})} & \text{when } t > \tau_1 + \tau_2 \end{cases} \quad (10.9)$$

where the two time lapses  $\tau_1$  and  $\tau_2$  are, respectively, the time needed by the spin system to reach the equilibrium under CW-MW irradiation and the duration of THz pulse.  $H(t, T)$  is a function defining the difference in  $M_0$  at different temperature;  $T_1(T)$  and  $T_2(T)$  are the relaxation times as a function of temperature;  $T_{\text{THz}}$  is the additional relaxation channel operating only during THz pulse, due to the spin-phonon coupling;  $T_{\text{term}}$  is the sample thermal relaxation toward the equilibrium condition after the THz heating. The temperature of the sample during the different periods of the experiment are treated as follow

$$T_{\text{experiment}} = \text{const}, \quad \text{temperature of the cryostat} \quad (10.10)$$

$$T_{\text{pulse}} = T_{\text{final}} \quad \text{derived from} \quad Q(t) = \int_{T_{\text{initial}}}^{T_{\text{final}}} C(T) dT \quad (10.11)$$

$$T_{\text{after}} = (T_{\text{after pulse}} - T_{\text{experiment}}) e^{-(t - \tau_1 - \tau_2)/T_{\text{term}}} + T_{\text{experiment}} \quad (10.12)$$

During the THz pulse, the heating of the sample is taken into account by numerically solving the equation 10.11, where the upper limit of the integral corresponds to the instant temperature i.e. the temperature at that  $t$  value.  $C(T)$  is the heat capacity of the material, which also depends on the temperature (Figure 10.46).

After the pulse, the temperature exponentially relaxes back to its initial value,  $T_{\text{experiment}}$ , with a decay time equal to  $T_{\text{term}}$ . The  $Q(t)$  function i.e. the amount of heat absorbed by the sample during the THz pulse, is calculated as follow

$$Q(t) = \begin{cases} 0 & 0 \leq t < \tau_1 \\ \frac{A}{\tau_2}(t - \tau_2) & \tau_1 \leq t \leq \tau_1 + \tau_2 \\ 0 & t > \tau_1 + \tau_2 \end{cases} \quad (10.13)$$

where A is an empirical parameter that was estimated to be 12.105 for THz power of ca. 100 W, i.e. the THz power during the MW power dependence experiment. The  $H(t, T)$  function, which defines the magnitude of  $M_0$  at different temperatures, is calculated in the following way

$$H(t, T) = \frac{T_{pulse} - T_{experiment}}{T_{pulse}} \quad (10.14)$$

Two sets of parameters have been used in the simulations of MW power dependence of TR-THz-EPR signal:

- $T_1$  coincident with the longest decay time from three exponential best-fit.  $T_{THz}=260$  ms,  $T_{term}=55$  ms,  $\tau_2=350$   $\mu$ s;
- $T_1$  coincident with the decay time from the sigle exponential best-fit.  $T_{THz}=250$  ms,  $T_{term}=55$  ms,  $\tau_2=350$   $\mu$ s;

Only  $\omega_1$  has varied in the range corresponding to 60–18 dB. Simulations have been carried out at 20 and 55 K, the two temperatures at which the complete MW power dependence was investigated (see section 10.4).

## 10.8.2 Simulation of MW power dependence at 20 K

### $T_1$ equals to the longest decay time from three exponential fitting

The model qualitatively describes the shape of experimental kinetics and its behavior at different MW power, including the jump from negative to positive THz-induced signal (Figure 10.47 and 10.48). As it follows from curves 5-6 of Figure 10.48(a) and 10.48(b), without the additional relaxation during THz pulse, the initial part of kinetics after the THz pulse at moderate MW power has the behavior determined by  $T_1$  and does not have the linear behavior simulated with  $T_{THz} = 260$  ms and measured in experiment. In addition to the linear behavior of kinetics during THz pulse at MW power corresponding to the saturation, the additional relaxation during THz pulse also affects the parts of kinetics right after THz pulse, that starts with characteristic time  $T_1$  and then continue with  $T_{term}$ . (Compare curves 6-8 in Figure 10.48(a) and 10.48(b)). Similar behavior can also be seen in experimental data (see curves 7-8 in Figure 10.48(c)). The mentioned linear behavior of kinetics during THz pulse with additional relaxation  $T_{THz}=260$  ms can be simulated at each MW power that saturates the spin

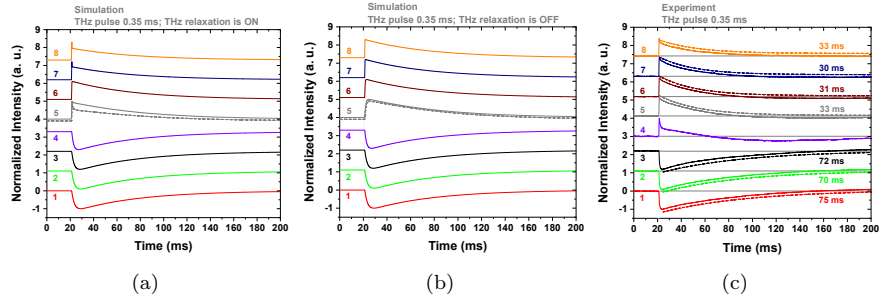


**Figure 10.47:** (a) Simulations of the signal with following parameters:  $T=20$  K,  $T_{THz}=260$  ms,  $T_{term}=55$  ms,  $\tau_2=350$   $\mu$ s; (b) simulation without the additional THz-induced relaxation channel ( $T_{THz} = \infty$ ) and (c) experimental data at different MW power (1) 60 dB; (2) 54 dB; (3) 48 dB; (4) 42 dB; (5) 36 dB, dashed gray line 36.5 dB; (6) 30 dB; (7) 24 dB; (8) 18 dB. The kinetics are horizontally shifted for a better comparison.

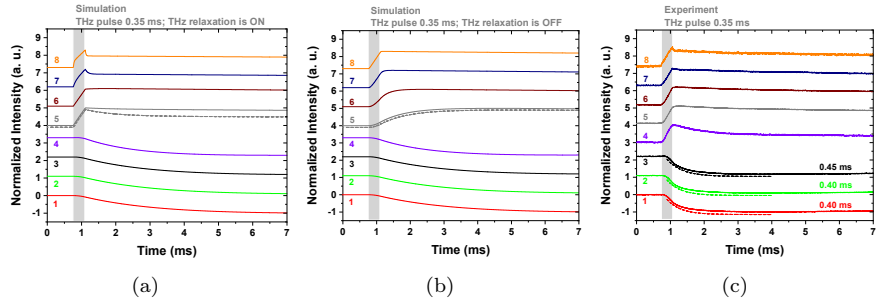


**Figure 10.48:** (a) Zoom at shorter times of the simulations of the signal with following parameters:  $T=20$  K,  $T_{THz}=260$  ms,  $T_{term}=55$  ms,  $\tau_2=350$   $\mu$ s; (b) simulation without the additional THz-induced relaxation channel ( $T_{THz} = \infty$ ) and (c) experimental data at different MW power (1) 60 dB; (2) 54 dB; (3) 48 dB; (4) 42 dB; (5) 36 dB, dashed gray line 36.5 dB; (6) 30 dB; (7) 24 dB; (8) 18 dB. The kinetics are horizontally shifted for a better comparison.

system. Using  $T_{THz} = \infty$ , the linear behavior can be obtained only at high MW power.

The long tails of both positive and negative kinetics (curve 1-8 in Figure 10.47(a) and 10.50(a)) are due to substantial heating effects of THz radiation that also affects  $T_1$  relaxation time, since the latter drastically decreases with the temperature rise. Long tails can also be reproduced without additional relaxation during THz pulse (see Figure 10.47(b) and 10.50(b)).

The region between 42 and 36 dB is extremely sensitive to MW power as it is clearly visible in the comparison between the dashed and solid curve 5 in Figure 10.47(a) and 10.48(a) and Figure 10.50(a) and 10.51(a). The shift of 0.5 dB is enough to better reproduce the experimental kinetics. As already discussed, the simulated kinetics seem to be 6 dB shifted in comparison with experimental kinetics. This is due to the not exactly correct MW power calibration. The impact of the heat capacity on the simulation is bright: the thermal effect of THz radiation is substantial for both unsaturated and saturated region. The heat capacity of the sample at different temperatures can change the relative contribution of positive and negative kinetics to the resulting ones.

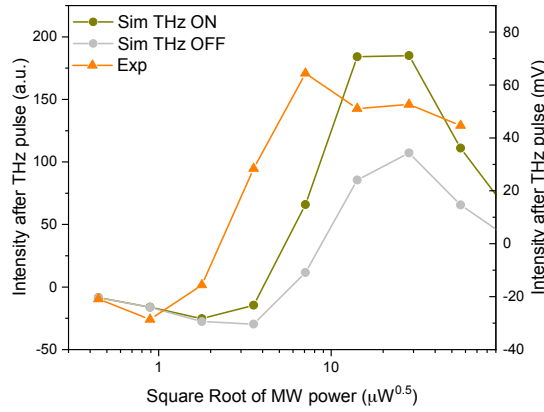


**Figure 10.49:** Dependence at 20 K of the signal intensity at 21.4 ms on the square root of MW power, obtained by the three exponential fitting of  $T_1$ . Green circles show data with additional relaxation during THz pulse channel,  $T_{THz} = 260$  ms; gray circles show the same without additional relaxation,  $T_{THz} = \infty$ ; orange triangles show the experimental data.

The simulated absolute intensities of the signal right after THz pulse (Figure 10.49) reasonable reproduce the experimental data, once shifted for 6 dB. As already mentioned, the shift is due to the incorrect calibration that allows to obtain the MW power from the attenuation. The latter is, indeed, the param-

eter which is experimentally accessible, while the MW power is achievable only through a calibration procedure.

The effect of the additional relaxation during the THz pulse is clearly visible where the intensity of the signal after the THz pulse rises up much faster upon MW power increase compared to the simulation without THz spin relaxation.

### $T_1$ equals to the decay time from single exponential fitting

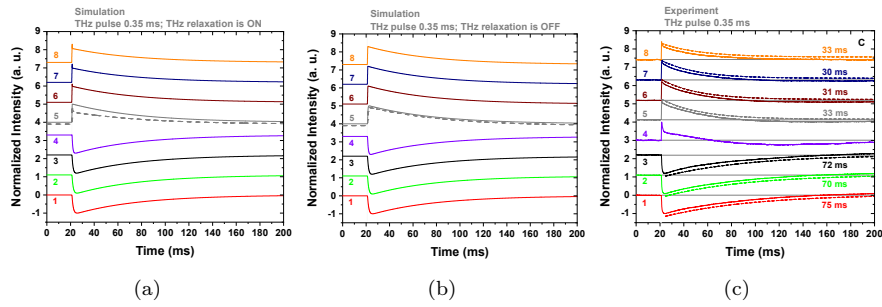


**Figure 10.50:** (a) Simulations of the signal with following parameters:  $T=20$  K,  $T_{THz}=250$  ms,  $T_{term}=55$  ms,  $\tau_2=350$   $\mu$ s; (b) simulation without the additional THz-induced relaxation channel ( $T_{THz} = \infty$ ) and (c) experimental data at different MW power (1) 60 dB; (2) 54 dB; (3) 48 dB; (4) 42 dB; (5) 36 dB, dashed gray line 36.5 dB; (6) 30 dB; (7) 24 dB; (8) 18 dB. The kinetics are horizontally shifted for a better comparison.

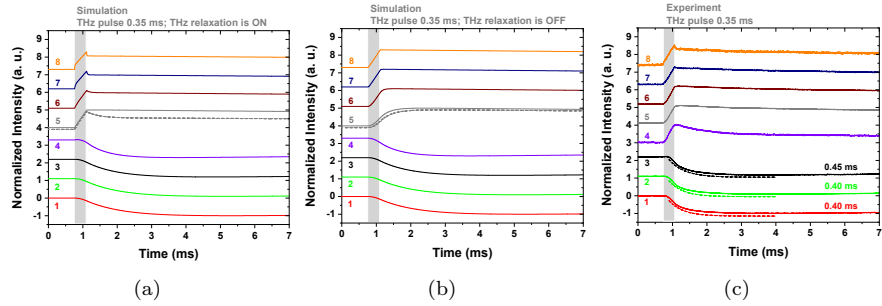


**Figure 10.51:** (a) Zoom at shorter times of the simulations of the signal with following parameters:  $T=20$  K,  $T_{THz}=250$  ms,  $T_{term}=55$  ms,  $\tau_2=350$   $\mu$ s; (b) simulation without the additional THz-induced relaxation channel ( $T_{THz} = \infty$ ) and (c) experimental data at different MW power (1) 60 dB; (2) 54 dB; (3) 48 dB; (4) 42 dB; (5) 36 dB, dashed gray line 36.5 dB; (6) 30 dB; (7) 24 dB; (8) 18 dB. The kinetics are horizontally shifted for a better comparison.

The simulations of the experimental data at 20 K by using the  $T_1$  coincident with the decay time of the single exponential fitting are shown in Figure 10.50

and 10.51. Both  $T_1$  fitting approaches give qualitatively similar simulations: the differences can be seen only at timescales where  $T_1$  is crucial, e.g., compare curve in Figure 10.48(a) and 10.51(a). Also in this case, the simulated absolute intensities of the signal right after THz pulse (Figure 10.52) reasonable reproduce the experimental data, considering the shift of 6 dB. In contrast to the results in the previous section (Figure 10.49), the effect of the additional relaxation during THz pulse is no more significant.

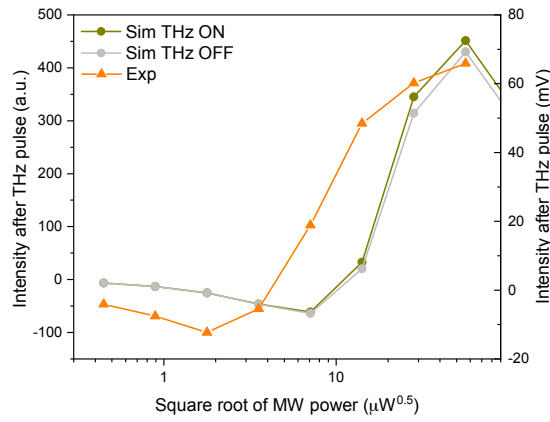


**Figure 10.52:** Dependence at 20 K of the signal intensity at 21.4 ms on the square root of MW power, obtained by the single exponential fitting of  $T_1$ . Green circles show data with additional relaxation during THz pulse channel,  $T_{THz} = 250$  ms; gray circles show the same without additional relaxation,  $T_{THz} = \infty$ ; orange triangles show the experimental data.



## 10.8.3 Simulation of MW power dependence at 55 K

$T_1$  equals to the longest decay time from three exponential fitting

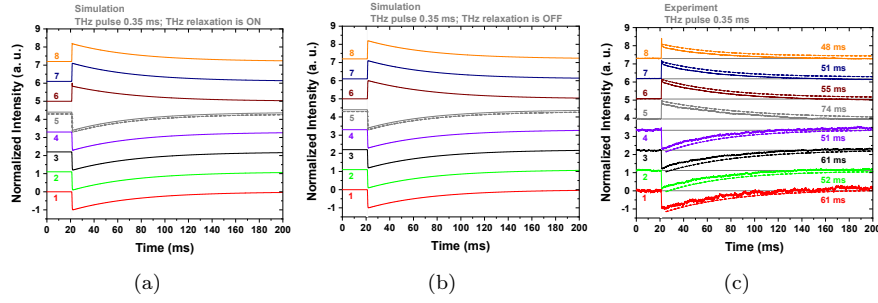


**Figure 10.53:** (a) Simulations of the signal with following parameters:  $T=55$  K,  $T_{THz}=260$  ms,  $T_{term}=55$  ms,  $\tau_2=350$   $\mu$ s; (b) simulation without the additional THz-induced relaxation channel ( $T_{THz} = \infty$ ) and (c) experimental data at different MW power (1) 60 dB; (2) 54 dB; (3) 48 dB; (4) 42 dB; (5) 36 dB, dashed gray line 36.5 dB; (6) 30 dB; (7) 24 dB; (8) 18 dB. The kinetics are horizontally shifted for a better comparison.

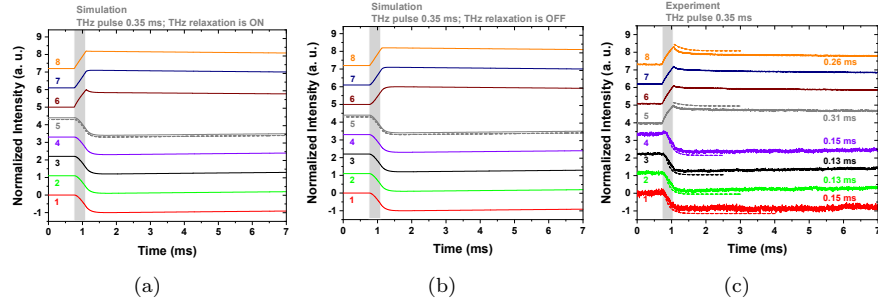


**Figure 10.54:** (a) Zoom at shorter times of the simulations of the signal with following parameters:  $T=55$  K,  $T_{THz}=260$  ms,  $T_{term}=55$  ms,  $\tau_2=350$   $\mu$ s; (b) simulation without the additional THz-induced relaxation channel ( $T_{THz} = \infty$ ) and (c) experimental data at different MW power (1) 60 dB; (2) 54 dB; (3) 48 dB; (4) 42 dB; (5) 36 dB, dashed gray line 36.5 dB; (6) 30 dB; (7) 24 dB; (8) 18 dB. The kinetics are horizontally shifted for a better comparison.

At 55 K the general behavior of the simulated kinetics also reproduces the experimental data (Figure 10.53 and 10.54). For both the temperatures, the same set of parameters are used except the temperature value. It is interesting to note that simulations correctly predict an additional negative kinetics at 55 K in comparison with 20 K (compare curve 5 in Figure 10.47(a), 10.47(c) and Figure 10.53(a), 10.53(c)). In the simulation, the effect of additional relaxation during THz pulse is practically indistinguishable from  $T_1$ -limited relaxation

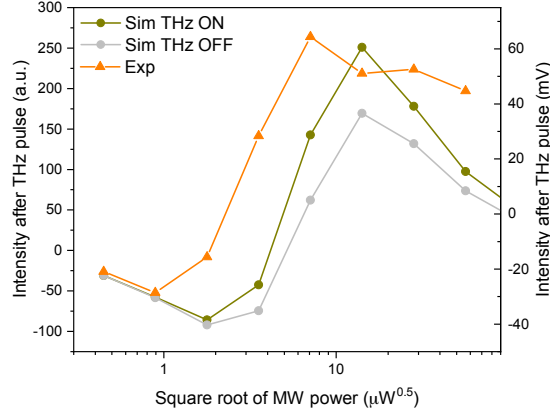


**Figure 10.55:** Dependence at 55 K of the signal intensity at 21.4 ms on the square root of MW power, obtained by the three exponential fitting of  $T_1$ . Green circles show data with additional relaxation during THz pulse channel,  $T_{THz} = 260$  ms; gray circles show the same without additional relaxation,  $T_{THz} = \infty$ ; orange triangles show the experimental data.

caused by the THz-induced sample heating. This is due to the shorter  $T_1$  at 55 K whereby THz relaxation cannot contribute significantly at this temperature. In addition,  $T_1$  is almost temperature independent above 50 K (Figure 10.13(a)) reducing the efficiency of the THz-induced relaxation channel. On the contrary, the experimental data (curves 5-8 in Figure 10.53(c) and 10.54(c)) still show the feature ascribed to the THz-induced relaxation channel. In the model  $T_{THz}$  is considered to be temperature independent, but such approximation neglects the changing in the occupation number of the phonons' states.

The simulated absolute intensities of the signal right after THz pulse (Figure 10.55) reasonable reproduce the experimental data, once shifted for 6 dB. The effect of the additional relaxation during THz pulse is almost imperceptible since, at 55 K, the  $T_1$  of the spin system is shorter than at 20 K and an additional, weak, THz relaxation channel almost does not influence the kinetics.

$T_1$  equals to the decay time from single exponential fitting

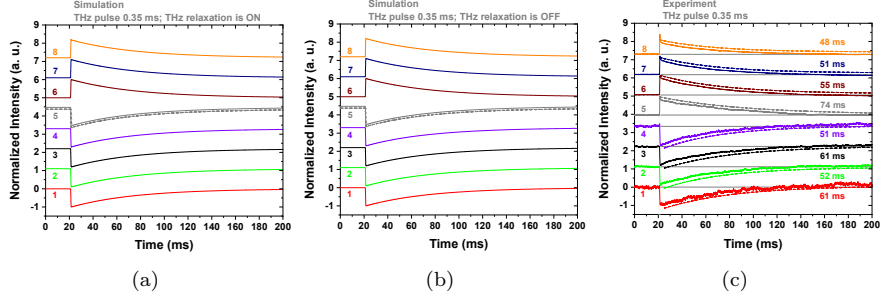


**Figure 10.56:** (a) Simulations of the signal with following parameters:  $T=55$  K,  $T_{THz}=250$  ms,  $T_{term}=55$  ms,  $\tau_2=350$   $\mu$ s; (b) simulation without the additional THz-induced relaxation channel ( $T_{THz} = \infty$ ) and (c) experimental data at different MW power (1) 60 dB; (2) 54 dB; (3) 48 dB; (4) 42 dB; (5) 36 dB, dashed gray line 36.5 dB; (6) 30 dB; (7) 24 dB; (8) 18 dB. The kinetics are horizontally shifted for a better comparison.

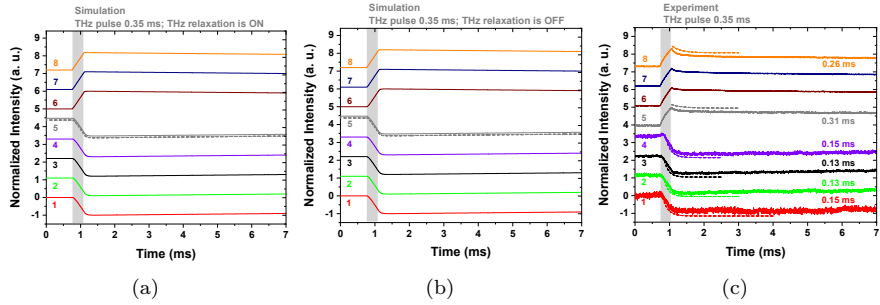


**Figure 10.57:** (a) Zoom at shorter times of the simulations of the signal with following parameters:  $T=55$  K,  $T_{THz}=250$  ms,  $T_{term}=55$  ms,  $\tau_2=350$   $\mu$ s; (b) simulation without the additional THz-induced relaxation channel ( $T_{THz} = \infty$ ) and (c) experimental data at different MW power (1) 60 dB; (2) 54 dB; (3) 48 dB; (4) 42 dB; (5) 36 dB, dashed gray line 36.5 dB; (7) 24 dB; (8) 18 dB. The kinetics are horizontally shifted for a better comparison.

The comparison between the simulation and the experimental results at 55 K is shown in Figure 10.56 and 10.57. Considerations similar to what has been mentioned in the previous section (sec. 10.8.3) hold also for the case of  $T_1$  coincident with the decay time of the single exponential fitting.

The simulated absolute intensities of the signal right after THz pulse (Figure 10.58) reasonable reproduce the experimental data also at 55 K, once shifted for 6 dB as in the previous cases. The effect of the additional relaxation during THz pulse is almost imperceptible as for the results obtained by three exponential

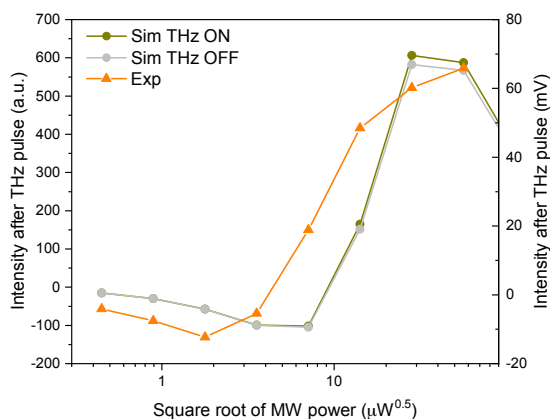


**Figure 10.58:** Dependence at 55 K of the signal intensity at 21.4 ms on the square root of MW power, obtained by the single exponential fitting of  $T_1$ . Green circles show data with additional relaxation during THz pulse channel,  $T_{THz} = 250$  ms; gray circles show the same without additional relaxation,  $T_{THz} = \infty$ ; orange triangles show the experimental data.

fitting of  $T_1$ .

#### 10.8.4 Simulation of THz power dependence

The simulation of the effect of THz radiation power on time-resolved signal has also been implemented by using the model described before. In this case, the empirical parameter  $A$ , that affects the sample heating, has been reduced, while  $T_{THz}$  has been extended, considering that heating and additional relaxation have a similar dependence on the power of THz. Experimental data was recorded at 20 K, 30 dB (200  $\mu$ W MW power), therefore the simulations have been performed using the same parameters. Kinetics at  $A$  equal to 12.105 (average THz power of 100 W), 6.053 (50 W), and 3.02 (25 W) were simulated.  $T_{THz}$  was correspondingly reduced to 250 ms (100 W); 500 ms (50 W), and 1000 ms (25 W). Only the longest  $T_1$  model was used, since no significant differences between these two models were observed in the simulations of MW power dependence.

The model succeeds in predict the decrease, proportional to averaged THz power, in the amplitude of the signal (Figure 10.59(a)). This is valid when both  $A$  and  $1/T_{THz}$  are reduced correspondingly. As it follows from the comparison in Figure 10.60, in the current state the model fails in predicting the change in the decay time of thermal relaxation. According to experimental data (Figure 10.60(b)), the less averaged power irradiates the sample, the faster is the thermal relaxation after THz pulse. At the moment, the model considers the

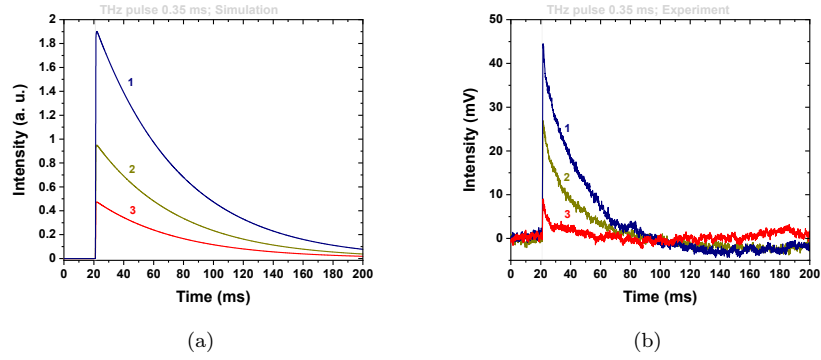


**Figure 10.59:** Simulations (a) and experimental data (b) at different averaged THz power: (1)  $A=12.105$ ; average THz power 100 W;  $T_{THz}=250$  ms; (2)  $A=6.053$ ; average THz power 50 W;  $T_{THz}=500$  ms; (3)  $A=3.03$ ; average THz power 25 W;  $T_{THz}=1000$  ms. The other parameters are kept fixed:  $T=20$  K,  $T_{term}=55$  ms,  $\tau_2=350$   $\mu$ s.

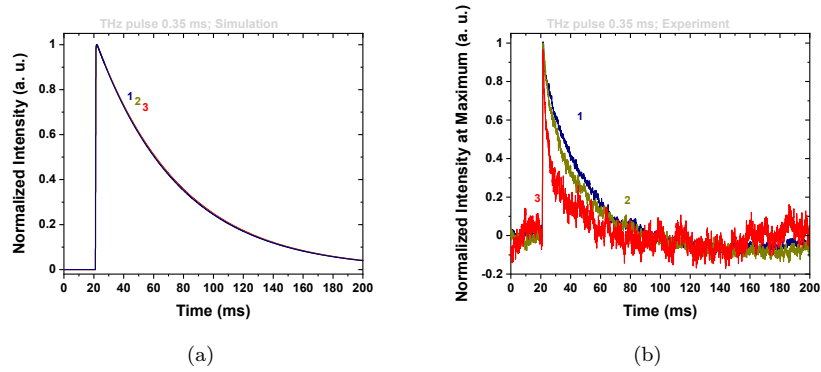


**Figure 10.60:** Simulations (a) and experimental normalized data (b) at different averaged THz power: (1)  $A=12.105$ ; average THz power 100 W;  $T_{THz}=250$  ms; (2)  $A=6.053$ ; average THz power 50 W;  $T_{THz}=500$  ms; (3)  $A=3.03$ ; average THz power 25 W;  $T_{THz}=1000$  ms. The other parameters are kept fixed:  $T=20$  K,  $T_{term}=55$  ms,  $\tau_2=350$   $\mu$ s.

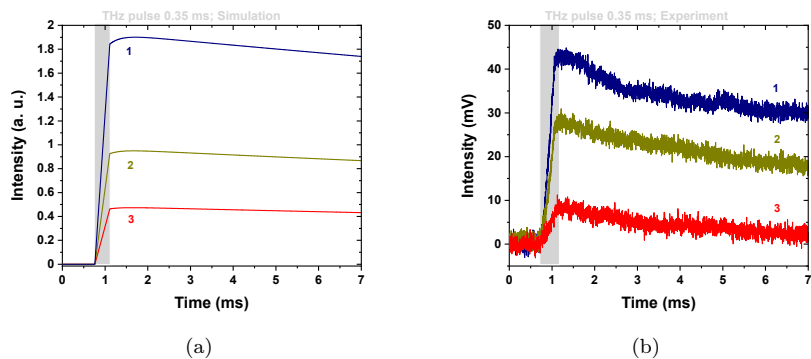


Figure 10.61: Zoom at short times of Figure 10.59.

thermal relaxation after THz pulse as one exponential decay process with  $T_{term}$  as characteristic time. The more sophisticated description is needed to reproduce experimental data in simulation. The impact of additional relaxation during THz pulse reveals itself as linear behavior of the kinetics during the THz pulse.

## 10.9 Conclusions

The study discussed in this chapter revealed some insights into the spin relaxation mechanisms when the spin system is irradiated by high power THz pulses. In particular, the **VOTPP** shows a very peculiar behavior when the MW power is varied. Indeed, when it approaches the saturation, the TR-THz-EPR signal changes from negative to positive revealing that the acceleration of the spin relaxation process overcomes the negative effect of the temperature increase. Such an effect is caused by two phenomena:

- the temperature dependence of  $T_1$ : during the THz irradiation, the sample is heated and its temperature rapidly jumps of several Kelvins. Since the **VOTPP**  $T_1$  has a strong temperature dependence, it dramatically reduces  $T_1$ , causing the increase of the spin relaxation rate;
- the THz-induced spin relaxation: this phonon-mediated process induces a further relaxation of the spin population when the phonon is perturbed by the THz radiation. The magnitude of this effect is smaller compared to that of the change in  $T_1$ , but it is clearly visible at 20 K.

While the former is a well-known effect, the latter is, for the best of our knowledge, unprecedented. The indispensable requirement of the resonance condition

of the THz radiation with the phonon, as well as the linear behavior of the TR-THz-EPR signal intensity by varying the THz power, corroborate the hypothesis of a process mediated by the spin-phonon coupling. Also the simulations, although performed with a simple model, definitely highlight the presence of this additional phenomenon. Till now, it is treated phenomenologically by introducing an additional relaxation term in the  $z$ -component of the magnetization of the Bloch equation, but further studies, based on *ab-initio* calculations, are under development. Moreover, to confirm the phonon-mediated nature of such effect, other TR-THz-EPR experiments irradiating a different phonon with a different spin-phonon coupling as well as performed on other suitable compounds, are in progress to further elucidate the origin of the phenomenon.

## References

- [1] L. Tesi et al. “Giant spin-phonon bottleneck effects in evaporable vanadyl-based molecules with long spin coherence”. In: *Dalton Transactions* 45.42 (2016), pp. 16635–16643. ISSN: 14779234. DOI: 10.1039/c6dt02559e.
- [2] Dante Gatteschi, Roberta Sessoli, and Jacques Villain. *Molecular nanomagnets*. Vol. 5. Oxford University Press on Demand, 2006.
- [3] JH Van Vleck. “Paramagnetic relaxation times for titanium and chrome alum”. In: *Physical Review* 57.5 (1940), p. 426.
- [4] AC De Vroomen et al. “Electron spin-lattice relaxation of the Zeeman and interaction systems in CuCs<sub>2</sub> (SO<sub>4</sub>)<sub>2</sub> · 6H<sub>2</sub>O”. In: *Physica* 61.2 (1972), pp. 241–249.
- [5] Matteo Atzori et al. “Spin dynamics and low energy vibrations: insights from vanadyl-based potential molecular qubits”. In: *Journal of the American Chemical Society* 139.12 (2017), pp. 4338–4341.
- [6] Alessandro Lunghi et al. “Intra-molecular origin of the spin-phonon coupling in slow-relaxing molecular magnets”. In: *Chemical Science* 8.9 (2017), pp. 6051–6059. ISSN: 20416539. DOI: 10.1039/c7sc02832f.
- [7] Zixiang Chi et al. “Comparative Study of three Mononuclear Vanadium-Aromatic 1, 2-Diol Complexes: Structure, Characterization and Anti-Proliferating Effects Against Cancer Cells”. In: *Zeitschrift für anorganische und allgemeine Chemie* 638.10 (2012), pp. 1523–1530.
- [8] Matteo Atzori et al. “Quantum coherence times enhancement in vanadium (IV)-based potential molecular qubits: the key role of the vanadyl moiety”. In: *Journal of the American Chemical Society* 138.35 (2016), pp. 11234–11244.

CHAPTER 10. Spin dynamics under THz irradiation

- [9] Alessandro Lunghi et al. “The role of anharmonic phonons in under-barrier spin relaxation of single molecule magnets”. In: *Nature Communications* 8 (Mar. 2017). ISSN: 20411723. DOI: 10.1038/ncomms14620.
- [10] L. Escalera-Moreno et al. “Determining Key Local Vibrations in the Relaxation of Molecular Spin Qubits and Single-Molecule Magnets”. In: *Journal of Physical Chemistry Letters* 8.7 (Apr. 2017), pp. 1695–1700. ISSN: 19487185. DOI: 10.1021/acs.jpclett.7b00479.
- [11] Salvatore Califano, Vincenzo Schettino, and Natale Neto. “Lattice Dynamics”. In: *Lattice Dynamics of Molecular Crystals*. Springer, 1981, pp. 1–40.
- [12] Natale Neto and Luca Bellucci. “A new algorithm for rigid body molecular dynamics”. In: *Chemical Physics* 328.1-3 (2006), pp. 259–268.
- [13] Alfred G Redfield. “On the theory of relaxation processes”. In: *IBM Journal of Research and Development* 1.1 (1957), pp. 19–31.
- [14] Edward I. Solomon and A. B. P. Lever. *Inorganic Electronic Structure and Spectroscopy, Volume 1: Methodology*. John Wiley & Sons, Inc., 1999.
- [15] Matteo Atzori et al. “Structural effects on the spin dynamics of potential molecular qubits”. In: *Inorganic chemistry* 57.2 (2018), pp. 731–740.
- [16] Kenneth S Cole and Robert H Cole. “Dispersion and absorption in dielectrics I. Alternating current characteristics”. In: *The Journal of chemical physics* 9.4 (1941), pp. 341–351.
- [17] Chandran Karunakaran and Murugesan Balamurugan. “Chapter Five - Advances in Electron Paramagnetic Resonance”. In: *Spin Resonance Spectroscopy*. Ed. by Chandran Karunakaran. Elsevier, 2018, pp. 229–280. ISBN: 978-0-12-813608-9. DOI: <https://doi.org/10.1016/B978-0-12-813608-9.00005-8>. URL: <http://www.sciencedirect.com/science/article/pii/B9780128136089000058>.
- [18] Daocong Li et al. “Theoretical studies on molecular structure and vibrational spectra of copper phthalocyanine”. In: *Vibrational Spectroscopy* 39.2 (2005), pp. 191–199.
- [19] Katrin F Domke and Bruno Pettinger. “In Situ Discrimination between Axially Complexed and Ligand-Free Co Porphyrin on Au (111) with Tip-Enhanced Raman Spectroscopy”. In: *ChemPhysChem* 10.11 (2009), pp. 1794–1798.
- [20] Lawrence J Berliner, Sandra S Eaton, and Gareth R Eaton. *Distance measurements in biological systems by EPR*. Vol. 19. Springer Science & Business Media, 2006.



## REFERENCES

- [21] Sergey L Veber et al. “X-band EPR setup with THz light excitation of Novosibirsk Free Electron Laser: Goals, means, useful extras”. In: *Journal of Magnetic Resonance* 288 (2018), pp. 11–22.
- [22] Tsutomu Yamabayashi et al. “Scaling Up Electronic Spin Qubits into a Three-Dimensional Metal–Organic Framework”. In: *Journal of the American Chemical Society* 140.38 (2018), pp. 12090–12101.
- [23] AV Tyurin et al. “Thermodynamic functions of vanadyl acetylacetonate VO (C 5 H 7 O 2) 2 at 0–350 K”. In: *Russian Journal of Physical Chemistry A* 89.10 (2015), pp. 1711–1714.

*CHAPTER 10. Spin dynamics under THz irradiation*

Part V

Conclusions



The scientific work described in this dissertation has been devoted to the individuation of the theoretical “bricks” required to build solid-state molecular Qubits able to retain long coherence time up to room temperature. Since the  $T_m$  is upper limited by the spin-lattice relaxation time,  $T_1$ , the efforts during these three years have been focused on the improvement of the latter, which is deeply connected to the vibrations of the paramagnetic ion’s surrounding environment. Such investigation has been performed on several different homoleptic magnetic molecules based on vanadium(IV), which has electronic spin value  $S= 1/2$  and nuclear spin  $I= 7/2$ , in different coordination environments.

The disclosure of the spin relaxation processes has been possible through a multi-techniques approach, which was able to take into account different and complementary perspectives of the same issue. Indeed, on one side the standard magnetic techniques, such as CW and pulse EPR together with AC susceptometry, allow the complete characterization of the magnetic properties; and, on the other side, THz spectroscopy makes it possible the investigation of the phonons, namely both lattice and low-energy molecular vibrations. This innovative approach allows the full description of the system, providing several insights into the correlation between the spin dynamics and the vibrations that take place nearby the atom bearing the unpaired electron. More specifically, such vibrations have been recognised as the main parameter in determining the temperature dependence of  $T_1$  when affected by the direct and Raman relaxation processes. Accordingly, the lack of low energy vibrational modes provides very weak temperature dependence of the spin-lattice relaxation times. This may represent a key aspect in realizing molecular-based quantum systems with manipulable quantum properties even at room temperature. Moreover, the temperature dependence of some parameters, extracted by fitting the magnetic field dependence of the spin-lattice relaxation time with the Brons-van Vleck model, follows an Arrhenius-like behavior which allows to obtain an effective activation energies of the relaxation processes. Interestingly, the latter well correlate with some of the low-energy vibrational modes, experimentally detected by THz-TDS. In this context, a new THz-TDS set up based on plasma generation of THz radiation and Air-biased Coherent Detection has been implemented to reach a wider spectral window, namely from 0.5 to 15 THz (ca. from 15 to 500  $\text{cm}^{-1}$ ), allowing further and more informative measurements. The performance of this new set up has been tested on liquid water, revealing high-quality spectra even on this material, which is historically difficult to measure by transmission IR spectroscopies.

In this framework, the importance of theoretical calculations is evident. The spin-phonon coupling can be obtained only by *ab initio* calculations and it provides the unequivocal key to correctly interpret the experimental results. Furthermore, the complex phonons structure is shared by almost all the investigated

compounds therefore the deep investigation of the vibrational modes requires the support of theoretical simulations.

Additional insights into the influence of the phonons on the spin system have been reached by the use of a more exotic technique, namely the Time-resolved THz-pump EPR-probe experiment. This exploits a Free Electron Laser source capable to produce high-power monochromatic THz radiation, which can be tuned in a wide range of frequency, to study the influence of the strong THz excitation of some selected phonons on the spin relaxation. It revealed an unprecedented behavior of the [VO(TPP)] spin dynamics resulting in a phonon-mediated THz-induced spin relaxation when the system approaches the saturation. Such effect, although small compared to others, is paramount in the comprehension of the spin-phonon coupling providing a further step toward the understanding of the spin-lattice relaxation. Also, it can be a starting point for the spin manipulation in performing logic operations in potential solid-state molecular Qubits.

Molecular Qubits are still less performing compared to other Qubit platforms, but they have undeniable interesting features that make them appealing for the purpose. In fact, molecules can be tailored at will thanks to the extremely tunability of their electronic and magnetic properties through a rational synthetic design. Moreover, they seem to be very promising candidates for realizing multi-Qubits architectures and many efforts are going toward this direction. A first step in the use of vanadyl molecules to realize two-Qubits gates has been already achieved, demonstrating also the possibility to implement hybrid electron-nuclear spin schemes by exploiting the hyperfine interaction of the vanadium atom.

Finally, another important aspect to keep in mind is that several of the investigated vanadyl-based molecules can be addressed on surface. This represents a great advantage in the design of real Qubit devices, especially in the engineering process.

# Appendices





## Appendix A

# Error analysis

In this appendix the treatment of the error will be discussed recalling few basic statistic concepts. The error analysis has been carried out on data examined in section 9.1 but the results also apply for the other spectroscopic data of chapter 9.

Each spectrum shown in section 9.1 is the result of the average of about 120 acquisitions that require approximately 12 hours. As previously discussed, each acquisition consist of two measurements: the sample signal which is acquired together with the reference signal, in order to minimize the effect of the external perturbations such as the temperature variation of the set up, fluctuations of the laser power, etc. The extraction of the margin of error that affects the spectral features (frequency  $\omega$  and widths  $\Gamma_L$  and  $\Gamma_G$  of the peaks) has been performed obtaining these parameters by fitting the spectrum corresponding to each acquisition with equation (9.4) and then evaluating the standard deviation (equation (A.2)) and the relative standard deviation (equation (A.3)).

$$\bar{x} = \frac{1}{N} \sum_{i=1}^N x_i \quad (\text{A.1})$$

$$\sigma_x = \sqrt{\frac{1}{N-1} \sum_{i=1}^N (x_i - \bar{x})^2} \quad (\text{A.2})$$

$$\sigma\%_x = \frac{\sigma_x}{\bar{x}} \cdot 100 \quad (\text{A.3})$$

In particular, the fit error has been evaluated for the 10 and 300 K, that are the extremes of the investigated temperature range. As discussed in section 9.1, the former temperature value corresponds to the spectrum having the better separation of the peaks whether the latter coincides with the spectrum with the greater overlap among the peaks. In principle it is thus possible to extrapolate

CHAPTER A. Error analysis

the smallest and the greatest errors that affect the fit. Indeed, it is clear that at 10 K the peaks are narrower and better separated with respect to 300 K, making the quality of the curve fitting higher. Moreover, the central frequency of the pseudo-Voigts is extracted more efficiently compared to the Gaussian and Lorentzian width because the latter are particularly sensitive to both the choice of the base line and the presence of asymmetries in the peak shape as well as of noise on the peak tails.

In table A.1, the relative standard deviation on the frequency values of the five peaks is shown for the two edge temperatures. The error arising from the fit at 10 K is about the half of the observed error that affect the temperature trend of the peaks' frequency (Figure 9.7). The underestimation can be ascribed to other and heavier error sources which can be either systematic or random with a long time evolution. Indeed, if the acquisition time is shorter than that needed to average out the randomly oscillation of an external parameter, such as the temperature variation of the setup during the day, it produces an additional error source. At 300 K the fit error is comparable to the observed one since the goodness of fit is worse. The error bars reported in Figure 9.7 and Figure A.1 qualitatively takes into account the error that affects the temperature trend of the frequency values and are comparable to the standard deviation of the fit at 300 K.

Peak label	Fit error (%)		Observed error (%)
	10 K	300 K	
<b>1</b>	0.10	0.25	0.35
<b>2</b>	0.10	-	0.15
<b>3</b>	0.05	0.10	0.10
<b>4</b>	0.15	0.30	0.35
<b>5</b>	0.20	0.25	0.25

**Table A.1:** Relative standard deviations at 10 and 300 K of the fit and observed  $\sigma\%$  that affect the temperature trend of the frequencies.

As already mentioned, the extrapolation of Gaussian  $\Gamma_G$  and Lorentzian  $\Gamma_L$  widths suffers from higher margin of error because these parameters are highly dependent from the choice of the base line and also the goodness of the fit strongly depends on possible asymmetries in the peak shape as well as the presence of noise on the peak tails. It is therefore evident that in this case the primary source of error is ascribed to the fit whose relative standard deviation is of the order of 10-20% or more (see Table A.2).

The temperature behaviour of the Gaussian and Lorentzian width is shown in Figure A.2. As mentioned in section 9.1, **2** almost disappears above 120 K and **5**, being at the right edge of the spectrum, suffers from higher noise compared to

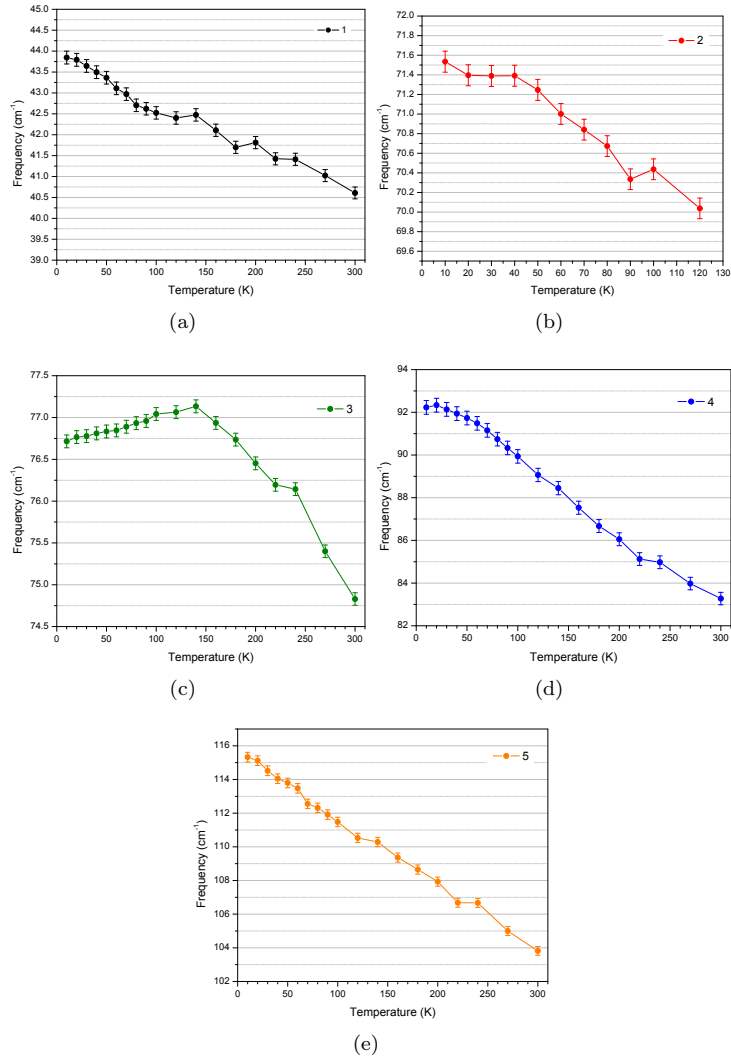


**Figure A.1:** Temperature trend of the frequency for peak 1 (a), 2 (b), 3 (c), 4 (d), 5 (e). The error bars are qualitatively evaluated.

Peak label	$\sigma\%$ Gaussian width		$\sigma\%$ Lorentzian width	
	10 K	300 K	10 K	300 K
1	18	27	10	18
2	45	-	45	-
3	20	32	12	26
4	46	58	9	29
5	25	42	41	55

**Table A.2:** Relative standard deviations at 10 and 300 K of the fit that affect the temperature trend of the Gaussian and Lorentzian line widths.

CHAPTER A. Error analysis

the other peaks, leading to higher  $\sigma\%$ .

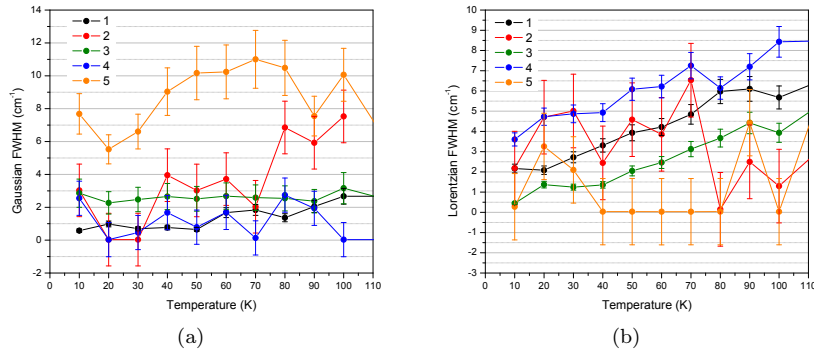


**Figure A.2:** Temperature trend of the (a) Gaussian line width and (b) Lorentzian line width in the 10-100 K temperature range. The error bars correspond to the relative standard deviation at 10 K.

The fit error on  $\Gamma_G$  and  $\Gamma_L$  of **1**, **3** and **4** clearly allows to extrapolate a linear trend for the homogeneous widths while the inhomogeneous widths remain almost constant. On the contrary, **2** and **5** are affected by a higher error which makes impossible to identify a tendency.

## Appendix B

# Origin of Bloch equations

Let us consider a charged particle rotating anticlockwise: it has an associated magnetic moment  $\boldsymbol{\mu}$  due to the charge motion. Since the particle is an electron, it has the spin angular momentum  $\mathbf{S}$  and consequently  $\boldsymbol{\mu}_S = \gamma\mathbf{S}$ , where  $\gamma$  is the gyromagnetic ratio. In a magnetic field  $\mathbf{B}$ , the magnetic moment behaves as a magnetic dipole experiencing a torque  $\boldsymbol{\tau}$ :

$$\boldsymbol{\tau} = \boldsymbol{\mu} \times \mathbf{B} \quad (\text{B.1})$$

The magnetic moment will precess with an angular frequency  $\omega_L$  called Larmor frequency that is directly related to the applied magnetic field through the relation  $\omega_L = \gamma B$ .

Considering a macroscopic sample composed by an ensemble of spins. The magnetization will be  $\mathbf{M} = \sum_i \boldsymbol{\mu}_i$  and in terms of total angular momentum  $\mathbf{M} = \gamma\mathbf{L}$ .

The interaction of the magnetization with the magnetic field gives a torque on the system changing its angular momentum[1]

$$\boldsymbol{\tau} = \frac{d\mathbf{L}}{dt} = \mathbf{M} \times \mathbf{B} \quad (\text{B.2})$$

and in terms of magnetization

$$\frac{d\mathbf{M}}{dt} = \gamma \frac{d\mathbf{L}}{dt} = \gamma \mathbf{M} \times \mathbf{B} \quad (\text{B.3})$$

which is the Bloch equation. Making explicit the vector product

$$\mathbf{M} \times \mathbf{B} = \begin{vmatrix} \underline{i} & \underline{j} & \underline{k} \\ M_x & M_y & M_z \\ B_x & B_y & B_z \end{vmatrix} = (M_y B_z - M_z B_y)\underline{i} + (M_z B_x - M_x B_z)\underline{j} + (M_x B_y - M_y B_x)\underline{k}$$

## CHAPTER B. Origin of Bloch equations

the individual components of Bloch equation can be obtained as follow.

$$\begin{aligned}\frac{dM_x}{dt} &= \gamma(M_y B_z - M_z B_y) \\ \frac{dM_y}{dt} &= \gamma(M_z B_x - M_x B_z) \\ \frac{dM_z}{dt} &= \gamma(M_x B_y - M_y B_x)\end{aligned}\tag{B.4}$$

Let us now consider that the applied static magnetic field lies along the  $z$  direction,  $\mathbf{B} = B_z$ . The components of  $\mathbf{B}$  in the  $xy$  plane are equal to zero and the magnetization will precess around the  $z$  axis. Making such approximation, the Bloch equations reads:

$$\begin{aligned}\frac{dM_x}{dt} &= \gamma M_y B_z \\ \frac{dM_y}{dt} &= -\gamma M_x B_z \\ \frac{dM_z}{dt} &= 0\end{aligned}\tag{B.5}$$

### B.1 Bloch equations with relaxation process

If we also include relaxation processes, the general equations become[1]

$$\begin{aligned}\frac{dM_x}{dt} &= \gamma(M_y B_z - M_z B_y) - \frac{M_x}{T_2} \\ \frac{dM_y}{dt} &= \gamma(M_z B_x - M_x B_z) - \frac{M_y}{T_2} \\ \frac{dM_z}{dt} &= \gamma(M_x B_y - M_y B_x) - \frac{M_z - M_0}{T_1}\end{aligned}\tag{B.6}$$

whereas considering the above mentioned approximation, they reads

$$\begin{aligned}\frac{dM_x}{dt} &= \gamma M_y B_z - \frac{M_x}{T_2} \\ \frac{dM_y}{dt} &= -\gamma M_x B_z - \frac{M_y}{T_2} \\ \frac{dM_z}{dt} &= -\frac{M_z - M_0}{T_1}\end{aligned}\tag{B.7}$$

## B.2 Including perturbation in the system: RF field

Let us assume that an external perturbation through a radio-frequency field is applied in the  $xy$  plane. The RF field can be written as[2]

$$\begin{aligned} B_{1x} &= B_1 \cos(\omega t) \\ B_{1y} &= B_1 \sin(\omega t) \\ B_{1z} &= 0 \end{aligned} \tag{B.8}$$

The Bloch equations reads

$$\begin{aligned} \frac{dM_x}{dt} &= \gamma(M_y B_z - M_z B_1 \sin(\omega t)) - \frac{M_x}{T_2} \\ \frac{dM_y}{dt} &= \gamma(M_z B_1 \cos(\omega t) - M_x B_z) - \frac{M_y}{T_2} \\ \frac{dM_z}{dt} &= \gamma(M_x B_1 \sin(\omega t) - M_y B_1 \cos(\omega t)) - \frac{M_z - M_0}{T_1} \end{aligned} \tag{B.9}$$

## B.3 Rotating frame

In the laboratory frame the magnetization precess around the  $z$  axis at the Larmor frequency. To probe the changes induced by the RF field it is convenient to work in a new reference system, called rotating frame, whose  $z$  axis correspond to the  $z$  axis of the laboratory frame and the  $x$  and  $y$  axis rotate at the Larmor frequency. In this new reference system the magnetization appears stationary at the equilibrium.

The transformation of Bloch equations in the rotating frame requires that two new variables must be defined as follow

$$\begin{aligned} M'_x &= M_x \cos(\omega t) - M_y \sin(\omega t) \\ M'_y &= M_x \sin(\omega t) + M_y \cos(\omega t) \end{aligned} \tag{B.10}$$

and therefore

$$\begin{aligned} M_x &= M'_x \cos(\omega t) + M'_y \sin(\omega t) \\ M_y &= M'_x \sin(\omega t) - M'_y \cos(\omega t) \end{aligned} \tag{B.11}$$

The time derivative of the magnetization components in the rotating frame

CHAPTER B. Origin of Bloch equations

reads[2]

$$\begin{aligned}\frac{dM'_x}{dt} &= \frac{dM_x}{dt} \cos(\omega t) - \frac{dM_y}{dt} \sin(\omega t) - \omega[M_x \sin(\omega t) + M_y \cos(\omega t)] \\ &= \gamma B_z M'_y - \omega M'_y - \frac{M'_x}{T_2} \\ &= (\omega_0 - \omega) M'_y - \frac{M'_x}{T_2}\end{aligned}\tag{B.12}$$

$$\frac{dM'_y}{dt} = -(\omega_0 - \omega) M'_x + \omega_1 M'_z - \frac{M'_y}{T_2}\tag{B.13}$$

$$\frac{dM'_z}{dt} = -\omega_1 M'_y - \frac{M'_z - M_0}{T_1}\tag{B.14}$$

where  $\omega_0 = \gamma B_z$ ,  $\omega_1 = \gamma B_1$  are the Larmor frequencies respectively proportional to the strength of the static field and to the amplitude (power) of the MW radiation;  $\omega$  is the resonance frequency of the spins. Generally in a complex system there are several groups of spins according to their own energy gaps which depend on the specific surrounding environment. From now on we will always work in the rotating frame therefore we will drop the single quote marks in the following equations.

A further approximation that can be done in this case is considering each spin having the same resonance condition. In this case  $\Delta\omega = \omega_0 - \omega = 0$  and the Bloch equations simplify as follows

$$\frac{dM_x}{dt} = -\frac{M_x}{T_2}\tag{B.15}$$

$$\frac{dM_y}{dt} = \omega_1 M_z - \frac{M_y}{T_2}\tag{B.16}$$

$$\frac{dM_z}{dt} = -\omega_1 M_y - \frac{M_z - M_0}{T_1}\tag{B.17}$$

## References

- [1] Felix Bloch. "Nuclear induction". In: *Physical review* 70.7-8 (1946), p. 460.
- [2] Charles Kittel. *Introduction to Solid State Physics*. 8th ed. John Wiley & Sons, 2004.